Utrecht University

UNIS
The University Centre in Svalbard

MASTER'S THESIS

Gravity and Magnetic Data Integration for Forward Modeling in Svalbard

Fenna AMMERLAAN

Earth Structure and Dynamics
Department of Earth Sciences
Utrecht University

In cooperation with:
Department of Arctic Geology
The University Centre in Svalbard

November 2023

Supervisors:

Dr. Aleksandra Smyrak-Sikora
Department of Arctic Geology, The University Centre in Svalbard

Dr. Kim Senger
Department of Arctic Geology, The University Centre in Svalbard

Dr. Cedric Thieulot
Department of Earth Sciences, Faculty of Geosciences, Utrecht University

Abstract

The Svalbard archipelago is located in Arctic Norway and forms the northwestern corner of the Barents Shelf. It has a complex geological history with multiple phases of deformation. NNW-SSE orientated long-lived tectonic lineaments separate the Pre-Caledonian basement rock of Svalbard into three distinct provinces. Svalbard is recognized for its high-quality geological outcrops, but less knowledge is available on density structure and geometry of the subsurface. To put further constraints on the subsurface, we performed a multi-physical data integration and used these as constraints for forward modeling. The specific focus was on the geophysical signal of the emplacement of magmatic bodies associated with the High Arctic Large Igneous Provinces (HALIP) and one of the main fault zones, the Billefjorden Fault Zone (BFZ).

Input data from various data sets sensitive to different physical parameters in the subsurface were considered. Among them were regional magnetic and gravity data, 2D seismic profiles, borehole logs and recently acquired inland gravity data. This new high resolution gravity data was collected in April 2022 along seismic lines in central Spitsbergen. We completed a satisfactory quality check of the data, after which they were used as input data for forward modeling where available.

Potential field data, magnetic and gravity data, are sensitive to changes in magnetic susceptibility and density, respectively. We enhanced the preliminary understanding of the regional potential field data by applying filter techniques to the data grids, amplifying long wavelength trends, and allowing depth and edge detection. The subsurface magnetic susceptibility and density structure was then quantified by magnetic and gravity forward modeling on five roughly E-W orientated profiles on Spitsbergen located along seismic lines. We made seismic interpretations to establish the subsurface geometry of the models, after which suitable physical parameters were assigned based on the available data. An iterative procedure followed to obtain the best fit of the modeled subsurface to the observed potential field data.

The regional data showed that the BFZ coincided with a high in magnetic and gravity anomalies, coming from a relatively shallow source. A long wavelength, deep magnetic anomaly was positioned below central Isfjorden but had no gravitational high. HALIP-related outcropping igneous rocks and sills were previously interpreted in this region. However, the depth and signal of the magnetic anomaly indicated a deeper situated source was necessary.

Forward modeling showed that the gravity anomaly trends were mostly explained by the basement topography, with an elevated basement along the BFZ and the influence of a thick sedimentary basin. To match the magnetic data on the three profiles intersecting the Isfjorden anomaly, large basement susceptibility contrasts were needed. As the other two profiles beyond the extent of the Isfjorden anomaly did not require heterogeneities in basement susceptibility, we favor the presence of a local magmatic body in the deep subsurface. Further geological implications of the forward modeling results are discussed, including scenarios for the emplacement of this magmatic body. The regional potential field analysis and the forward models have enabled us to put more constraints on the geometry and physical properties of the subsurface of Svalbard.

Acknowledgements

As I finalize my thesis, it is also a moment of reflection and gratitude for the amazing journey I have been on this year. When I first set foot in Svalbard in the autumn of 2022, I had no idea of which door I had just opened. Therefore, I want to start by thanking my supervisors for providing me the opportunity to come back and write my MSc Thesis at UNIS with all the resulting opportunities.

Aleks, your enthusiasm for the geology of Svalbard was very contagious. Thank you for the lively discussions, geofantasies, stratospheric clouds and advice for the thesis and beyond. Kim, I will never forget the polar flexibility. Thank you for your guidance throughout the thesis and for putting me in touch with the right people. Both of you have been fundamental to the process and I appreciate that.

I am also grateful to all the people I met at NGU who welcomed me into their office for two weeks. A special thank you to Marie-Andrée for not only providing guidance during my stay, but also for finding time afterwards to help me when I was lost in the potential fields. Jan Inge Faleide, thank you for the fruitful discussion during the research phase which helped defining the scope and outline of the work.

I must also extend my gratitude to the SvalGrav team who acquired the gravity data on which some of this work was based. A special thanks to Tereza, not only for leading this campaign but also for introducing me to Svalbard in the first few weeks and inspiring me for what is possible.

To NORRAM and the amazing people associated with it, thank you for adopting me into your program and providing me the opportunity to travel to Canada and Alaska while working on my thesis. I am grateful to have been involved in the program and hope to see some of you again in the future.

Tremendous thanks to the Masters of Disasters for the many shared coffees, drinks, laughs, public disturbances and in general good company both during and after office hours. You guys made the long thesis days more durable but more importantly, my stay so much more memorable.

Back in Utrecht, I want to thank Cedric for his help with arranging some of the logistics and being there to answer my questions. I am also grateful for my colleagues of the corner office for the cozy lunch breaks and daily stretches which were a nice interruption of the writing.

I am forever grateful to my friends back home who had to deal with me being away to wander between polar bears and ride snowscooters. But also to my family, for their unconditional support throughout my studies and I am very glad I got the opportunity to share some of the Svalbard magic with you.

I am grateful to all the people I had the pleasure of getting to know along the way. The location but definitely also the people are what made this doing this thesis so special, and I will forever cherish the time.

Contents

List of Figures

List of Tables

Acronyms

BFZ Billefjorden Fault Zone.

CCS Carbon capture and storage.

CSB Central Spitsbergen Basin.

DC Direct Current.

DEM Digital Elevation Model.

GPR Ground-Penetrating Radar.

HALIP High Arctic Large Igneous Province.

HFC Hornsund Fault Complex.

KTH KTH Institute of Technology in Stockholm.

LFZ Lomfjorden Fault Zone.

MT magnetotelluric.

NGU Norwegian Geological Survey.

NNF No Name Fault.

NPI Norwegian Polar Institute.

TWT two-way traveltime.

UiB University of Bergen.

UiT University of Tromsø.

UNIS The University Centre in Svalbard.

WSFTB West Spitsbergen Fold and Thrust Belt.

1 Introduction

In regions with a complex subsurface geometry and relatively sparse data availability, data integration is essential. It allows one to enhance the geological understanding of an area by combining information obtained from various geological and geophysical data sources, helping to fill in existing knowledge hiatuses. One of these geophysical data sources is potential field data. Anomalies in gravity and magnetic data are caused by density and susceptibility contrasts in the subsurface, respectively. The identification and understanding of the sources of these anomalies function as a steppingstone for further enhancing the understanding of the geological evolution of a region.

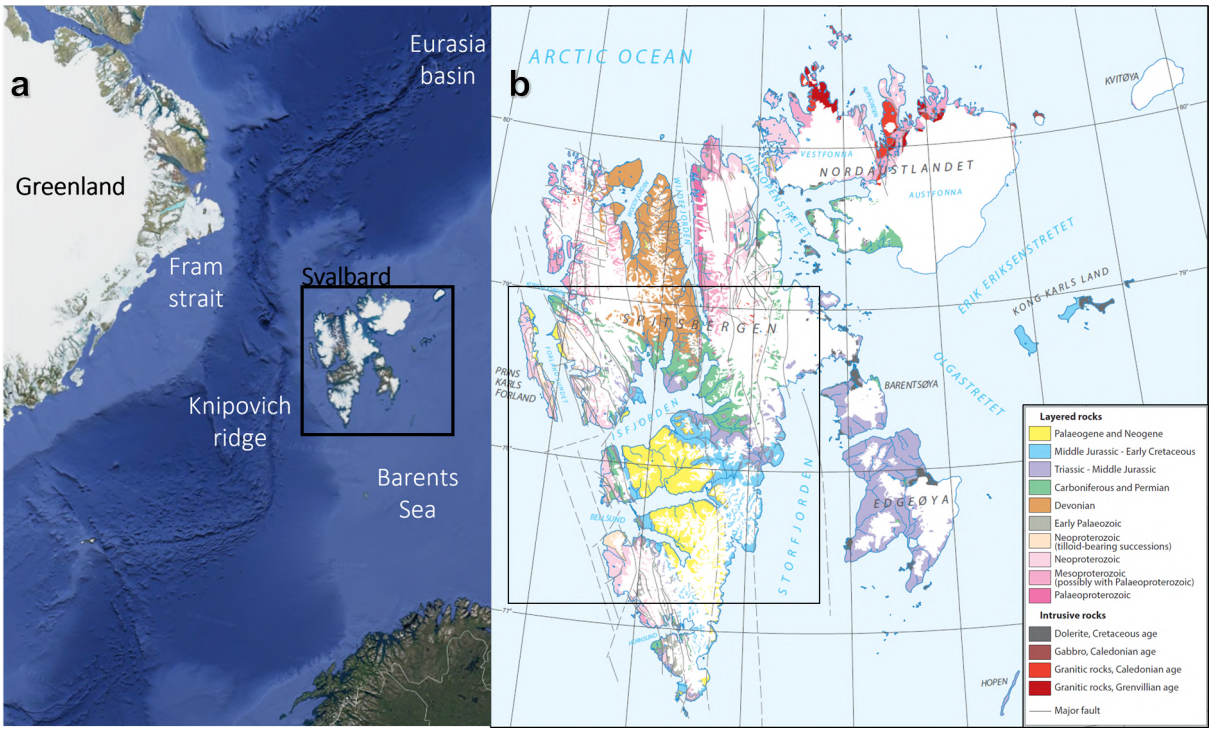

Figure 1.1: a) Location of Svalbard showing the main elements of the region. Black box showing the location of Figure b. b) Geological map of Svalbard from Dallmann (2015). Black box shows the location of Figure 1.2.

1.1 Svalbard

Svalbard is such a region with sparse data availability and a complex subsurface geometry. It is an archipelago in the high Arctic (74–81° N and 15–35°E) and forms the northwestern exposed part of the Barents Shelf, see Figure 1.1a. The exposed bedrock ranges from the Paleoproterozoic to Cenozoic sediments (Harland, 1997; Worsley, 2008) and 57% of the landscape is covered by glaciers (Nuth et al., 2013).

Recent uplift (Lasabuda et al., 2021) combined with a lack of vegetation make high-quality outcrops giving insight into the surfaced geology of Svalbard. Contrary, the structure of the subsurface is less well-known. Due to the challenging accessibility of the remote location, limited subsurface data are available of Svalbard. Data collected from the boreholes have a limited stratigraphic coverage and as most of the boreholes were in operation in the 20th century, logs can be incomplete with lower data quality (Senger et al., 2019). The seismic data have a limited spatial coverage, most of the 2D seismic data are collected offshore. While there are some onshore seismic profiles available, most of them are short, have a limited penetration depth and are confined to central Spitsbergen (Bælum et al., 2012).

1.2 Previous work

Geological understanding of Svalbard started far back in the 19th century when first geological maps of Svalbard were published (Nordenskiöld, 1867). The understanding of the area has increased significantly since then and a recent tectono-stratigraphic synthesis of the region can be found in Olaussen et al.

(2023). Previous studies have looked at various geophysical data sources in terms of magnetic, gravity and tomography data for constraining the subsurface structure of Svalbard or its surroundings.

The first big aeromagnetic surveys were acquired between 1987-1991 by the Norwegian Geological Survey (NGU) and various other operators (Skilbrei, 1991, 1992; Breivik & Faleide, 2004). A preliminary interpretation of this magnetic data was done by Skilbrei (1992). Their magnetic forward model showed that the basement topography alone was not sufficient to explain the observed anomalies. They argued for a geological object in the subsurface that could explain the intra-basement susceptibility contrasts.

A more recent magnetic survey, KRAS-16, was conducted by the Norwegian Geological Society (NGU) around the Fram strait between 2016-2018 (Dumais et al., 2020). This new potential field data gave insight into the evolution of the spreading at the Knipovich ridge (Dumais et al., 2021) as well as identifying thermal and crustal heterogeneities of the Fram Strait and Svalbard margin (Dumais et al., 2022). A more local onshore study was also performed on Austfonna, a big ice cap located on the island of Nordaustlandet located in the northeast of Svalbard. Potential field data were used to both evaluate the ice thickness of the glacier and therefore deduce the bedrock profile as to evaluate contrasts in basement susceptibilities (Dumais & Brönner, 2020).

Magnetic anomalies located offshore southeast of Svalbard were previously studied (Grogan et al., 2000; Minakov et al., 2012) and interpreted to be due to magmatic intrusions. Interpretations of both gravity and magnetic potential field anomalies of Svalbard were described in Dallmann (2015). It was argued the relatively large line spacing in combination with the sedimentary cover resulted in the magnetic signature to be overshadowed, therefore only large areas of high magnetic basement or volcanic intrusions could be identified. Some more trends could be identified based on the gravitational data, of which anomalies were linked to structural highs and lows, presence of igneous and metamorphic rocks and a large negative anomaly due to thickened crust on the western flank of Svalbard.

Previous tomographic studies were done in the surrounding of Svalbard which enhanced the understanding of the subsurface velocity and density structure. Velocity models were created based on seismic refraction data, after which they were converted to density models using general velocity-density relationships and gravity observations as constraints. The models of Ritzmann et al. (2002, 2004); Ljones et al. (2004) were of the western coast of Svalbard and studies southeast of Svalbard were done in Breivik et al. (2002, 2003, 2005). A 3D magnetic and gravity model of the entire Barents Sea was made using this data (Marello et al., 2013) as well a compilation of the ocean-continent transition east of Svalbard (Grad & Majorowicz, 2020). While these mostly offshore studies are relevant for a general comprehension of the deeper subsurface structure surrounding Svalbard, the scope of our research was more confined and focused on the subsurface of the archipelago itself.

With this goal in mind, a new potential field data land survey, SvalGrav, was acquired in the spring of 2022 along 7 profiles in central Spitsbergen, 260 gravity data points were collected with a station spacing of 500-2000 meters. Most of these profiles coincided with the location of previously acquired seismic lines. The gravity dataset was previously described in the joint master thesis Rylander & Sterley (2022), but limited conclusions were drawn regarding the geological implications.

1.3 Relevance of Svalbard

Understanding the deep subsurface geology and the coinciding tectonic evolution of Svalbard is important for several reasons. On a regional scale it enhances insight into the tectonic development of surrounding regions in the circum-Arctic. On a local scale, detailed knowledge about the subsurface helps understanding other geological features and is important for ongoing research looking into increasing the sustainability of the local energy system.

Newly acquired knowledge and interpretations can be extrapolated to several areas outside of the archipelago. Traditionally, the region has been of interest for several operators looking for petroleum resources who were actively exploring the Barents Shelf situated towards the south and east (Jakobsson, 2018). As the rocks on Svalbard are the results of similar tectonic processes and overall geological evolution, it forms an analogue study area for the geology that can be expected offshore. More recent operations in the Barents Shelf have also been focusing on Carbon capture and storage (CCS). The Snøhvit CCS project has been in operation since 2008 (Ringrose, 2018) and subsurface investigation are currently ongoing for the Polaris CCS project (Horisont Energi, n.d.). Understanding the bedrock is essential for evaluating the potential and risk analysis of CCS, an element of the energy transition which is expected to become essential for the sustainability of Norway's future energy strategy (Egging & Tomasgard, 2018).

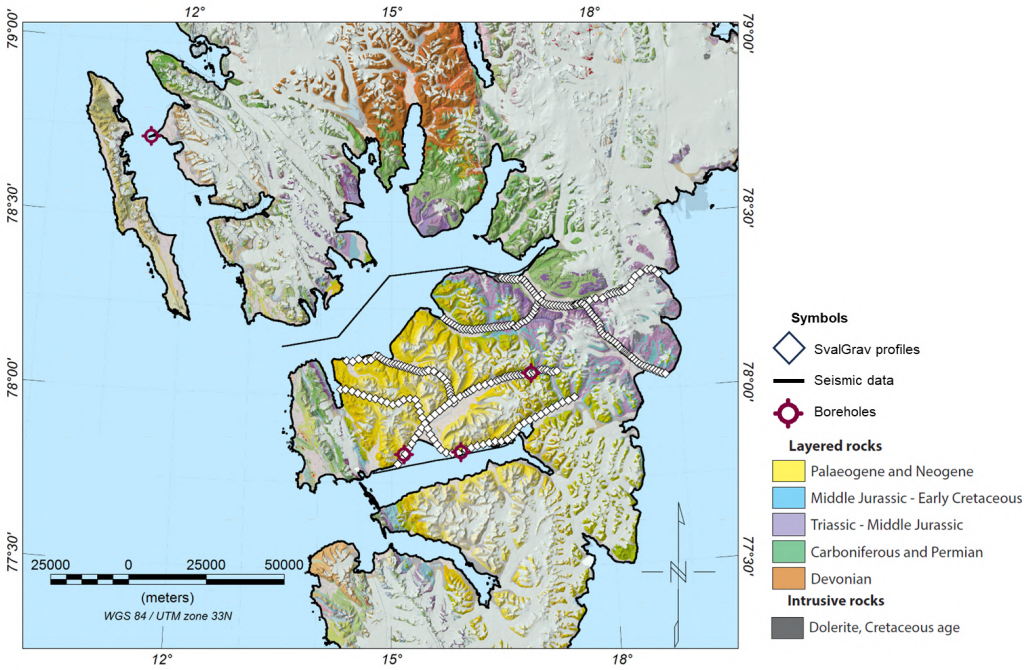

Figure 1.2: Geological map of Svalbard showing the 2022 SvalGrav survey profiles in white, used seismic lines in the fjords in black and relevant boreholes are indicated.

From a broader perspective, understanding the subsurface geology of Svalbard is relevant for several oceanic rift systems bounding Svalbard towards the north and west of which their opening is not fully understood, such as the Eurasia basin (Berglar et al., 2016) and the Knipovich ridge (Dumais et al., 2021), see Figure 1.1. Sea ice coverage in these regions makes traditional data collection, especially seismic surveys, challenging. A more detailed understanding of the Svalbard region can therefore help understand the tectonic development of these other regions. Another example of a regional tectono-magmatic element is the High Arctic Large Igneous Province (HALIP). This intrusion of igneous rock was found in various areas in the high Arctic and due to its magmatic nature, it is possible to observe its presence on potential field data (Senger & Galland, 2022). Knowledge on the emplacement of the HALIP on Svalbard will help understand the emplacement in other high Arctic regions, such as northern Greenland (Tegner et al., 2011) and Arctic Canadian islands (Bédard et al., 2021), where data acquisition is logistically and financially much more challenging.

Despite its remote location, when compared to other high Arctic regions, Svalbard is logistically relatively easily accessible. The settlement of Longyearbyen has a commercial airport open all year round and the presence of several research centers makes it an important hub for many scientists performing research in the Arctic. However, this research activity goes hand in hand with an increased need of sustainable energy sources. Currently, the energy system of Longyearbyen relies primarily on fossil fuels (coal and diesel) but efforts to incorporate more renewable sources of energy have been ongoing. The potential of CCS on Svalbard has been previously explored (Senger et al., 2015) and more recent research focuses on investigating the geothermal potential (Senger et al., 2023). Detailed knowledge about the subsurface is required for evaluating the risk coinciding with these operations as well as to understand the potential of the methods. Local knowledge about the subsurface structure in the direct surroundings of the village are of especial importance for the geothermal potential. This is because the proximity to the area of heat demand, therefore the area of distribution, is an important factor in the evaluation for geothermal potential.

As discussed in Senger et al. (2023), current plans for geothermal exploration around Longyearbyen are focused on using a deep borehole heat exchanger (DBHE) from a depth of 1.5-2 kilometers. However, there is also interest in investigating the potential of enhanced geothermal systems (EGS) (Schintgen, 2015) with a depth of up to 5 kilometers beneath Longyearbyen. For this operation a temperature of 150°C is required (Lund et al., 2008). This is expected to be reached at a depth between 3.5-4.1 kilometer. As this depth below Longyearbyen, one expects either Devonian sandstones or crystalline rock belonging to the basement (Senger et al., 2023). While the former would be able to form a potential geothermal reservoir, the latter basement rock would form an additional challenge for geothermal exploration.

1.4 Current knowledge gap

Cretaceous uplift has tilted Svalbard southwards with an angle of about five degrees (Senger & Galland, 2022). As a result, juxtaposed basement terranes offset by major fault zones observed in the north are covered by more recent sedimentary formations southwards. This limits our knowledge of the lateral continuation of fault zones, basement terranes and structural basins and highs. Additionally, limited seismic penetration depth and sparse borehole data are not sufficient to constrain the deep subsurface. Current interpretations at depth are mostly based on velocity models and seismic data.

Previous potential field studies in the region were mostly located in offshore regions and used these seismic refraction data as foundation for their research. Preliminary interpretations of potential field data onshore Svalbard have been established but are quite robust. No extensive data integration with the aim of further interpreting the anomalies has been done before. Therefore, the understanding of the sources of the different gravity and magnetic anomalies observed are limited and there are persistent knowledge gaps about how the subsurface geology can explain the potential fields.

1.5 Aims of the thesis

This thesis aims to resolve these knowledge gaps by enhancing the interpretation of the potential field anomalies observed on Svalbard. We use both local and regional potential field data to better understand the gravity and magnetic anomaly trends, and how they are linked to the subsurface geometry, density, and magnetic susceptibility structure.

To allow higher spatial resolution interpretations, we quantitatively analyze and quality control the new SvalGrav gravity data. Proven satisfactory, its input is combined with the airborne magnetic data and used as observed values for forward modeling. Along five key profiles, we construct forward gravity and magnetic models of the subsurface using Oasis Montaj software (Geosoft, 2006). Such a forward model simulates a response of the potential field data using relevant equations based on a user-input defined model and in such a manner creates synthetic data which can be compared to the observed values. It is used as a tool to test various scenarios to analyze which subsurface structure has the best fit to the observed anomalies. It should be noted that in essence the method of forward modelling is ambiguous as there are infinite ways in which the model can fit the data. Therefore, the models are constrained by various geological and geophysical sources. This includes seismic 2D lines, borehole logs, velocity models, hand samples and additional information obtained from literature.

The five profiles are selected based on the quantity and quality of the available data and their geological relevance. Four of the elected profiles cross one of the major fault zones, the Billefjorden Fault Zone (BFZ) which offsets Devonian sediments against crystalline basement. Some are overlaying regions where elements of the HALIP are observed. Both the fault zone and the tectono-magmatic province are expected to have a recognizable signature on the potential field data which makes them suitable candidates for further investigation in this study.

By quantifying the subsurface density and magnetic susceptibility structure necessary for explaining the potential field trends, we aim to enhance the knowledge of the subsurface and local understanding of the geology with a focus on:

- The extent of HALIP in Svalbard.
- Geological structures such as highs and basin.
- Major fault zones offsetting basement terranes.
- The need of intra-basement density and susceptibility changes.

This information is relevant for local geothermal exploration, understanding the tectonic development of the region and extrapolating interpretations to areas outside of the archipelago to enhance the regional understanding.

2 Study area and geological setting

2.1 Geological history

Svalbard is located at the outer NWN edge of the Barents Shelf (74–81° N and 15–35°E). The outcropping rocks have a large range of rock ages and lithologies, see Figure 2.1. For understanding the subsurface structure and regional trends in anomaly data, comprehension of the entire geological history of Svalbard is necessary. An overview of a stratigraphic column in Svalbard with the main stratigraphic units and tectonic events can be found in Figure 2.2 which was adapted from Olaussen et al. (2023). An extensive overview of the geological history of Svalbard can be found in Dallmann (2015).

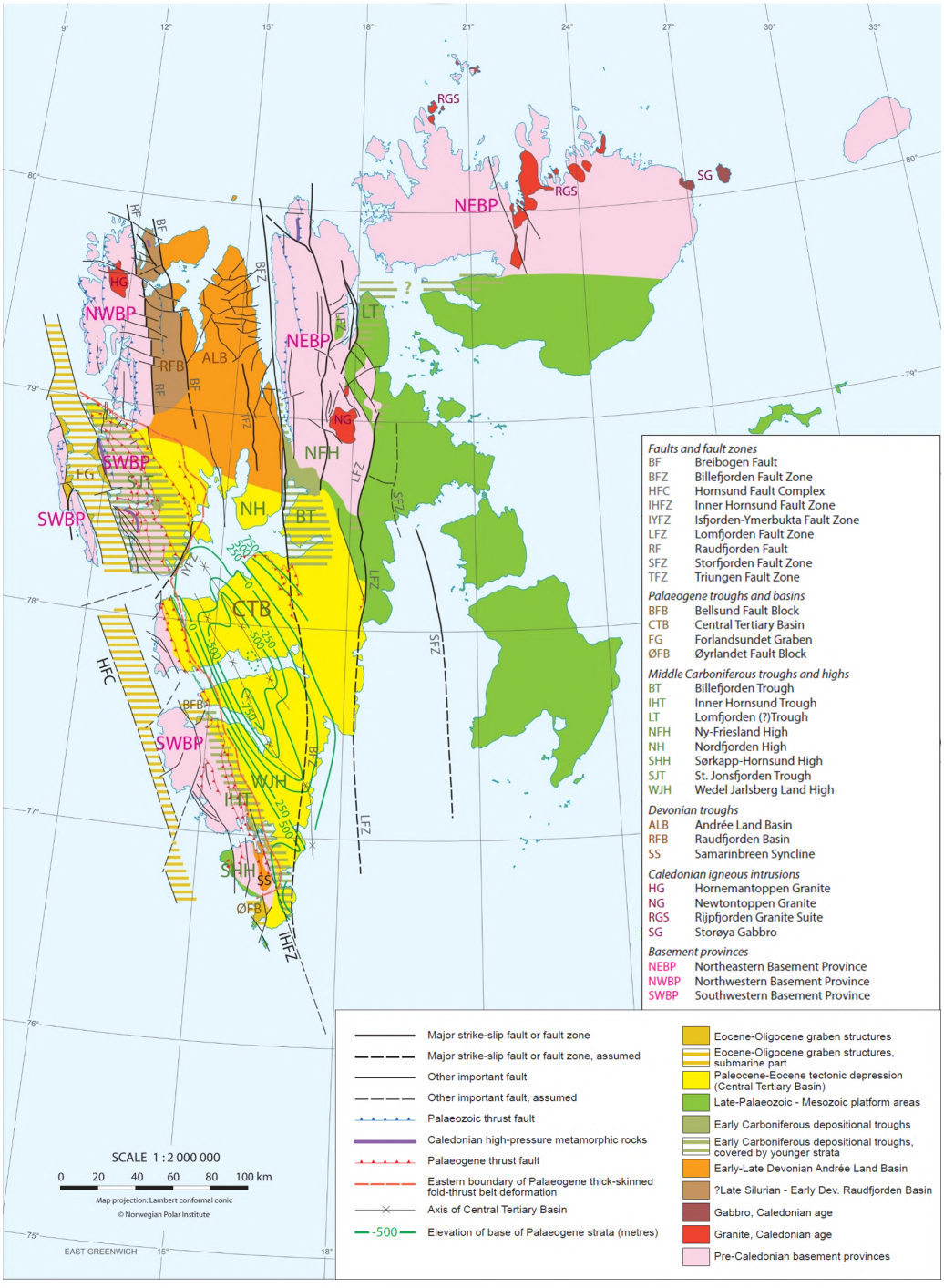

Figure 2.1: Main tectonic elements of Svalbard from Dallmann (2015). The various basement provinces are indicated, as well as the major N-S trending fault zones.

The basement of Svalbard is defined as the Pre-Caledonian rocks and exists out of 3 distinct basement provinces which are separated by NNW-SSE striking long-lived tectonic lineaments, see Figure 2.1 (Dallmann, 2015). The Proterozoic rocks are outcropping in the north and west of Svalbard. The Northeastern Basement Province (NEPB) exists out of the Nordaustlandet terrane and the Western Ny-Friesland terrane (Figure 2.1). The Western Ny-Friesland terrane exists in the lower part out of 5 thrust sheets made up of Paleoproterozoic granitoids. They are overlain by Mesoproterozoic metasedimentary rocks. There is a thick sequence of gneisses and supracrustals which were exposed to metamorphism and deformation during the Caledonian orogeny (Witt-Nilsson et al., 1998). The Nordaustlandet terrane consists of granitoids and supracrustals (Johansson et al., 2005). These two NEPB terranes are separated by the Veteranen fault (Harland et al., 1992), part of the Lomfjorden Fault Zone (LFZ). The Billefjorden Fault Zone is the western border between the NEPB and the Devonian Basin. The Northwestern Basement Province (NWBP) is located on the western side of the Devonian basin and exists out of two metamorphic terranes (Figure 2.1). The Biskayarhalvøya Terrane and the Albert I terrane (Gee & Teben'kov, 2004). The third province is the Southwestern Basement Province (SWBP) and is present along the west coast of Svalbard (Figure 2.1) (Gasser & Andresen, 2013). The eastern edge of the SWBP is not observed as it is overlain by post-Caledonian sediments. The SWBP is located along the Hornsund Fault Complex (HFC) which was a continental transform fault between Svalbard and Greenland (Lepvrier, 2000).

It is thought that the basement terranes of the provinces were juxtaposed during the Caledonian orogeny resulting from the collision between Laurentia and Baltica (Lyberis & Manby, 1999).

Resulting from the orogenic collapse of the Caledonides, the Devonian sediments were deposited in an intramontane terrestrial basin. Svalbard was located around the equator at the time of the Devonian, resulting in a hot and arid climate with gradual expansion of vegetation on land. Lack of proper soils facilitated high levels of weathering and erosion (Dallmann, 2015). The present day, the Devonian succession can be found on two fault blocks, the Raudfjorden in the west and the Andrée Land in the east. The Raudfjorden fault block consists of the Early Devonian sediments formed in a high-relief hinterland setting leading to the deposition of coarse-grained braided river and alluvial fan system sediments of the Red Bay Group, see Figure 2.2, (McCann, 2000). The Andrée Land fault block is composed of the Andrée Land Group (Figure 2.2), with fine-grained sediments deposited in a low-relief hinterland setting and semi-arid climate (Friend et al., 1966). The Mimerdalen Subgroup, which is the uppermost Devonian, is thought be deposited in small foreland basins related to the transpressional deformation of the Late Devonian Svalbardian tectonic phase (Piepjohn & Dallmann, 2014). The Andrée Land Fault Block is bordered by the BFZ in the east and the Breibogen Fault in the west and the Raudfjorden fault is the western boundary of the Raudfjorden fault block. It is discussed if the extent of the Devonian Basin was significantly larger than currently preserved. Devonian sediments have been observed further west of the Raudfjorden. As the Andrée Land Group sediments are not indicative of deposition near a basin-margin, it is thought to have extended a lot further east than the current BFZ border (Dallmann, 2015). The southward continuation of the Devonian basin is mostly covered by post-Devonian sediments. The Devonian succession is exposed in southern Spitsbergen and folded into the Samarinbreen Syncline (Dallmann, 1992). Recent research argues that the Devonian sediments were formed in a supradetachment basin, with the outcropping basement rock being a metamorphic core complex (Braathen et al., 2018).

At the end of the Devonian, Svalbard was affected by the Svalbardian event which was transpressional and linked to the Ellesmerian event (Piepjohn, 2000). This caused the Western Ny-Friesland basement to be thrusted onto the Devonian sediments along the Baliolbreen fault, the western fault of the BFZ (Bergh et al., 2011). Strata of the Lower Billefjorden Group (Figure 2.2) was deposited in an interior continental basin as a result of initial subsidence during the Late Devonian - Early Carboniferous (Braathen et al., 2012; Smyrak-Sikora et al., 2021). These were mostly fluvial and deltaic deposits with coal beds, indicators of the tropical and humid conditions during the deposition of the Billefjorden Group (Gjelberg & Steel, 1981).

This succession was followed by Carboniferous rifting which led to several fault-bounded basins being formed on Spitsbergen. There was a shift to a warm and arid climate (Steel & Worsley, 1984). The best studied basin is the half-graben at the Billefjorden Trough formed at the hanging wall of the BFZ (Smyrak-Sikora et al., 2019; Smyrak-Sikora et al., 2021). The syn-rift deposits belong to the lower Gipsdalen Group (Figure 2.2), with multiple isolated and fault-bounded rift troughs. In the lower Gipsdalen Group, there is a transition from continent to marine environment deposits. Basal clastic red beds are overlain by the Ebbadalen formation, with alluvial fans in the proximity of the fault zone which are distally interfingering with siliciclastics, mixed carbonites and evaporites. The late rift and early post-rift sediments consist of siliciclastics and carbonates of an open to restricted, shallow-marine shelf (Olaussen et al., 2023; Dallmann, 2015).

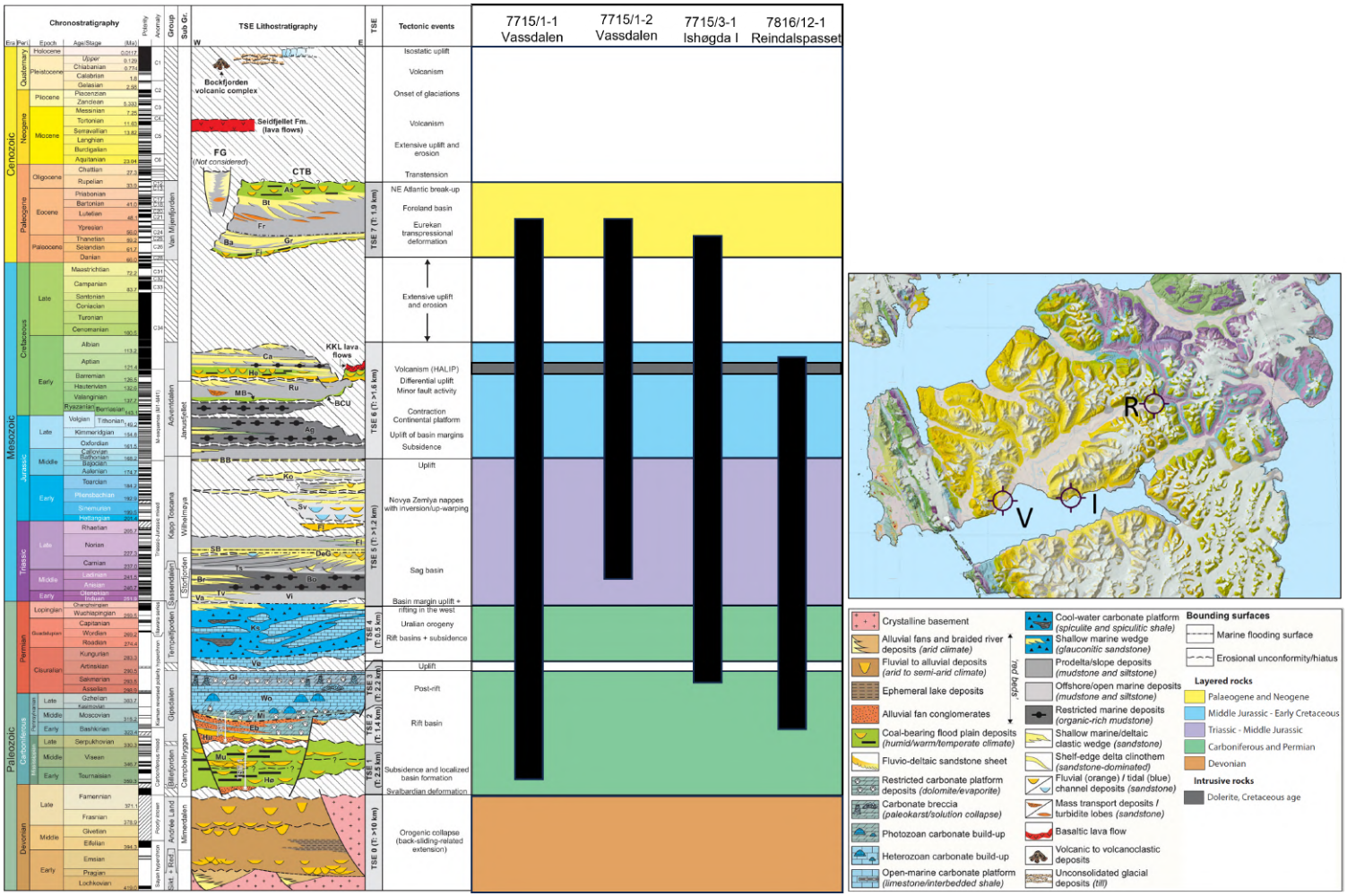

Figure 2.2: Chronostratigraphic and lithostratigraphic column and legend adapted from Olaussen et al. (2023). The main tectonic events affecting the geology of Svalbard are shown. The wireline coverage and location of 4 boreholes are plotted. Vassdalen II and Vassdalen III were drilled in the same region. Borehole abbreviations: I, Ishogda; R, Reindalspasset; V, Vassdalen.

As the rifting phase ceased and subsequent subsidence followed, this led to an increase in the relative sea level and the deposition of a long-lived shallow-marine carbonate platform of the Wordiekammen Formation belonging to the Upper Gipsdalen Group (Ahlborn & Stemmerik, 2015; Smyrak-Sikora et al., 2021). After the deposition of the carbonates of the Gipshuken Formation (Blomeier et al., 2009), there was a short phase of uplift resulting in an erosional unconformity (Stemmerik, 2008).

The North Atlantic rift located between Greenland and the Barents Sea led to a phase of renewed extension in the Late Permian (Seidler et al., 2004; Clark et al., 2014). Temperate to cold water siliceous-carbonate ramp deposits of the Tempelfjorden Group (Figure 2.2) were formed (Blomeier et al., 2013). Cold-water carbonate platform deposits were a result of the northward drift in latitude of Svalbard. A stable tectonic platform was present which lasted until the late Jurassic.

Regional subsidence in the Early Triassic to Middle Jurassic led to the creation of a sag basin which was primarily filled with siliciclastic deposits (Olaussen et al., 2023). A NW-prograding delta originating from the Fennoscandian shield and Uralide mountains in the Middle to Late Triassic was the main source for these sediments of the Sassendalen and lower Kapp Toscana Group (Figure 2.2) (Klausen et al., 2019).

Around the transition from the Triassic to the Jurassic, the basin configuration changed. Compression from the Novaya Zemlya Orogeny resulted in the inversion of old basement faults and led to uplift in the west. Subsequent foreland basins were formed in the east, where the stratigraphic succession is still mostly complete. Contrary, a large part of the Kapp Toscana Group is missing in the west (Müller et al., 2019).

The Early Cretaceous Adventdalen Group (Figure 2.2) forming a continental siliciclastic platform was deposited as a result of regional subsidence in southern Svalbard and uplift in the north (Olaussen et al., 2023). In the early Cretaceous the HALIP was emplaced as a result of circum-Arctic magmatism and possibly related to the opening of the Amerasian basin (Døssing et al., 2013). The magmatism was linked to thermal doming (Ineson et al., 2021), which tilted the Svalbard platform southwards and resulted in significant uplift (Senger & Galland, 2022).

Reworked pollen found in Paleogene deposits is the only evidence that has been found which suggests the presence of Upper Cretaceous strata on Svalbard (Smelror & Larssen, 2016). The large hiatus of the Upper Cretaceous is explained by exhumation due to uplift resulting from magmatism and the opening of one of the major basins north of Svalbard, the Amerasian basin (Maher, 2001).

Dextral movement occurred between the Greenland and Eurasian plate in the Paleocene. This was linked to the Eurekan phase of deformation. Crustal shortening was the result of induced transpression (Bergh et al., 1997) and this led to the formation of the West Spitsbergen Fold and Thrust Belt (WSFTB) and its corresponding foreland basin, the Central Spitsbergen Basin (CSB) (Steel et al., 1981). This basin is filled by the Van Mijenfjorden Group (Figure 2.2) which exists out of coastal plain to deep water basin siliciclastics (Helland-Hansen & Grundvåg, 2021). These Paleogene and Neogene rocks are mainly located in central and southern Spitsbergen, as seen in Figure 2.1.

In the Neogene there is another major hiatus which is linked to the onset of oceanic spreading and crustal thinning west of Svalbard (Green & Duddy, 2010). In the last million years Svalbard has also been heavily influenced by phases of glaciation with subsequent glacial erosion and post-glacial isostatic uplift (Lasabuda et al., 2021). Uplift estimates of the region are in the range of 2.5-3.5 kilometer (Olaussen et al., 2023). This has led to the exhumation of many well-consolidated and compacted sediments on Svalbard, giving them high density properties.

From this geological history, there are several points of especial importance for our research. The basement is a juxtaposition of various provinces and terranes, where intra-basement density and susceptibility contrasts are possible. Basins of both Devonian and Carboniferous age can be expected in the subsurface. Overlying sediments vary between carbonates and siliciclastics and have high densities to due Neogene uplift. The emplacement of the HALIP has led to the intrusion of igneous rock which can influence the subsurface magnetic susceptibility.

2.2 Study area

The study area of the current research encompasses the entire Svalbard archipelago for determining regional trends and focuses on Central Spitsbergen for understanding of local anomalies. Figures 2.3 and 2.4 show the magnetic and gravity anomalies of the study area, respectively. The blue squares indicate the location of the gravity profiles. Interpretations from the main anomalies discussed below were retrieved from Dallmann (2015).

The Atomfjella complex is part of the West Ny-Friesland terrane and has a high-metamorphic grade causing positive anomalies in both gravity and magnetics (A). In Isfjorden, the magnetic short wavelength signal is thought to originate from shallow intrusions (Skilbrei, 1992) but no explanation has been found for the large wavelength magnetic anomaly (B), for which there is no corresponding gravity anomaly. Highs in magnetic and gravity in the east are linked to dolerite intrusions (C). The CSB, resulting from the WSFTB, has a thicker sedimentary package pushing denser rocks downwards causing a large negative anomaly dominating the gravity signal (D). The thin NW-SE trending positive magnetic anomalies in the south (E) are thought to be linked to major fault zones but have an unsatisfactory match with the expected location. A local high in both magnetic and gravity signal is found at the end of two gravity profiles (F). A high in gravity and magnetic signal (G) north of Dicksonfjorden is thought to be linked to shallow placement of the basement.

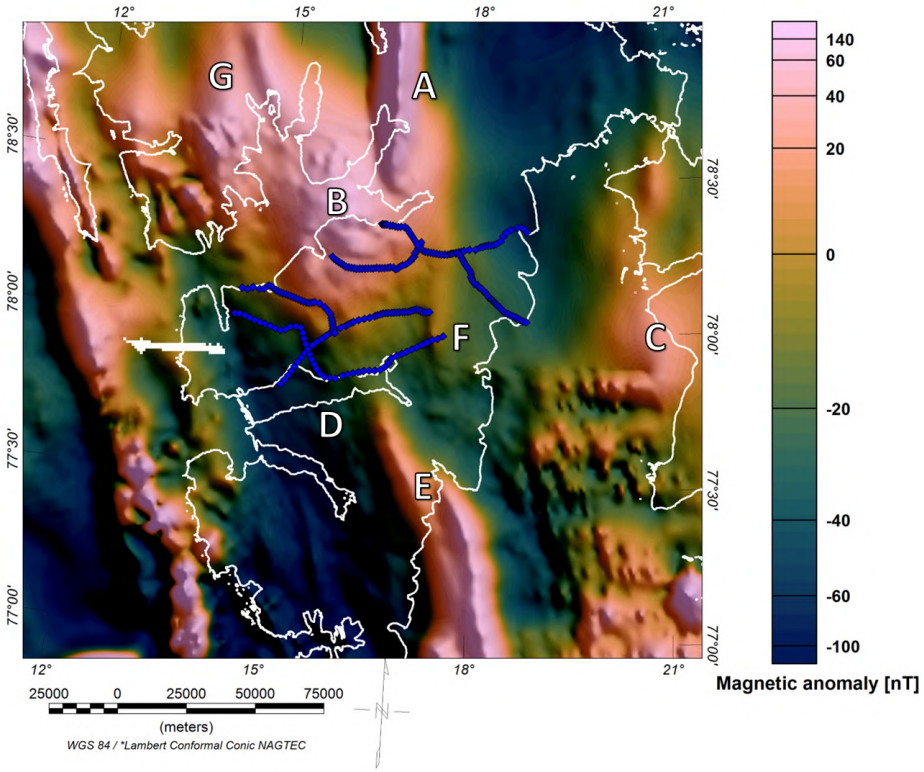

Figure 2.3: Overview of the magnetic anomalies in the study area. Blue squares indicate the location of the gravity profiles. Annotations: A = Atomfjella Complex, B = major Isfjorden anomaly, C = dolerite intrusions, D = CSB, E = NW-SE magnetic highs, F = local magnetic high, G = basement.

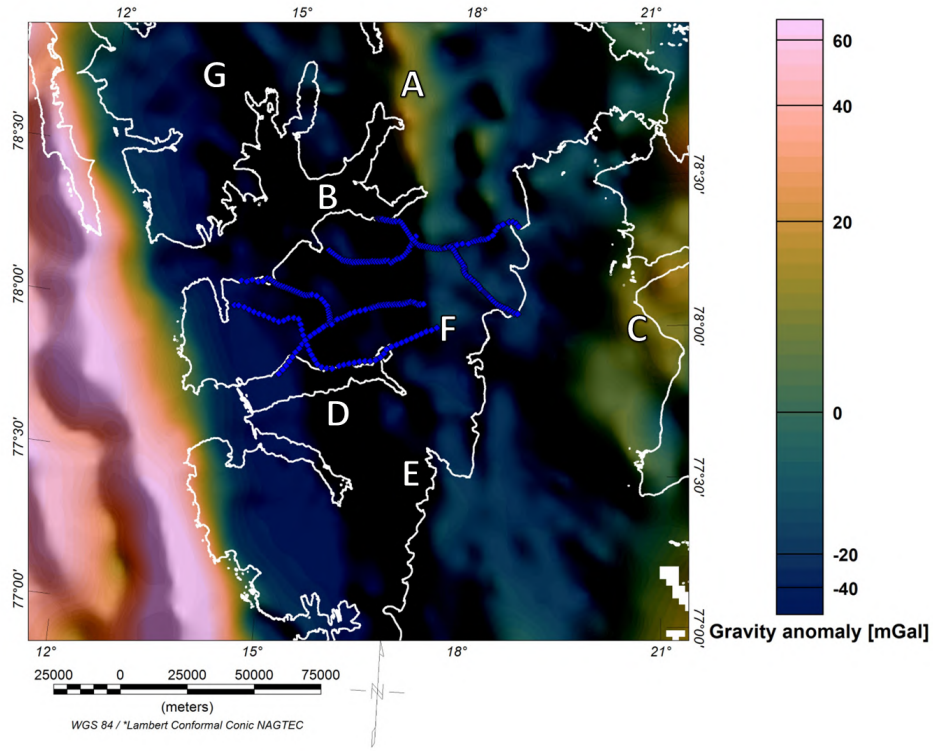

Figure 2.4: Overview of the gravity anomalies in the study area. Blue squares indicate the location of the gravity profiles. Annotations: A = Atomfjella Complex, B = major magnetic Isfjorden anomaly, C = dolerite intrusions, D = CSB, E = NW-SE magnetic highs, F = local high, G = basement.

3 Geophysical background

3.1 Gravity

Gravity is the universal force of attraction between various bodies of mass. It has a potential field described by a scalar potential function and satisfies the LaPlace equation. The gravitational force corresponds to the following formula:

$$F = G\frac{m_1 m_0}{r^2}\mathbf{r} \tag{1}$$

where G is the gravitational constant of $6.672 \cdot 10^{-11} Nm^2kg^{-2}$, m_1 and m_0 describe the mass of the particles, r is the distance between the two particles and $\mathbf{r}$ is the unit vector from m_0 towards m_1. In general, gravity is measured in the vertical direction from the body surface. The gravitational acceleration on the Earth's surface is approximately 9.8 m/s^2 which is equal to 980 Gal. However, the range of gravity values is 9.78-9.83 m/s^2 depending on elevation and latitude (Moritz, 1980).

The gravitational acceleration at the subsurface is measured with a gravimeter. For land acquisition surveys, such as SvalGrav, a Lacoste-Romberg gravimeter (Lacoste, 1967) is often used. It measures the gravity relative to a base station where absolute measurements are taken. The fundament of the Lacoste-Romberg gravimeter is a spring with a mass connected which is at zero-length when it is in equilibrium. Gravitational changes effect the pull of the mass on the spring, allowing one to detect changes in the gravitational field of up to 0.01 mGal precision for both positive and negative anomalies (Lacoste-Romberg, 2004). Besides land surveys, gravity data is also collected with various other data acquisition platforms. It is possible to collect data with ships, as well as data from satellite and aerial surveys.

The geoid is the equipotential gravity surface, a surface with a constant gravity value. Gravity anomalies are deviations from this expected value caused by lateral variations in mass. To obtain anomalies which are solely resulting from subsurface density contrasts, several corrections need to be applied to the data. From a temporal perspective, effects of instrumental drift and the tidal pull during the moment of acquisition should be considered. On a global scale, the effect of the latitude and the regional isostasy are relevant. A terrain correction accounts for the pull of surrounding topographic highs and lows. Finally, the elevation at the station is used to determine the free-air and the Bouguer anomaly.

Corrections

To obtain anomalies based on collected gravity measurements multiple corrections are necessary. Both factors influenced by the timing of the measurements, as the regional scale and local scale are relevant.

The readings of an instrument can change over time due to internal factors. Elastic creep in a spring or a change in temperature can affect the resulting gravitational measurements. By taking measurements in the same location at the start and end of every acquisition day, it is possible to correct for this drift. The time at which the measurements was taken is also important as the gravity on Earth is affected by the pull of the moon, creating a tidal effect which needs to be corrected. However, this is slow enough that it can be calibrated using the same measurements necessary for the instrumental creep correction.

The ellipsoidal shape of the Earth means the radius reduces towards the polar regions. As the gravity acceleration is inversely proportional to the square of the distance between two masses, see equation (1), this acceleration is latitude-dependent and higher at the poles. Additionally, the higher equatorial centrifugal force caused by the spinning of the Earth opposes the gravitational force. It is therefore important to apply a latitude correction (g_ω) according to the latest model (Dumais, 2021; Dentith & Mudge, 2014):

$$g_\omega = 9.7803267714\frac{(1 + 0.00193185138639\sin^2\omega)}{\sqrt{1 - 0.00669437999103\sin^2\omega}} \tag{2}$$

where ω is the latitude in degrees.

Data acquired on a moving platform requires an additional Eötvös correction (g_E). The moving platform velocity affects the centrifugal acceleration outwards and can be compensated using the following formula (Glicken, 1962):

$$g_E = 4.040Vcos\omega sin\alpha + 0.001211V^2 \tag{3}$$

with V being the velocity in km/hr, ω the latitude and α the azimuth of the movement. As apparent from the formula, data collected in east-west strike is the most affected by this effect. Detailed and precise

data of the speed and direction during acquisition is therefore important for correct processing. As land surveys are static, the velocity of the platform is zero and g_E is also equal to zero.

For understanding height correction nomenclature about Earth's surfaces is necessary. As seen in Figure 3.1, the surface of the Earth can be divided into the topography, the geoid, and the ellipsoid. The geoid is the equipotential surface equal to the mean sea level. Elevation (h) is the difference between the topography and the geoid and useful for geodetic application. However, for geophysical applications, one is interested is the different between the topography and the equipotential ellipsoid of revolution (H). This ellipsoid is based on a mathematical approximation of the Earth. Due to the smoothness of the geoid, the difference is often negligible, but it is important to be aware of which elevation measurement should be used for the corrections (Li & Götze, 2001).

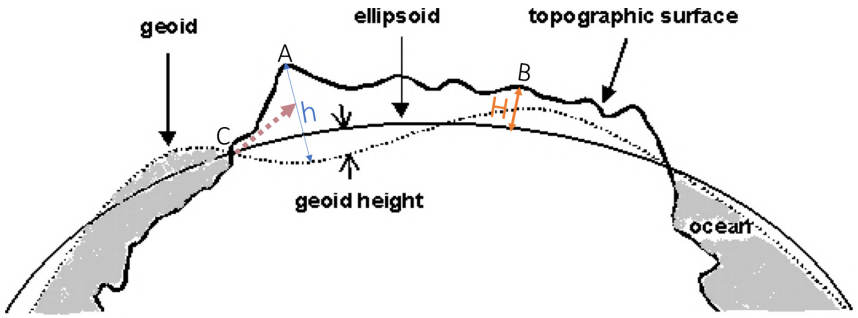

Figure 3.1: Figure indicating the nomenclature of Earth's surfaces. The geoid is the equipotential gravity surface equal to the mean sea level and the ellipsoid is the mathematical expression of the equipotential ellipsoid of revolution. The difference between the topography and the geoid (h at A) is the elevation useful for geodetic purposes. For geophysical usage, the difference between the topography and the ellipsoid (H at B) is relevant. This elevation can be used for computing the free-air and Bouguer correction. The dashed pink arrow at C indicates how a nearby topographic high exerts an upward gravitational pull on the local gravitational acceleration.

The gravitational acceleration reduces with height, an effect described with the free-air correction. It compensates for the difference between the topography and the ellipsoid, as indicated by H in Figure 3.1. An air layer with negligible density and therefore mass is assumed to be situated in between, giving the following formula (Li & Götze, 2001):

$$g_{FA} = \frac{2GM_E}{R_E^3} \cdot h = 0.3086 \cdot h \tag{4}$$

where g_{FA} is the free-air correction, G the gravitation constant, M_E the mass of the Earth, R_E the radius of the Earth and h the ellipsoid height.

Continuing on this free-air correction, it is possible to compute the simple Bouguer correction (g_{SB}) by interchanging the previously assumed air layer with an infinite homogeneous and horizontal slab of rock. This correction compensates for the effect of this mass on the measurement and can be computed with the following formula:

$$g_{SB} = 2\pi G\rho h \tag{5}$$

with G the gravitational constant, ρ the density of the slab and h the thickness of the slab. Typically, the average density of crustal rocks (2670 kg/m^3) is used (Blakely, 1995).

Laterally, gravity measurements are affected by topographic highs and lows exerting a higher or lower pull on the station measurements, respectively. This is indicated at C in Figure 3.1, showing the upward gravitational pull caused by the proximal high in elevation. The magnitude of this terrain effect is dependent on the vicinity and height of the topographic elements. It is negligible in flat lands but can be up to a couple of mGal in regions with medium-high topography. An additional terrain correction (g_T) can be added to the simple Bouguer and gives the complete Bouguer correction (g_{CB}).

$$g_{CB} = g_{SB} + g_T \tag{6}$$

Determining the terrain correction requires a high-resolution Digital Elevation Model (DEM) and sufficient computing power. An additional challenge in Polar regions such as the Arctic is that the topography is not solely a result of the bedrock, but also due to layers of snow and ice. As these materials have a significantly lower density than rocks, information about the thickness of these layers is required for a reliable terrain correction.

Additional isostatic corrections (g_I) can be calculated to remove the effect of isostatic compensation due to tectonic flexure of the crust. For this, it is important that the region is in an isostatic balance, as it will otherwise introduce more error into the data.

Taking all these corrections into consideration, we find the following anomaly values. The free-air anomaly (G_{FA}) is:

$$G_{FA} = G_{obs} - g_\omega - g_E - g_I - g_{FA} \tag{7}$$

with G_{obs} the observed gravity value. The Bouguer corrected anomaly (G_{BC}) is:

$$G_{BC} = G_{obs} - g_\omega - g_E - g_I - g_{FA} - g_{SB} - g_T = G_{FA} - g_{SB} - g_T \tag{8}$$

3.2 Magnetics

Magnetic susceptibility describes the relationship between the applied field and the induced magnetization in a material (Tauxe, 2010). The susceptibility of a rock depends on the concentration of ferromagnetic particles, particles such as iron which can save a magnetic signal. In general, metamorphic and igneous rocks are more magnetically susceptible than sediments.

Lateral fluctuations in magnetic susceptibility led to spatial variations of the intensity of the magnetic field. The magnetic field is conceptualized as (Dumais, 2021)

$$\mathbf{B} = \frac{\mu_0}{4\pi}\frac{p_1 p_2}{r^2}\mathbf{r} \tag{9}$$

where $\mathbf{B}$ is the magnetic field, μ_0 is the permeability of free space, p_1 and p_2 describe the strength of the poles of a magnetic dipole and r is the distance between the magnetic dipole and the measurement location.

The magnetic field is a potential field from which the changes can be measured using a magnetometer. Fluxgate magnetometers are primarily used in aeromagnetic surveys and consists of iron cores wrapped by coils. Alterations in the continuously generated hysteresis loops are detected and provide information about the magnetic field (Dumais, 2021).

To obtain anomalies solely due to subsurface features, it is important that the magnetic noise is reduced and that temporal variations are considered. Logging the timing of acquisition is of especial importance, as hourly fluctuations in the Earth's magnetic field strength caused by magnetic storms must be compensated in magnetic surveying. As in the current study no new magnetic data is considered, it is not within the scope of the study to discuss the other corrections and the reader is referred to Dumais (2021) for a more detailed description on magnetic processing.

3.3 Edge and depth detection

Enhanced filters applied to potential field grids can help identify the edge and depth of the anomaly sources. A tilt derivative is the ratio between the vertical gradient and the absolute horizontal gradient:

$$\theta(x,y) = \tan^{-1}\frac{\frac{\partial f}{\partial z}}{\sqrt{(\frac{\partial f}{\partial x})^2 + (\frac{\partial f}{\partial y})^2}} \tag{10}$$

where θ the tilt derivative, f is the potential field, the numerator is the vertical gradient and the denominator the absolute horizontal gradient. It is positive over the source of the anomaly, near-zero at the edge of a source and negative elsewhere (Miller & Singh, 1994). An advantage of this method is that the dependence on the potential field is identical for both gradients, meaning that it allows the imaging of both weak and strong sources.

As discussed in Blakely et al. (2016), for a simple vertical contact equation (10) becomes:

$$\theta = \tan^{-1}(x/z), \tag{11}$$

with θ the tilt angle, x the horizontal distance to the contact and z the depth of the source. This simplification can then be used to compute the tilt depth, a variable which indicates at which depth the anomaly is situated. If x is identical to z, the tilt angle is $\pi/4$. By measuring the distance between the zero-contour and the $\pi/4$-contour, the depth of the source is estimated. The GEOSYS software utilizes this tilt depth method of Salem et al. (2008) for computing the tilt depth. The advantage of this

depth determination method over other methods is that there is no need for adding parameters such as susceptibility and structural indexes, making the results more objective.

The maximum depth of the magnetic sources can be constrained by determining the Curie depth. This depth is equivalent to the isotherm of the Curie temperature, which is the threshold temperature above which a material loses it magnetic signature. For magnetite, the main magnetic material in most of the Earth's rocks, this temperature is 580 degrees Celsius. Above this temperature, the material state is determined by the thermal domain.

3.4 Seismic methods

Seismic methods use acoustic waves to improve our understanding of the subsurface. Each subsurface layer has a certain acoustic impedance determined by the product of the density and the seismic velocity of the layer. Boundaries with contrasts in this impedance causes the waves to reflect and refract, returning them to the surface where they are recorded. Seismic acquisition where an artificial source (dynamite, a vibroseis truck or a sledgehammer) is used to initiate seismic waves are active source surveys. Passive source surveys instead use naturally occurring or ambient seismic waves such as earthquakes or ocean waves.

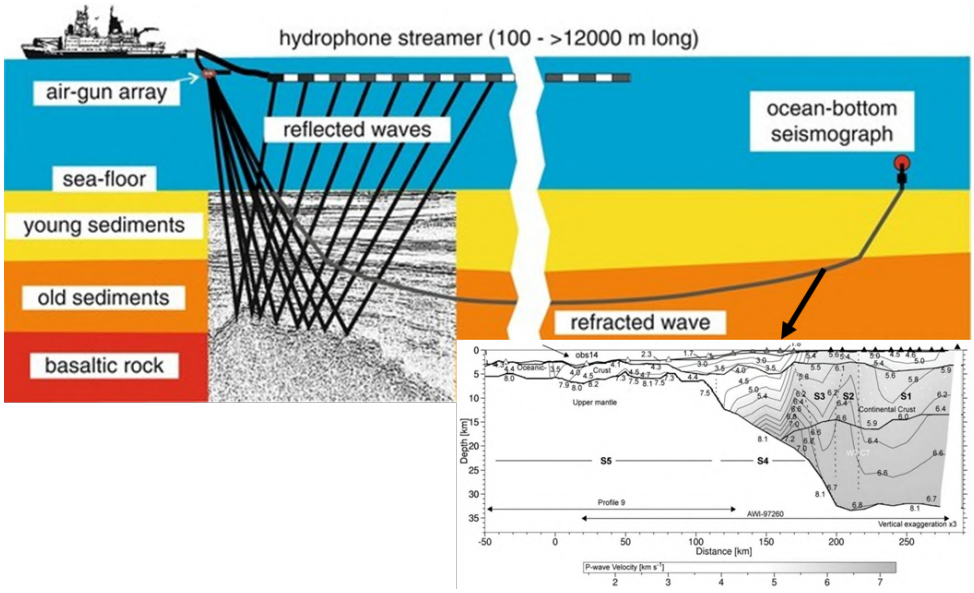

Figure 3.2: Short offset reflected waves are used for constructing seismic stacks giving insight into the subsurface structure. Long offset data from refracted waves can be used to construct velocity models. Figure adapted from Hübscher & Gohl (2014) and Ritzmann et al. (2002).

For seismic reflection studies, the offset between the source and the receiver is generally small allowing the capturing of acoustic waves reflected of a subsurface layer as illustrated in Figure 3.2. The larger the contrast in acoustic impedance between two layers, the clearer the seismic reflector. Seismic reflection data can be collected both onshore on land and offshore. The onshore surveys use dynamite or vibroseis as a point source for seismic signal and geophones or snow streamers as receivers. Marine surveys often use airguns as a source and hydrophone streamer toed behind the vessel as a recorder. After processing, the seismic reflection data can be turned into a seismic stack resembling the subsurface below a profile. This stack is in the two-way traveltime (TWT) domain and can be used for making seismic interpretations of the subsurface, identifying seismic reflectors as boundaries of various lithostratigraphic formations and faults. In the current research both onshore and offshore seismic data was utilized, see Table 4.3.

The imaging of subsurface elements is theoretically limited to objects which are equal or larger than a quarter of the wavelength of a seismic wave. As the acoustic wave moves further from its source, its energy decreases due to attenuation and increased scattering, decreasing the wavelength and subsequently the imaging resolution. Additionally, heterogeneity in the seismic velocity of sedimentary layers due to lithological differences can lead to increased waveform distortion again lowering the seismic resolution.

The aim of seismic refraction studies is to obtain information about the subsurface seismic velocity and boundaries at depth. As illustrated in Figure 3.2, due to the horizontal propagation of refracted waves, these surveys require a larger offset between source and receiver to have a useful penetration depth. Data obtained from these studies can be used for constructing velocity models by tomographic inversion.

Arctic seismic surveying

The acquisition of seismic data in an Arctic environment such as Svalbard, brings along additional logistical and processing challenges. In the proximity of sea ice, marine seismic acquisition becomes a lot more challenging as the towed streamers are vulnerable and require a constant velocity. Onshore surveys are more feasible, however the study area is often remote and only reachable by snow scooter and bandwagon. The usage of vibroseis trucks is nearly impossible, resorting to the usage of detonating cord (Dynacord) as an active source and a snowstreamer for the recording of the data (Johansen et al., 2011). The setup of such a survey can be seen in Figure 3.3.

The quality of the Arctic seismic data collected is impacted by the presence of permafrost. Frozen sediments have significantly different elastic properties, increasing the seismic velocity and therefore reducing the resolution (Johansen et al., 2003). Additionally, stronger surface waves are generated which decrease the signal to noise ratio. However, an advantage of the Arctic seismic surveying are the low levels of ambient noise due to the remoteness.

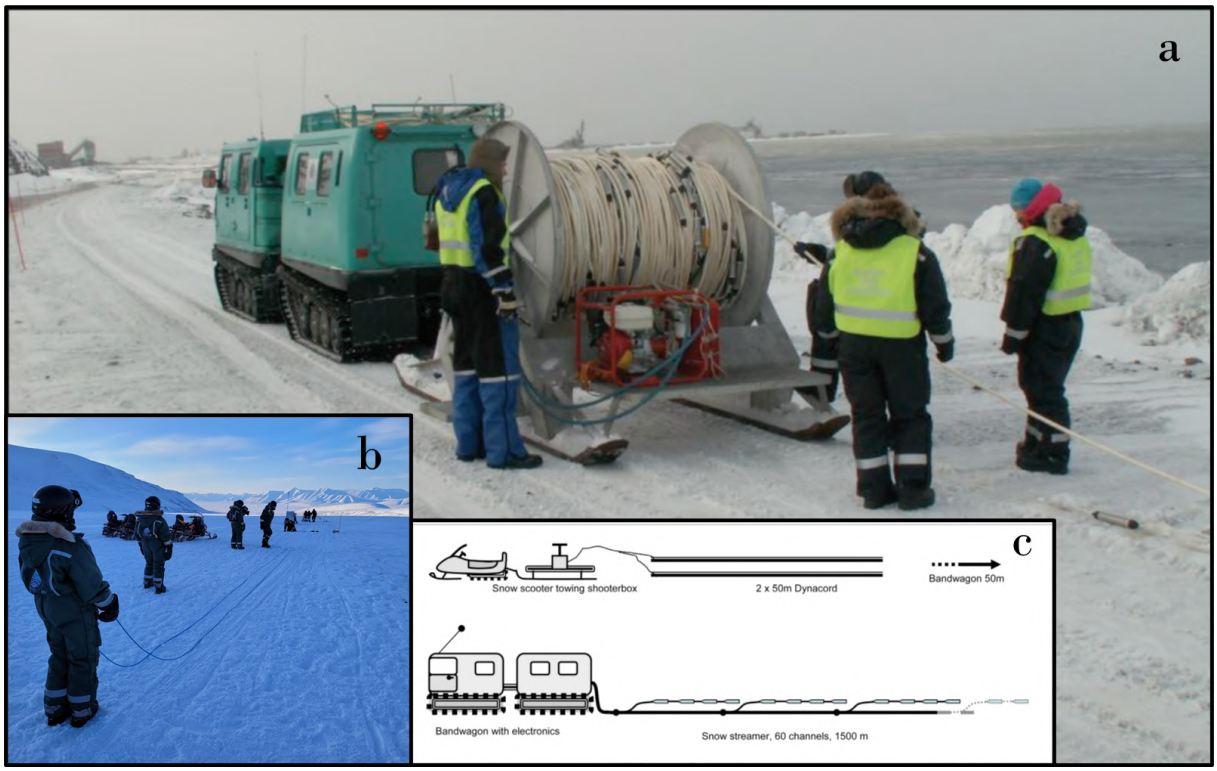

Figure 3.3: Setup of a seismic acquisition survey in the Arctic. a) The layout of geophones from a snowstreamer dragged by a bandwagon. b) Students of the AG-351/851 UNIS course placing detonating cord (Dynacord) on Slakbreen glacier south of Reindalen. c) Illustration of the seismic acquisition setup showing the snowstreamer of Figure a and the Dynacord of Figure b. Figure a and c are adapted from Bælum et al. (2012).

4 Data and methods

Regional ground- and air-based data were used to understand the large trends of the potential field anomalies in Svalbard. We integrated observations from a new gravity survey with complementary geological and geophysical data sources to constrain forward models of the subsurface along five key profiles.

4.1 Regional trends

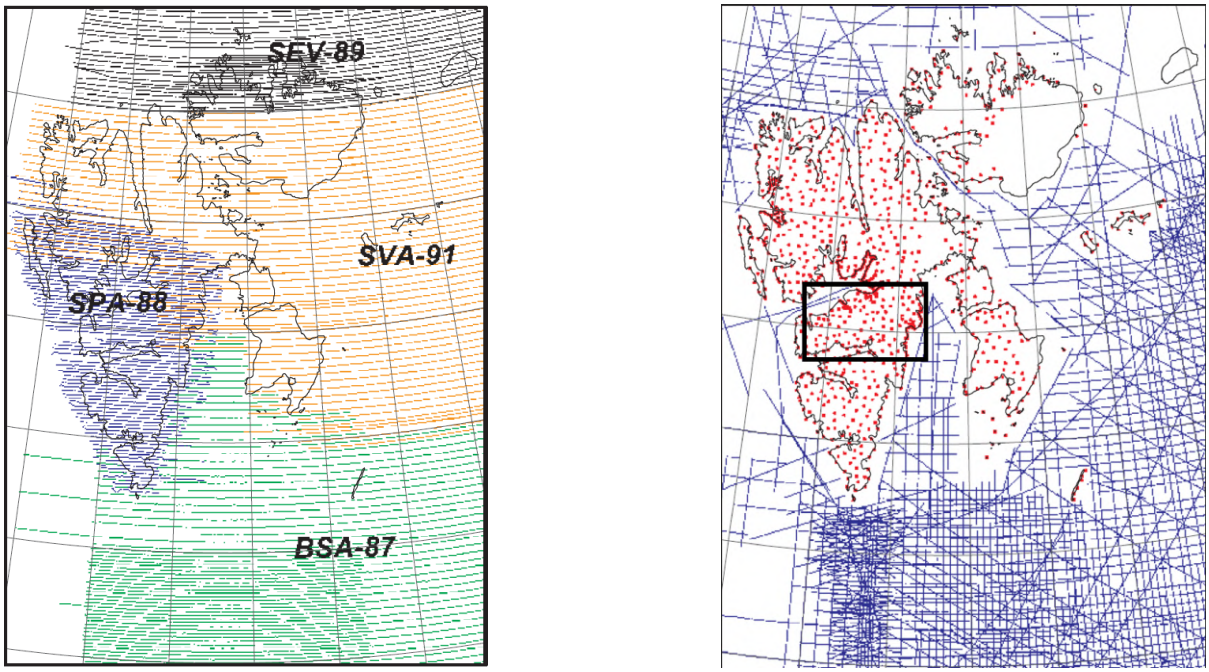

(a) Overview of 4 aeromagnetic surveys flown over Svalbard which were included in the compilation of the magnetic anomaly map. Details of the surveys can be found in Table 4.1.

(b) Overview of the data sources included in the gravity map. Red dots indicate the land stations where the blue lines are the marine profiles. Black box indicates the location of the SvalGrav survey as shown in Figure 4.3.

Figure 4.1: Data sources for the magnetic (a) and gravity data (b). Figures from Dallmann (2015).

4.1.1 Regional potential field data

Magnetics

Information about regional magnetic anomalies was retrieved from a Regional Aeromagnetic Map of NGU presented in Figure 4.2a. The map is a compilation of various aeromagnetic surveys completed on Svalbard and its direct offshore area, see Figure 4.1a and Table 4.1. The KRAS survey from 2016 was part of the compilation but is not included in Figure 4.1a. It was primarily located above the Fram Strait (Dumais et al., 2020). Additional data from more distant surveys were used in the compilation of the map but were outside the scope of the current study (Jokat et al., 2008, 2016; Trulsvik et al., 2011).

Dumais et al. (2020) used a minimum curvature algorithm (Briggs, 1974) to compile the various grids. Anomalies were computed using the relevant Definite Geomagnetic Reference Field (DGRF). The grid was upward continued to 1000 meter and consists of square cells of 2 by 2 kilometer. The study area of the current research coincides with the SPA-88 survey as shown in Figure 4.1a. Based on the 4-kilometer spacing of the survey, it is expected to be able to resolve anomalies of 10 km and greater (Skilbrei, 1992).

Gravity

Information about regional gravitational anomalies was retrieved from the Gravity Anomaly Map of NGU (Olesen et al., 2010), see Figure 4.2b. This map is based on both land data from the Norwegian Mapping authority and ship profiles from various sources, see Figure 4.1b. In areas with no data coverage, additional data was extracted from radar altimetry (Andersen & Knudsen, 2009).

Table 4.1: Overview of the aeromagnetic surveys used for the compilation of the magnetic anomaly map, updated after Dallmann (2015). Surveys shown which were relevant to the scope of the current study.

Area	Year	Operator, source	Survey name	Line spacing [km]	Sensor elevation [m]	Length [km]
NW Barents Sea	1987	NGU, Skilbrei (1991)	BSA-87	4-8	250	34000
Spitsbergen	1988	NGU, Skilbrei (1992)	SPA-88	4	1550	13300
Nordaustlandet	1989	Sevmorgeo 1989	SEV-89	2-8	N/A	N/A
Svalbard	1991	Amarok/TGS, Breivik & Faleide (2004)	SVA-91	7.5	900	27800
Fram Strait (KRAS)	2016-2018	NGU, Dumais et al. (2020)	KRAS	5.5	120	56906

As described in Dallmann (2015), the International Gravity Standardization Net 1971 (IGSN 71) (Morelli et al., 1972) and the Gravity Formula of 1980 (Moritz, 1980) were used for integrating the datasets. The data were interpolated to a grid with cell sizes of 2 by 2 kilometer using the minimum curvature method (Briggs, 1974) with an upward continuation to 500 meters (Jacobsen, 1987). The map shows the values of the Bouguer anomalies on land and the free-air anomalies at sea. An isostatic correction assuming a uniform Moho depth was applied based on the AIRYROOT algorithm (Simpson et al., 1983). More details about the data processing for this grid can be found in Dallmann (2015).

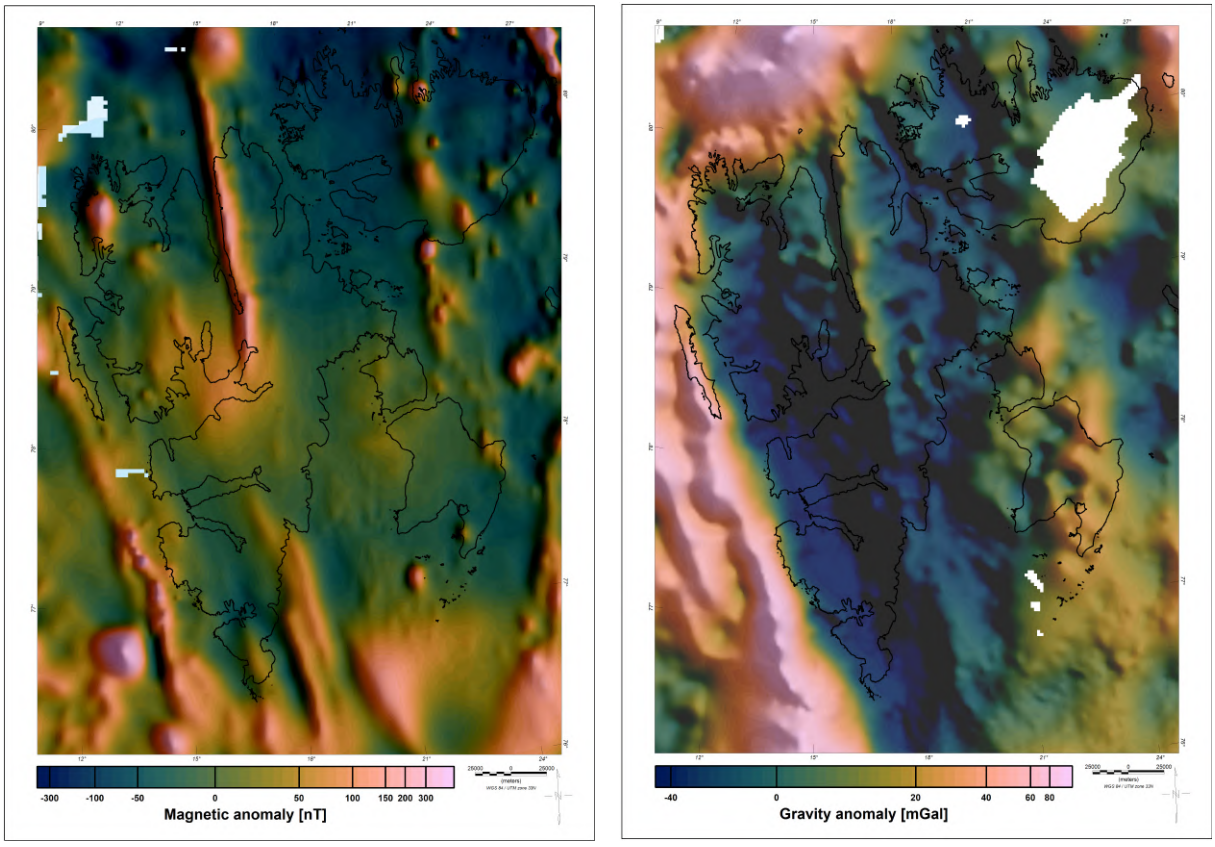

(a) Magnetic anomalies

(b) Regional map of the gravity anomalies

Figure 4.2: Magnetic (a) and gravity (b) anomalies of the region. Figures plotted using the color map of Crameri (2018). Appendix C contains identical maps created using the equal area rainbow color map.

4.1.2 Regional data application

In the current research, we used the data obtained from both the magnetic and the gravity potential field grid to study the regional trends in potential field anomalies. By integrating several geological data sources and overlaying the anomalies with geological maps, a first order understanding of the sources for the anomalies was obtained. This was enhanced by applying various filters to the data using the Oasis Montaj software (Geosoft, 2010). A low-pass filter was applied to the magnetic data to obtain insight into the long wavelength signal of the anomalies. The tilted derivative, a mathematical function indicating the outline of the potential sources (see Section 3.3), was determined. Due to some uncertainties coinciding

with the method, these positive tilted derivative areas will be defined as potential sources in the current study rather than considering them to be the hard outline of actual sources. Subsequently, an estimate of the source depth, tilt depth, could be extracted. Combining the edge detection of the tilted derivatives of both potential fields allowed some insight into the correlation between regions with potential gravity and magnetic sources and their geological implication.

We then combined knowledge about the regional trends with data on seismicity in Storfjorden to investigate a potential link. Earthquake data with a minimum magnitude of 2.7 for the time period of 1980-2012 (Dallmann, 2015) and a minimum magnitude of 4 for the time period of 2013-2023 (U.S. Geological Survey, 2023) were used. Fault zones can function as pathways for igneous intrusions, leading to potential field anomalies (Grogan et al., 2000). We investigated the link between the seismic activity and the anomalies to analyze whether one fault zone might be responsible for both.

Next to studying large-scale trends, the regional data functioned as a benchmark for a first-order quality control of the SvalGrav and SvalMag field data acquired in 2022. The regional gravity and magnetic grids were also utilized as some of the input data of the forward modelling. As the quality of the SvalMag data were found to be unsatisfactory, magnetic data along the profiles were extracted from the regional magnetic grid. Along profiles where no SvalGrav data were available, the gravitational values were extracted from this regional grid. Observations from the regional analysis were also used to aid the forward modelling.

4.2 Field survey

4.2.1 2022 field campaign

To expand on the regional potential field data with higher resolution gravity and magnetic data, the SvalGrav field campaign was executed between the 21st of April 2022 and the 1st of May 2022. It was led by The University Centre in Svalbard (UNIS) with critical contributions from the Norwegian Geological Survey (NGU), University of Tromsø (UiT) and the KTH Institute of Technology in Stockholm (KTH). Due to the smaller station spacing, these local data were more sensitive to short wavelength signals and therefore allowed a higher-order interpretation of subsurface features.

The areas of interest for data acquisition were determined by considering the anomalies identified in the regional potential field grids as well as regions of geological relevance. Due to logistical limitations, the fieldwork area was limited to regions where it was possible to travel by snow scooter within the direct surroundings of Longyearbyen. Gravity data were collected along 7 profiles in Nordenskiöld Land (see Figure 4.3), designed partly based on the coverage of previously acquired seismic data. Along some of the profiles, magnetic data were collected and along one profile Ground-Penetrating Radar (GPR) data were obtained. The profiles cover the CSB, as well as the BFZ and LFZ. A more extensive overview of the acquisition design from the field campaign can be found in Rylander & Sterley (2022).

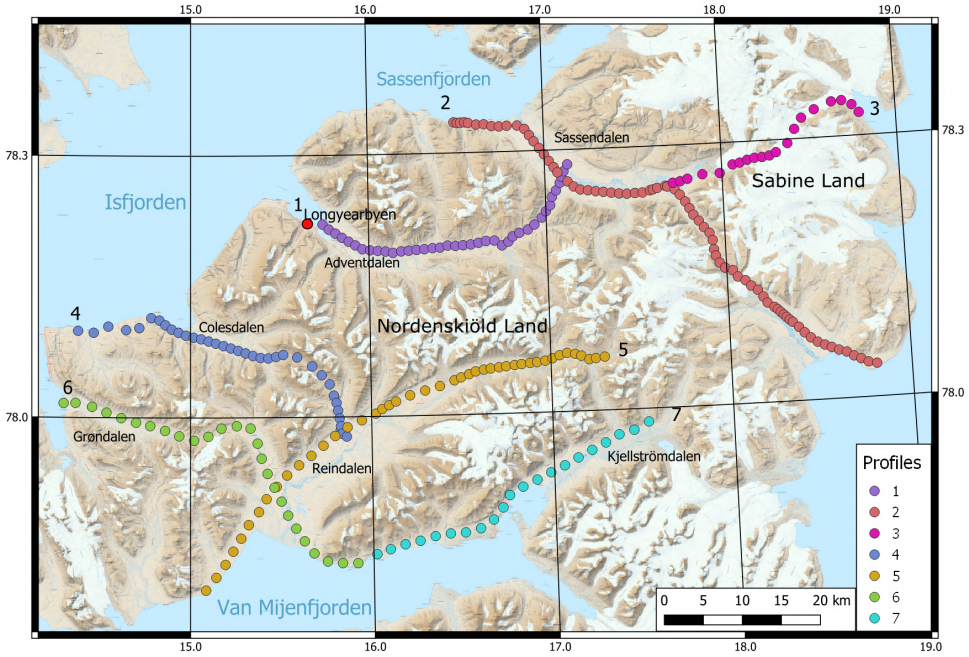

Figure 4.3: The location of the seven profiles collected in the SvalGrav field campaign. Most data were collected in Nordenskiöldland and Longyearbyen was the 'base camp' for this field campaign.

SvalMag: Magnetic survey 22

Unfortunately, there were several complications with the pilot acquisition of the magnetic data. A malfunction of the GPS of the magnetometer resulted in most data points missing location and time stamps. It was possible to obtain a rough location estimate by correlating the measurements to the GPX track of one of the scooters from the field campaign. This is a manual task which is time-intensive and introduces a lot of uncertainty into the data. Additionally, this scooter was primarily involved in the gravity data collection and its track is therefore less representative for the magnetic data. The configuration of the instrument was also altered throughout the fieldwork. This led to a change of about an order of magnitude in the measured values between different field days on the same profile. Consequently, we have used already available regional aeromagnetic data described above during the forward modeling.

SvalGrav: Gravity survey 22

Figure 4.3 shows the SvalGrav gravity data which were collected along 7 profiles. An overview of the rough location of the profiles with their corresponding parameters and seismic lines can be found in Table 4.2. In total 260 field data points were collected and the profiles had a cumulative length of 330.6 km. The pre-determined station spacing was one kilometer. However, during the acquisition station spacing was adapted to 500 meters in regions of high geological interest near fault zones. Large station spacing up to 2000 meter was used in regions of low geological interest.

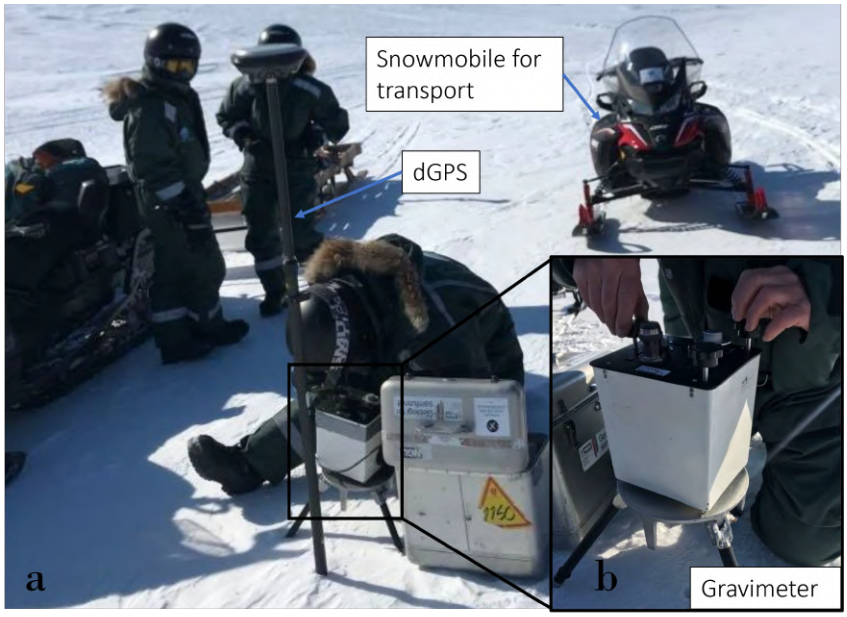

Figure 4.4: Figure illustrating the acquisition of gravity data in the field during the 2022 survey. a) The closest instrument is a Leica Viva GS16 dGPS used for accurate positioning in the field. The LaCoste & Romberg gravimeter is placed on a tripod behind it. b) The tripod is used to bring the gravimeter to a completely horizontal level, after which the relative gravity value could be determined. Figure adapted from Rylander & Sterley (2022).

The field setup for measuring the gravity is shown in Figure 4.4. Accurate positioning in the field was done using a Leica Viva GS16 dGPS, elevation measurements were especially relevant in further gravity processing steps. Gravity measurements in the field were done using a LaCoste & Romberg G569 model. As illustrated in Figure 4.4b, the gravimeter was placed on a tripod to bring it to a completely horizontal level. Once in balance, the spring was readjusted to determine the new relative gravity level. The relative values could be calibrated based on absolute gravity values from a base station located in Longyearbyen in the building of Sysselmesteren (78.223 N, 15.627 E). At the start and end of every field day, an additional measurement was taken at UNIS to correct the values for any instrument drifting.

The processing of the gravity data was done at NGU by Jomar Gellein. The latitude correction was based on Moritz (1980) and a density of 2670 kg/m^3 was used for the Bouguer and terrain corrections. The resulting Bouguer anomalies can be found in Figure 4.5. A terrain correction was also computed. However, it showed irregularities along the profiles which had no direct explanation by the local topography, see Figure 4.6. This is most likely due to the limited resolution of the DEM used for the computation of the terrain correction.

Gravity processing on Svalbard is challenging due to the presence of thick snow layers and glaciers which are responsible for some of the topography. In general, Bouguer corrections assume a density of 2670 kg/m^3, which is about 3 times as high as 850 ± 60 kg/m^3, which was found to be the density of glaciers appropriate for most conditions (Huss, 2013). Any elevation due to glaciers rather than bedrock should be compensated for to get representative Bouguer anomalies.

During the SvalGrav survey, the glacier thickness along Profile 3 was determined using a GPR. The bedrock layer below the glacier was identified by looking at conductivity contrasts resulting from radio waves. As Profile 3 was not selected for further forward modeling in the current research, this data set was not utilized but might be useful in future studies. Additionally, a recent DEM of the glacier thickness and ice-free topography of Svalbard (Fürst et al., 2018) would be essential input for accurate processing of all gravity data.

Table 4.2: Overview of the profiles of the 2022 SvalGrav field campaign with a rough location, the length of the profile, the amount of gravity data points, the mean distance between these data points, the range of distances between the data points and coinciding seismic lines for every profile. The range indicates the distribution of values between the 10th and the 90th percentile, to exclude anomalous values.

Profile	Location	Length [km]	Data points	Mean distance [m]	Range [m]	Seismic lines (E-W)
1	Adventdalen	38.20	39	1005	935-1098	**NH8802**-03,-02,-01,-08
2	Sassendalen	67.97	74	931	512-1086	**NH8802**-14,-13,-12
3	Sabine Land	28.00	20	1474	956-2060	**NH8802**-31
4	Colesdalen	43.65	36	1247	971-2009	**NH9108**-02
5	Reindalen	62.95	44	1464	905-2030	**NH9108**-07, **NH8802**-32
6	Grøndalen	49.15	26	1966	1877-2061	**NH9108**-06,-05
7	Van Mijenfjorden / Kjellströmdalen	39.70	21	1985	1930-2024	**SVA-VM-85**-01, **UNIS-AG351**-3,-2 **NH8903**-21

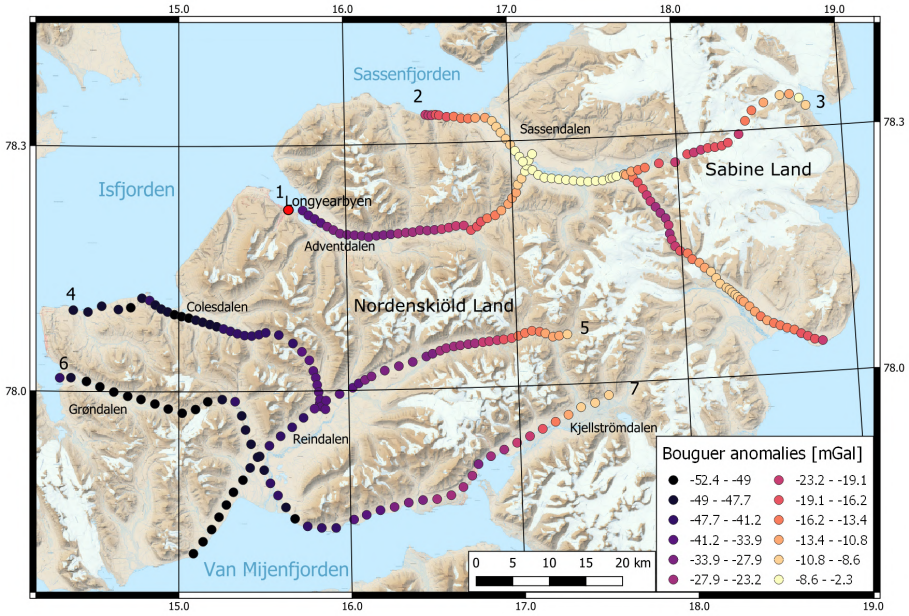

Figure 4.5: Computed Bouguer anomalies of the SvalGrav survey without terrain correction. Number indicates the SvalGrav profile, more information can be found in Table 4.2.

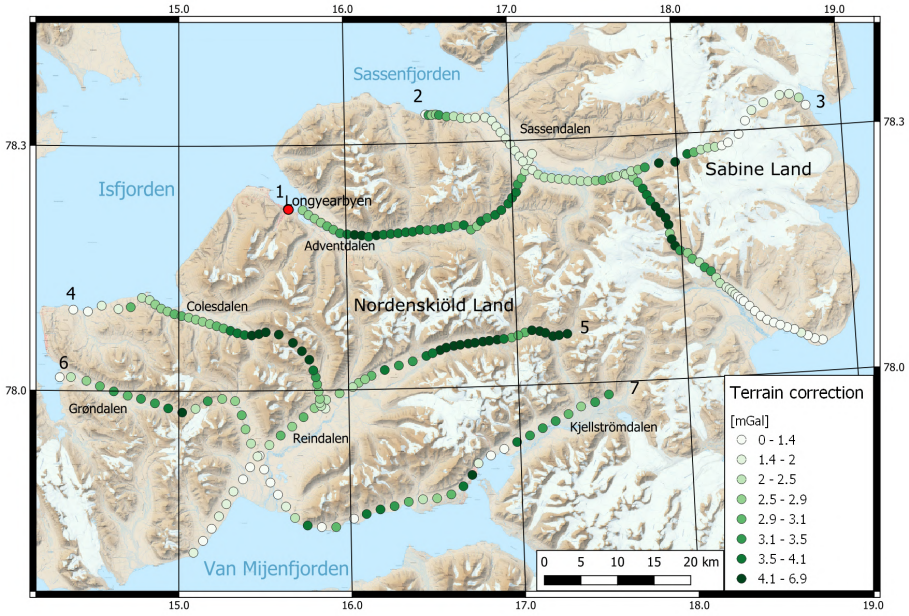

Figure 4.6: The computed terrain correction of the SvalGrav survey for the various stations. Numbers indicate the profiles of which more information can be found in Table 4.2.

4.2.2 Field data application

Our original aim was to include both the SvalGrav and SvalMag data as input observations for the forward modeling. Before doing so, we evaluated the quality of the newly acquired data and analyzed the applied processing steps. Due to the numerous limitations and uncertainties of the SvalMag data, it was decided these data were not applicable for forward modeling. The regional aeromagnetic data were used instead.

We evaluated the SvalGrav data by quantitatively comparing the new data to values sampled from the regional gravity grid at the same location as the SvalGrav stations. The Mean Absolute Error (MAE) was computed as an indicator the accuracy of the new data (Willmott & Matsuura, 2005). This was combined with the correlation coefficient which describes how well the trends of the two data sets match (Schober et al., 2018). This quantitative comparison was done for all data combined as well as for the individual profiles. We then investigated misfits between the two data sets to see whether these were originating from some of the data processing steps. If this was not the case, the misfits were most likely caused by the increased data resolution which allowed smaller anomalies to become visible. Specific focus was on the accuracy and suitability of applying the terrain correction for the data used in the forward modeling. As the quality of the SvalGrav data was found to be satisfactory and as it has a higher resolution, these data were used as input for the forward modeling where available.

Table 4.3: Overview of all the geophysical data used. Numbers link to Figure 4.7 showing the workflow. *More information on the boreholes can be found in Table 4.4. Abbreviations: AWI = Alfred Wegener Institute, HU = Hokkaido University, KTH = KTH Institute of Technology in Stockholm, NGU = Geological Survey of Norway, NH = Norsk Hydro, NMA = Norwegian Mapping Authority, NOPEC = Norwegian Petroleum Exploration Consultants, ST=Statoil, UiB = University of Bergen, UNIS = University Centre in Svalbard.

No.	Data type	Physical parameter [unit]	Location	Year	Operator	Source	Survey name	Survey type	Comments	Application
1	Magnetic	Susceptibility [SI]	Onshore and offshore Svalbard	1969-1991	NGU	Olesen et al. (2010)	NGU-69, BSA-87, SPA-88, SEV-89, SVA-91	Airborne	4-10 km line spacing.	Regional magnetic trends.
2	Gravity	Gravitational acceleration [mGal]	Onshore and offshore Svalbard	-	NMA and various others	Olesen et al. (2010)	-	Land and marine	2 x 2 km grid. Isostatically corrected Bouguer anomalies.	Regional gravity trends.
3	Magnetic	Susceptibility [SI]	Profiles 1,2,3,4,7	2022	UNIS & KTH	UNIS database	SvalMag	Land	Rough spacing of 12.5 m. Instrumental complications	-
4	Gravity	Gravitational acceleration [mGal]	Profiles 1-7	2022	UNIS & KTH	UNIS database	SvalGrav	Land	1.3 km average station spacing.	Local gravity variations.
5	GPR	Radio waves	Profile 3	2022	UNIS & KTH	UNIS database	-	Land	-	Determining glacier thickness.
6	Borehole*	Density, velocity and susceptibility	Onshore Svalbard	1966-1991	Various	UNIS database	-	-	See Table 4.4 for more details.	Constraining model parameters.
7	Seismic reflection	Acoustic impedance	Along SvalGrav profiles	1985-1991	NH	UNIS database	NH8802, NH8903, NH9108	Land	60 channel 1500 m snow streamer. See Table 4.2.	Seismic interpretation.
8	Seismic reflection	Acoustic impedance	Offshore	1985-1988	NOPEC, NH, ST	UNIS database	SVA-VM-85, NH8706, ST8815	Marine	-	Seismic interpretation.
9	Seismic reflection	Acoustic impedance	Svea	2017	UNIS, UiB	UiB database	AG-335/2017	Sea ice	Detonating cord, 25m geophones.	Seismic interpretation
10	Seismic refraction	Acoustic waves	Offshore	1997-1999	AWI, UiB, HU	Ritzmann et al. (2002, 2004)	AWI-97260, OBS98, AWI-99400	Marine	Airgun.	Velocity profile.

Table 4.4: Overview of the boreholes used in this research with the specific data accessed. Information retrieved from Olaussen et al. (2023). Abbreviations for operating companies: Amoseas = American Overseas Petroleum, NH = Norsk Hydro ASA, NPN = Norsk Polar Navigasjon AS, SNSK = Store Norske Spitsbergen Kulkompani AS, TA = Trust Arktikugol, T-PG = Polargas Prospektering. *Vassdalen well data from Bro (1990a,b).

No.	NPD well ID Borehole name	Easting Northing Longitude Latitude	Operating company Completed	Elevation KB (m) Total depth (m MD)	Youngest age Youngest formation	Oldest age Oldest formation	P -wave velocity Density	Susceptibility Relevant profile	Usage in this research
1	7715/3-1	522340 8640201	Amoseas	18	Paleocene	Early Permian	X		Velocity constraints for profile 7.
	Ishøgda I	15°58'00" 77°50'22"	3/15/1966	3304	Grumantbyen Fm	Gipshuken Fm		7	
2	7816/12-1	544775 8665611	NH/SNSK	182.5	Early Cretaceous	Middle Carboniferous	X		Velocity and density constraints for profile 5.
	Reindalspasset I	16°56'31" 78°03'28"	4/11/1991	2315	Carolinefjellet Fm	Hultberget Fm	X	5	
3	7715/1-1	503990 8639407	TA	15.13	Eocene	Carboniferous (?)		X	Density and susceptibility constraints for profile 5.
	Vassdalen II*	15°11'15" 77°49'57"	7/14/1987	2481	Frysjaodden Fm	Billefjorden Gp (?)	X	5	
4	7715/1-2	503990 8639407	TA	15.13	Eocene	Middle Triassic		X	Density and susceptibility constraints for profile 5.
	Vassdalen III*	15°11'15" 77°49'57"	9/1/1989	2352	Frysjaodden Fm	Botneheia Fm	X	5	
5	7617/1-2	552650 8533700	T-PG	6.7	Early Cretaceous	Early Permian	X		Constraints for general velocity and density relationship.
	Tromsøbreen II	17°05'38" 76°52'31"	8/24/1988	2337	Carolinefjellet Fm	Gipshuken Fm	X	-	
6	7811/5-1	422845 8741814	NPN	5	Oligocene	Pre-Devonian	X		Constraints for general velocity and density relationship.
	Sarstangen	11°28'40" 78°43'36"	12/1/1974	1113	Sarstangen conglomerate	Hecla Hoek	X	-	

4.3 Forward modeling and data integration

We constructed 2D forward models of gravity and magnetic data along five key profiles with the GM-SYS software package (Geosoft, 2006). These profiles were selected based on their intersection with the BFZ as well as the quality and quantity of the available supplementary data. Forward modeling was started on Profile RN (Regional North) and Profile RS (Regional South), located in Isfjorden and Van Mijenfjorden, respectively. No SvalGrav data was available along these profiles, so they are based on the input of regional data for both the magnetic and gravity observations. Along the profiles high resolution seismic data were available with previously established seismic interpretation in literature (Bælum & Braathen, 2012; Faleide et al., 2015). Additionally, these offshore lines were not influenced by any terrain effect reducing the presence of potential processing errors, making modeling and interpretation less ambiguous. Due to the respective location of Profile RN and RS north and south of the SvalGrav acquisition area, interpolation of key geological observations on the other three profiles was possible. These profiles were Profile 2, Profile 5, and Profile 7, based on the SvalGrav profiles in Nordenskiöldland. They are in Sassendalen, Reindalen and Kjellströmdalen, respectively. Profile 5 was the best constrained by two boreholes and seismic data were available along the whole line. Modeling started on the profiles with the best constraints but were simultaneously finalized for the sake of consistency between the models.

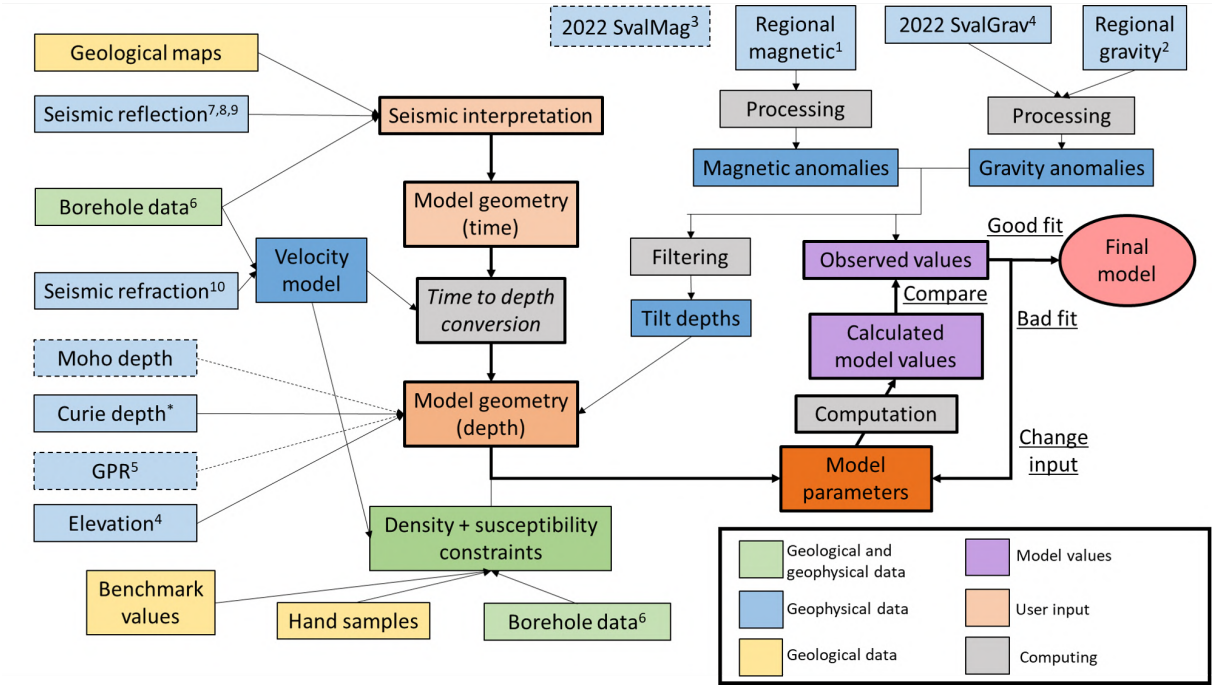

Figure 4.7: Overview of the different elements which went into the data integration used to constrain the forward models. The main elements of the data integration are shown in the figure, smaller elements of which some information was extracted are mentioned in the text but were left out to keep the figure concise. Dashed boxes indicate data which were relevant for the scope of the study but were not used in the forward modeling of the 5 profiles. The numbers in the geophysical data boxes refer to the data source found in Table 4.3, * are values extracted from a grid based on computations on geophysical data. Darker shades of the same color indicate a processing or filtering step was executed before. Illustrated is the iterative process of reworking the model until a good fit with the observed values is found.

Table 4.5: An overview of the five forward models with their respective geophysical data sources. I = Ishøgda, R = Reindalspasset and V = Vassdalen.

Profile	Regional magnetics	Regional gravity	SvalGrav	Borehole	Seismic data (E-W)
2	x		x		**NH8802**-14, -13, -12
5	x		x	V, R	**NH9108**-07, **NH8802**-32
7	x		x	I	**SVA-VM-85**-01, **AG351**-3,-2, **NH8903**-21
RS	x	x		I	**SVA-VM-85**-01
RN	x	x			**ST8815**-114,-222,-125, **NH8706**-405

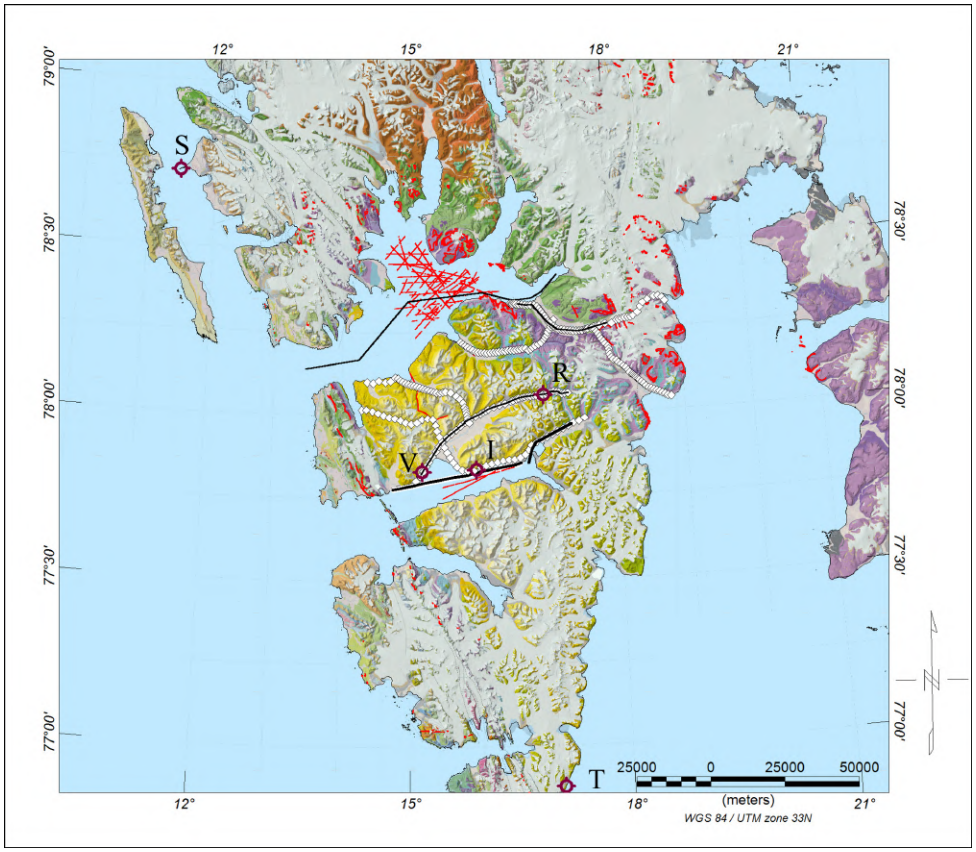

Figure 4.8: Overview of data plotted on the geological map of Dallmann (2015). White diamonds indicate the location of the SvalGrav survey, black lines the location of the seismic data, red are interpreted igneous sills on 2D seismic data and outcropping igneous rocks and the location of the five boreholes is plotted. I = Ishøgda, R = Reindalspasset, S = Sarstangen, T = Tromsøbreen, V = Vassdalen

For constraining the parameters and limiting the ambiguity of the forward models, we integrated data of various geological and geophysical sources. An overview of the different elements which went into the workflow of the forward modeling can be found in Figure 4.7 and their location in Figure 4.8. The geophysical data elements are linked to Table 4.3, where additional information can be found. Here follows a short workflow of the forward modeling, which will be expanded upon in the rest of the section.

The first step to create the model was to establish the geometry in the time domain based on seismic interpretation. A velocity model was then used to convert the geometry into the depth domain. Additional depth horizons such as the topography and mantle depth were included, after which density and susceptibility parameters were assigned to the various units. The resulting gravity and magnetic output were then computed and compared to the observations. Through an iterative process of manually adapting the assigned parameters, multiple scenarios could be tested to find the model with the best resulting fit. These models could then be used to expand on their geological implications.

Model projection

It should be noted that as the models are two-dimensional, they are represented by a straight line. In contrast, most of the gravity profiles were following the terrain and are curved. The location of the model line was automatically determined by ensuring a minimum distance to all the data points. As a result, the data points locations rarely match with the location of the model. This meant that it was necessary to perpendicularly project the data points back onto this straight line, as illustrated in Figure 4.9. This led to an uneven spreading of the data points along the model and the resulting distortion made incorporating seismic interpretations as a reference more challenging. All data used as modeling input were extracted along the data profile and projected accordingly on the straight model line.

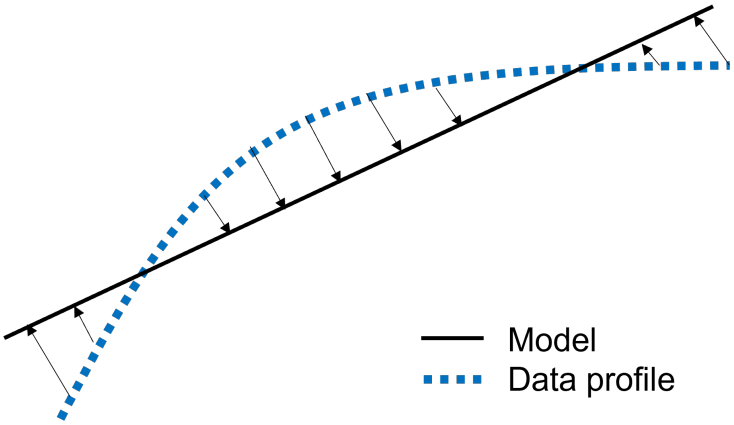

Figure 4.9: A simple illustration showing the concept of projection. The 2D forward model is a straight line at a mean minimum distance to the data points. Due to the curvature of the data profile, it is necessary to perpendicularly project data values to the model line as indicated with the arrows.

4.3.1 Step 1: Geometry in time domain

The first step to creating the model was to establish the preliminary geometry of the model in the time domain. By combining data from boreholes and geological maps, we made seismic interpretations based on seismic reflection data using PETREL software (Schlumberger, 2022), see Figure 4.7.

An overview of the seismic reflection data can be found in Table 4.3 and an overview of the seismic lines coinciding with the SvalGrav profiles in Table 4.2. This is mostly land data acquired with a snowstreamer between 1985-1991 by Norsk Hydro (NH) and Norwegian Petroleum Exploration Consultants (NOPEC). Additional seismic lines were also available in the UNIS database which enhanced the interpretation of seismic features. Within the scope of the AG-351/851 Arctic Seismic Exploration course at UNIS in cooperation with University of Bergen (UiB), new seismic data were collected on sea ice at Svea in Van Mijenfjorden in 2017 (Johansen et al., 2019). This segment connects the NH8510-203 marine line with the NH8903-21 onshore line.

General information about the geology of Svalbard was extracted from Dallmann (2015) and the geological map of the Norwegian Polar Institute (NPI). A seismic interpretation of Profile RN from Bælum & Braathen (2012) was used as a benchmark for the interpretation on this profile. Concept subsurface models in two-way traveltime of Faleide et al. (2015) were used for the Profile RN, Profile RS and Profile 7. Interpolation of the identified horizons from these cross sections allowed a first-order estimate of the depth of different stratigraphic groups on other seismic lines. This interpretation was fine-tuned based on the seismic reflectors and well ties where available. The Vassdalen, Reindalspasset and Ishøgda boreholes were used for adding stratigraphic constraints.

We interpreted the seismic lines based on the main stratigraphic horizons and faults, focusing on the major regional high angle fault zones as they were expected to have a significant influence on the potential field data. Low angle decollements and associated thrust faults were omitted as they would add further complexity to the models while a negligible gravitational and magnetic effect is expected. The defined horizons were exported and imported into GM-SYS to use as basis for the model. It was not possible to import faults, so these were manually added after the importing the horizons. Both outer edges of the model extend into infinity to prevent edge effects on the computed values.

4.3.2 Step 2: Time-to-depth conversion

After establishing the model geometry in the time domain, the next step was to convert it to the depth domain by assigning velocity values to the model. Insight into the expected velocity model of the subsurface was obtained from borehole data and seismic refraction studies.

Constraints about the seismic P-wave velocity for the different stratigraphic units were obtained from compilations in literature (Bælum & Braathen, 2012; Marello et al., 2013). These were based on various sources, such as the seismic refraction studies of Breivik et al. (2002, 2005); Ljones et al. (2004); Ritzmann et al. (2002, 2004). Additionally, seismic velocity data from the Ishøgda, Reindalspasset and Tromsøbreen borehole logs were used as a reference for the expected velocity in the upper few kilometers. An overview of the seismic velocities for the different stratigraphic groups can be found in Table 4.6. For more details on the boreholes the reader is referred to Table 4.4. Velocity profiles were created for the

different boreholes. These velocities were used to convert the time model into a depth model, as seen in Figure 4.7. It should be noted that it was not possible to incorporate a depth dependent velocity profile into the model. Instead, the velocities were assigned manually to the geometry blocks which results in depth-conversion limitations coming from this simplified approach. As the depth horizons of the lower crust and mantle transition were not incorporated in the time domain and added after conversion as a separate depth horizon, consistent velocities were applied.

Table 4.6: Seismic velocity [m/s] constraints for the different stratigraphic groups based on literature compilations and average velocities from borehole data.

Group	Bælum & Braathen (2012)	Ishøgda	Reindalspasset	Tromsøbreen
Van Mijenfjorden Gr.	4300-4500	4436		
Adventdalen Gr.	3800-4300 / 3500-4200	4006	3941	3626
Kapp Toscana Gr.	4000-4500	4906	4039	4736
Sassendalen Gr.	3500-4000	4719	4267	4868
Tempelfjorden Gr.	>5000	5315	5436	
Gipsdalen Gr.	>6000	5820	6127	5622
Billefjorden Gr.	4000-6000		5095	
Old Red	>6000			
Basement	>6000			
Intrusions	>6000			

4.3.3 Step 3: Adding depth horizons

Once we obtained a model in the depth domain by assigning the suitable velocities, the next step was to add further depth horizon constraints. The topography of the profiles was included based on elevation data collected during the SvalGrav survey. The Curie depth grid in the current research was retrieved from Dumais et al. (2022), who used the Pycurious python code (Mather & Delhaye, 2019) based on the algorithm of Bouligand et al. (2009) for computing the depth. The Curie depth was sampled along the profiles and used in the forward modeling to determine the maximum depth to which magnetic parameters were assigned. The depth of all created models is 50 kilometers, the transition to the mantle was uniformly set at 30 kilometers. It was decided not to alter the Moho depth between the models as there were no reliable data available to support introducing large fluctuations. From the tilted derivative grids, it was possible to extract the tilt depth. This is the depth from which the anomaly source is expected to originate. While we did not include it as horizon in the forward model, it did help give a rough estimate of the expected source elevation. If we would have selected the glacier-crossing profile for forward modeling, it would have been necessary to incorporate the glacier thickness retrieved from GPR data at this step.

4.3.4 Step 4: Assigning parameters

Once the depth geometry was established, density and susceptibility constraints to the different polygons were assigned. In order of importance, information was used from borehole data, velocity models, hand samples and benchmark values retrieved from literature. Consistent density and susceptibility values for the stratigraphic groups were applied for all models.

Borehole data and velocity models

Profile 5 coincided with the wildcat boreholes Vassdalen II & III and Reindalspasset. For the Vassdalen boreholes, no continuous logs were available but point sampled data of both density and susceptibility values were accessible (Bro, 1990a,b). Density and seismic velocity information was available for the Reindalspasset borehole. All three boreholes had a measured depth (MD) of around 2400 meters. Profile 7 coincided with the Ishøgda borehole of which P-wave velocities were available. An overview of the stratigraphic coverage and petrophysical parameters can be found in Table 4.4. Density constraints from the different stratigraphic groups were obtained from the Tromsøbreen and Reindalspasset boreholes.

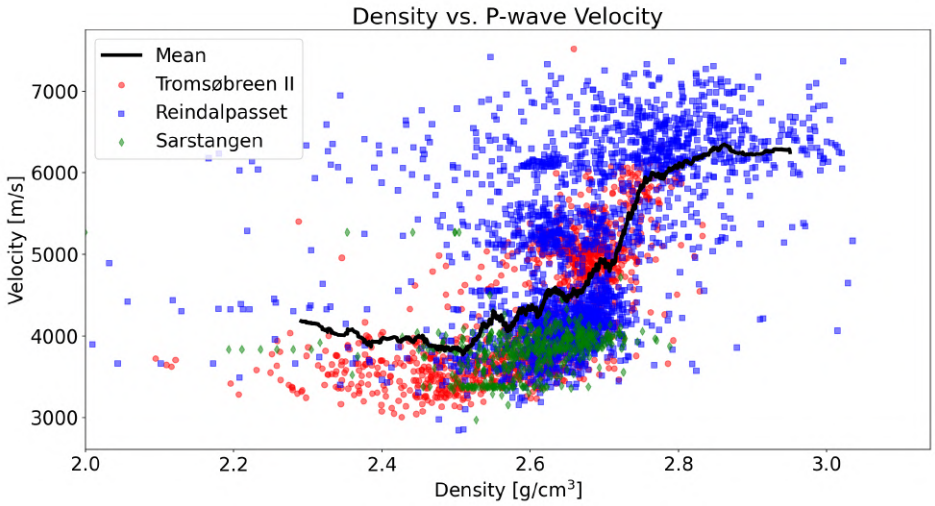

Figure 4.10: Velocity-density relationship based on data of 3 different boreholes.

Tromsøbreen, Sarstangen and Reindalspasset boreholes were used for investigating the general velocity-density relationship of the subsurface. As seen in Figure 4.10, the velocity values were plotted against the density values from which a rolling average was extracted. Due to the significant spread of the data points, further refinement by categorizing the data points based on their lithology or stratigraphic group would be required for more suitable velocity-density relationship estimations. However, this was not feasible within the scope of the current research and a first-order estimate was retrieved. A table with an overview of P-wave velocities with the corresponding density value based on the three boreholes is visible in Appendix A. As the borehole data only cover the upper two kilometers, extrapolating the relationship to deeper depths was done taking potential inaccuracies into consideration. The velocity-density relationship was used to convert the velocity model to expected density values in regions where only velocity information was available. This was combined with previous estimations of density models from literature (Ritzmann et al., 2002, 2004; Marello et al., 2013), where in some studies they adapted their models to match gravity observations.

Hand samples

Information about the density and susceptibility of rocks on Svalbard was available in some studies analyzing hand samples. Amphibolite samples from the western Ny-Friesland terrane were found to be relatively high in regards of the magnetic susceptibility with an average value of 0.01600 SI (Kurinin, 1965). Further east in the Nordaustlandet terrane, granite samples were found to be relatively non-magnetic (Hjelle, 1966). Krasil'ščikov et al. (1995) studied samples from 6 different rock types in the eastern part of the Forlandsundet graben. Mesozoic dolerites and serpentinites had the highest magnetic susceptibility, ranging from 40-1000 10^{-6} SI, with a density range of 2950-3100 kg/m^3 and 2500-2700 kg/m^3 respectively. There were widespread density and susceptibility values for the sampled metabasic rocks. The phyllites, carbonates and siliciclastic rocks were all found to be non-magnetic ($\leq 10 \cdot 10^{-6}$ SI with an average density of around 2700 kg/m^3. Sedimentary rocks of the Tempelfjorden and Gipshuken group were found to have an average density of 2500-2700 kg/m^3 (Jafarian et al., 2017).

As limited studies have been performed on Svalbard analyzing the density and susceptibility of the rocks, general susceptibility and density values of rocks as previously described in the literature were used in places of knowledge gaps. Telford et al. (1990) was used as a reference to constrain chosen density and susceptibility values elected for the model.

Intrusions

The location and depth of intrusions identified in Senger & Galland (2022) were incorporated in the forward models. The HALIP has a significant presence on Svalbard and around the study region. Based on borehole, seismic and magnetic data of the region, an area of 3000 km^2 was inferred in Central Spitsbergen. An additional 7.2 km^2 is outcropping and an average magma volume of 51.84 km^3 is estimated (Senger & Galland, 2022). Intrusions were added to Profile RN where the magnetic and seismic data suggested their presence. Suitable susceptibility values were assigned to these larger magmatic bodies to fit the data.

4.3.5 Step 5: Iteration and computation

Once the model parameters, the geometry and density and susceptibility constraints, were established, the resulting gravitational and magnetic signal was computed by the software. For the magnetic modeling the divergence theorem was used (Blakely, 1995). The effect of the individual model polygons was summed based on a method adapted from Talwani et al. (1959).

A comparison was made between the computed and the observed values, both in terms of trends and a quantitative error measure between the two profiles. The initial model was then adapted through an iterative process of adjusting the density, susceptibility, and geometry input to minimize the error within the constraints of the integrated data, as indicated in Figure 4.7. This iterative process was also useful for testing multiple scenarios to find the best fit to the data, especially when it was challenging to explain the observations based on the integrated data. The model with the best fit was then determined to be the final model.

Finally, during initial modeling the Direct Current (DC) shift was set to automatic, which meant the calculated values were adjusted to be within the range of the observed values by applying a correction to all the data points. The DC shift is an offset between the potential field data which could have been caused by for example drifting of the instrument, incorrect or incomplete data. Once the fit between the model and the observations was satisfactory, the absolute DC shift value for both the magnetic and the gravity data was determined separately. These values were then compared between the different profiles and were expected to be in a similar range.

4.3.6 Step 6: Geological implications

Once the forward modeling was completed, it was important to broaden the scope of the research again. The obtained interpretations and observations from the best fitting models were used to further understand the regional anomalies. Figures with a consistent vertical scale between the models were produced, which allowed relatively easy comparison. Additional observations about geological features were also compared to previous findings in the literature, with where necessary newly proposed scenarios or hypotheses were offered.

5 Results

In this section we present the results from the regional potential field studies. We then focus on the quality control of the acquired SvalGrav data and present the final seismic interpretations and forward models for the five key profiles.

5.1 Regional trends

Magnetic regional trends

The result of applying a low-pass filter on the regional magnetic grid (Figure 5.1a) around the study area is shown in Figure 5.1b. Positive long wavelength anomalies are prominent in central Spitsbergen (A), along the BFZ (B), along the HFC (C) and in southwestern Storfjorden (D). For the current research, the Isfjorden and BFZ anomalies were of particular interest as they overlap the acquisition area of the SvalGrav survey. The two anomalies are separated in the north but overlap around Isfjorden. The magnitude peaks at 73 nT in central Isfjorden and reduces southwards, becoming negligible around Van Mijenfjorden. The southern edge of the anomaly again showed separation, with a thin eastern limb and a broader western one. Some secondary effects of filtering were visible, but these did not seem to impact the main anomalies.

Figure 5.1b also shows the location of the five forward models. The Isfjorden magnetic anomaly is imaged by the two northernmost profiles, Profile RN and Profile 2. The southward extent of the anomaly overlapped with Profile 5 located further south, but does not continue to the two southernmost profiles, Profile RS and Profile 7.

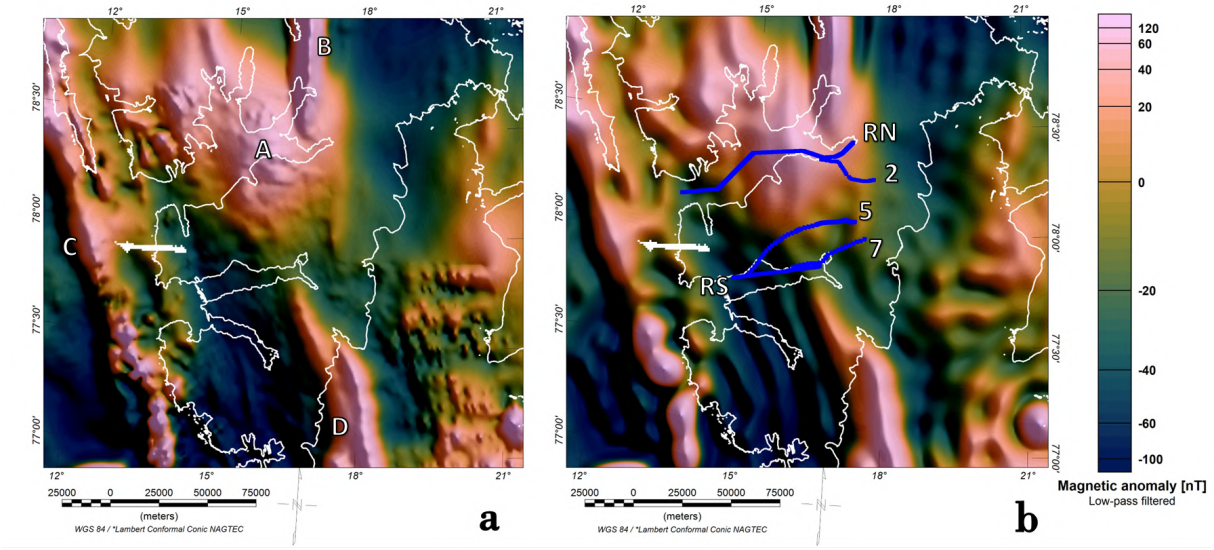

Figure 5.1: a) The magnetic anomalies before low-pass filtering. The letters indicate four positive anomalies in the regions. b) The magnetic anomalies after low-pass filtering magnetic grid accentuating the long wavelength signal. The data profiles of the five forward models are plotted as blue lines with their names annotated. Both figures have a shadow at an inclination and declination of 45 degrees to accentuate the anomalies and use color maps from Crameri (2018). Appendix C contains the low-pass figure with the equal area rainbow color map.

Figure 5.2a shows the tilted derivative of the Svalbard regional magnetic grid of Figure 4.2a. Areas with a positive tilted derivative are indicative of a potential source, with the edges outlined by a black zero-contour line. Similar to what Figure 5.1 showed, an elongated potential source with a NNW-SSE orientation is located along the BFZ and connects to a broader Isfjorden anomaly further south. The BFZ anomaly has a width of 10-15 kilometers and is about 200 kilometer in length. At its broadest, the elliptical Isfjorden anomaly is 60 kilometer wide. South of Profile RS, another elongated potential source area is visible which is shifted slightly more westwards and seems to be fragmented. Two more NW-SE trending potential anomalies are distinguished, one off the western coast and a less well-defined one crossing Nordaustlandet.

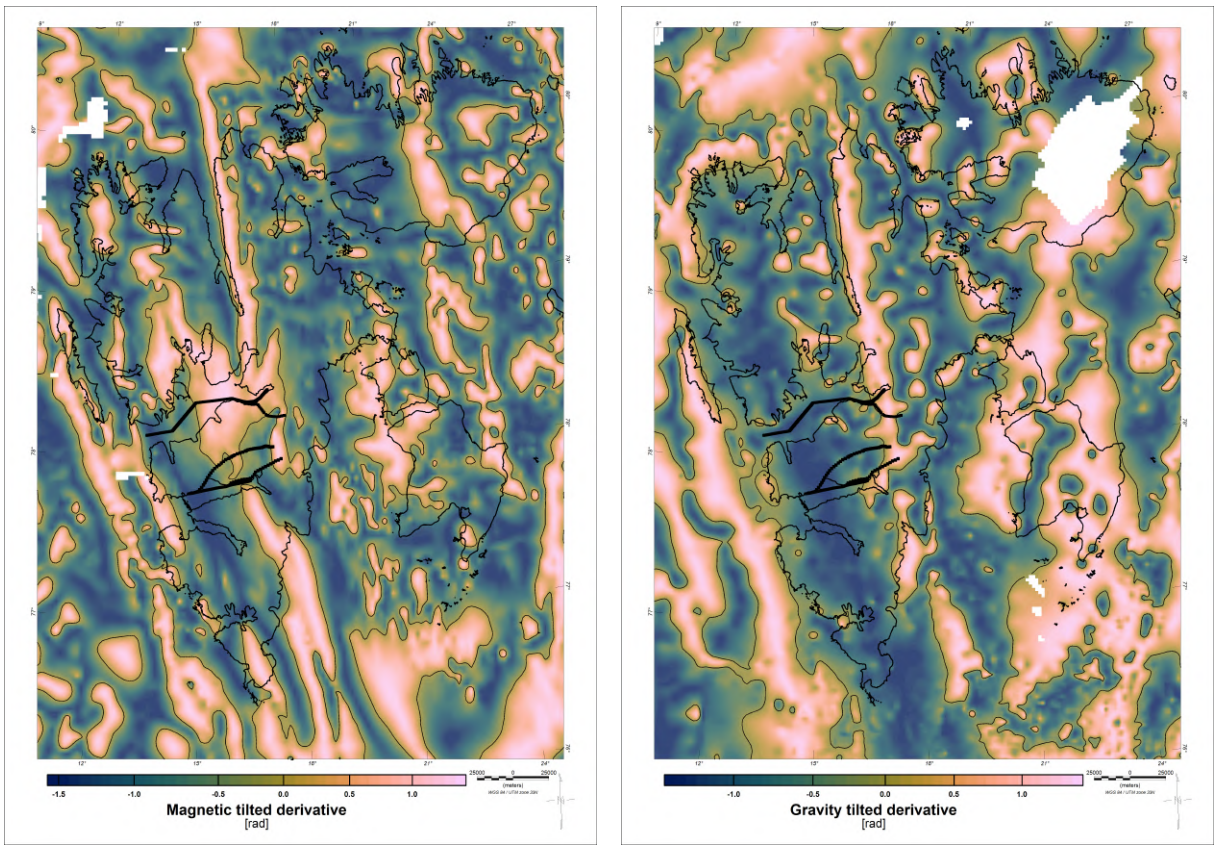

(a) Tilted derivative of the magnetic anomaly.

(b) Tilted derivative of the gravity anomaly.

Figure 5.2: Tilted derivatives of the magnetic (a) and gravity (b) data. A thin black line outlines the zero-contour of the tilted derivative, which is the edge of the potential source. This potential source is indicated by the area with a positive tilted derivative. Thick black lines show the data profiles of the five forward models. Crameri (2018) color map is used and an identical figure with rainbow color map can be found in Appendix C.

The computation of the tilt depth provided a rough estimate of the depth of the potential magnetic sources and was computed for a grid covering the whole of Svalbard (Figure 5.3) and a region focused around the study area with a denser point sampling (Figure 5.4). The tilt depth determination did not account for the elevation of the magnetic data. This introduced uncertainty into the absolute ranges of the anomaly depth, therefore the main takeaway was the relative depth position of the anomalies. The BFZ anomaly is relatively shallow with a depth of about 3000-4000 meters. The Isfjorden anomaly is in general deeper with the outer edge having a range of 4000-7000 meters with some internal shallower anomalies between 1500-3000 meters. Between Isfjorden and Van Mijenfjorden, it was apparent that the anomaly exists out of a deeper western leg and a shallower eastern leg with depths between 2000-3000 meters. This suggested that these two anomalies might not be related to the same system. Some more shallow sources were visible offshore illustrated in Figure 5.4 as patchy sources in the southeast with a depth range of 1500-3000 meters.

Gravity regional trends

The tilted derivative of the regional gravity grid (Figure 4.2b) can be seen in Figure 5.2b. The positive areas, indicative of a potential source, were primarily present as a large, elongated NNW-SSE trending feature along the BFZ. It has an average width between 15-20 kilometers and a length of 300 kilometers extending from the northernmost tip of Ny-Friesland to the east coast of Torell Land, with fragmentation further down in Storfjorden. A NW-SE orientated positive anomaly is visible of the western coast of Svalbard. Between these two highs, a large area with a negative tilted derivative was visible. No tilt depth data were acquired as this method required additional structural information for applying it to gravitational data.

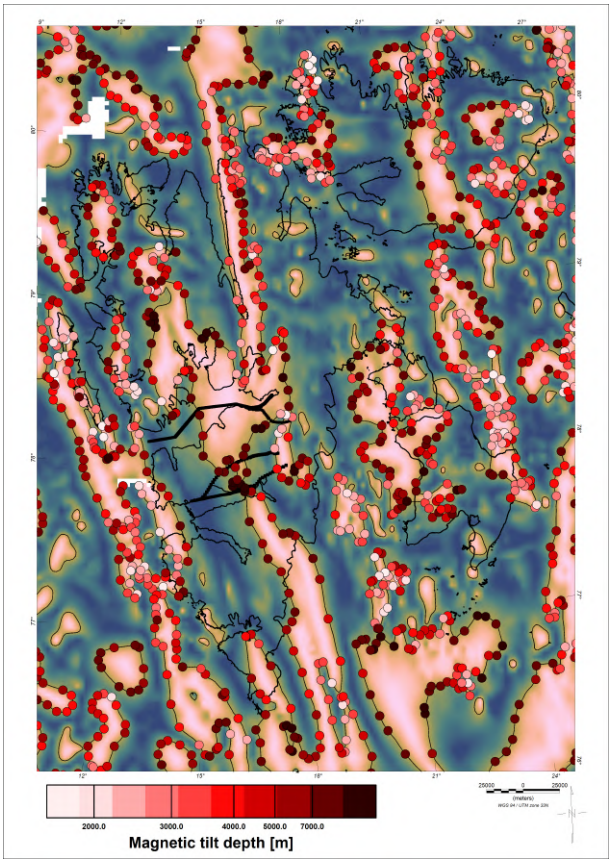

Figure 5.3: The computed tilt depth along the zero contour of the tilted derivative for the entire Svalbard region. The Isfjorden anomaly is deeper than the anomaly along the BFZ. A color legend of the tilted derivative can be found in Figure 5.2a. The thick black lines indicate the location of the five data profiles used for forward modeling.

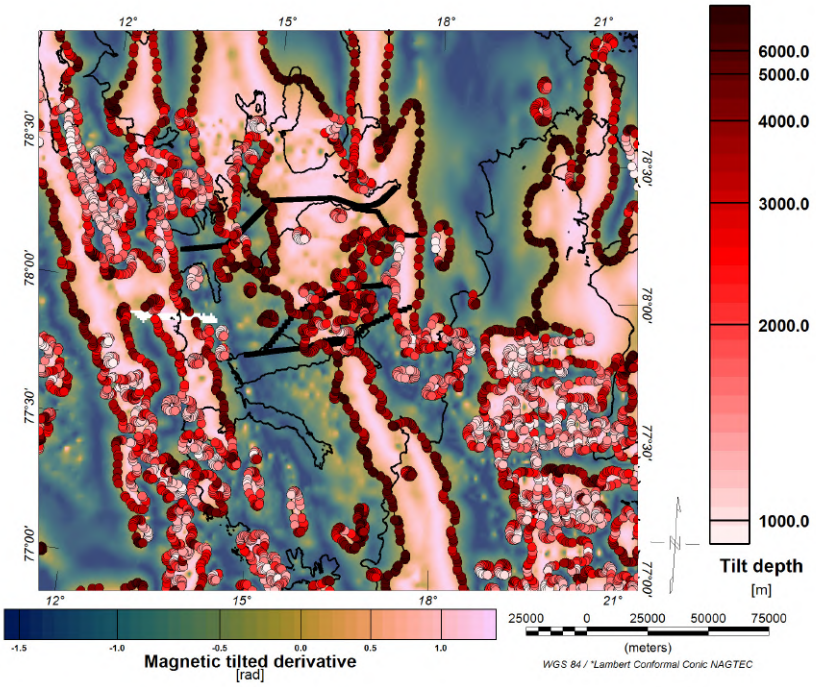

Figure 5.4: The computed tilt depth along the zero contour of magnetic tilted derivative of the study area with a denser points sampling. It shows the BFZ results from a shallower source than the Isfjorden anomaly. The thick black lines indicate the location of the five data profiles used for forward modeling.

Combined potential fields

The combined outlined potential sources of both the magnetic and gravity data, see Figure 5.5, gave further insight into the regional trends. Dark purple regions are indicative of both a potential magnetic and gravity source in that region, due to magnetic susceptibility and density contrasts, respectively. Such an area was located along the northern segment of the BFZ. It becomes more ambiguous southwards where the gravity and magnetic potential sources show less overlap. Both the potential sources show fragmentation in Storfjorden, but no clear trends offsetting both potential sources can be observed. Another high in magnetic and gravity data can be observed of the western coast.

Most large onshore gravity sources coincide with the magnetic sources. The large Isfjorden magnetic anomaly did not have a gravitational counterpart, suggesting that the change in susceptibility did not coincide with a significant density contrast. All forward modeling data profiles shown in Figure 5.5 overlap with the gravity and magnetic potential source in the east, except for Profile RS.

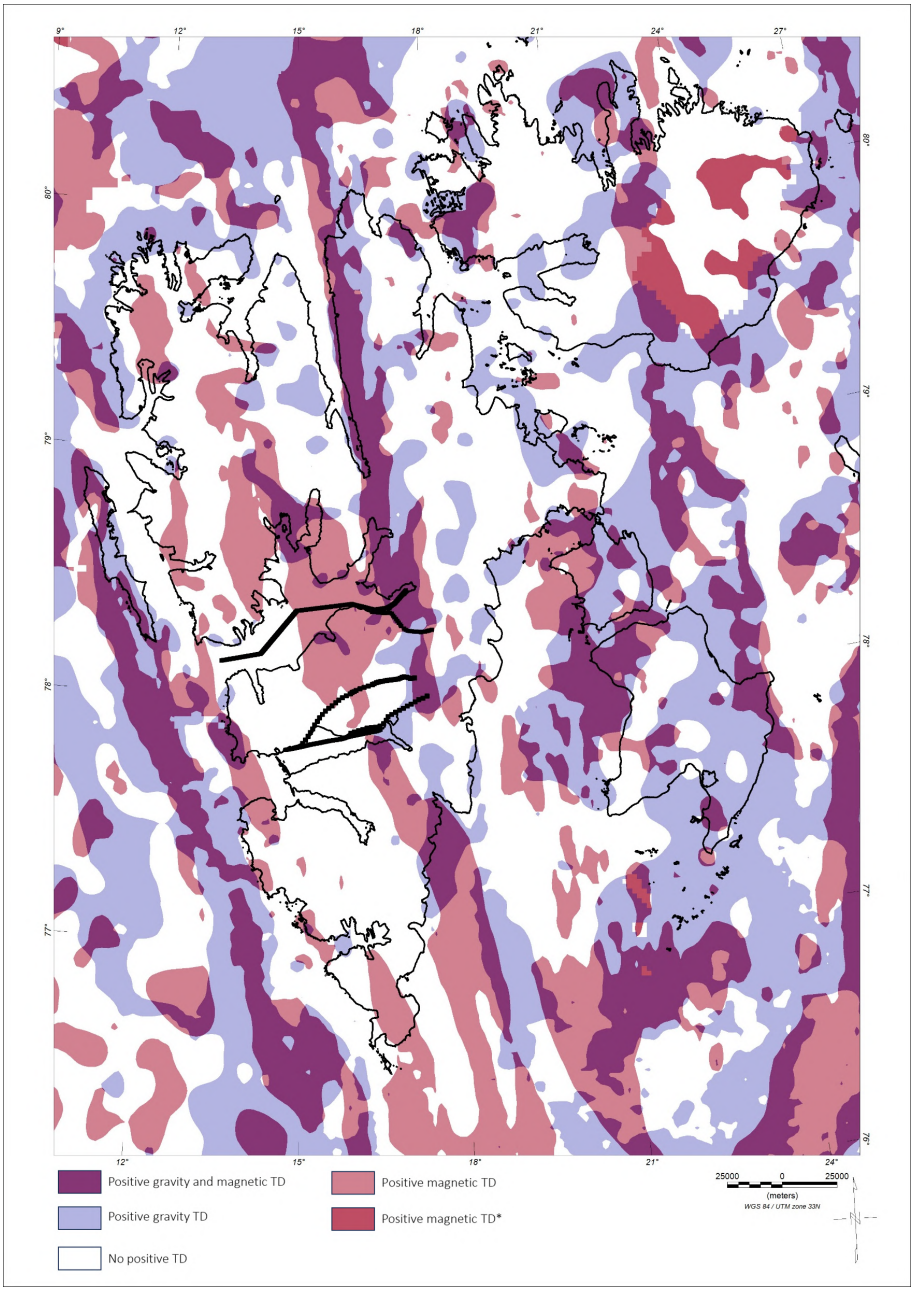

Figure 5.5: Svalbard overlain with areas with positive tilted derivatives (TD) for the magnetic and the gravity data. These areas are indicative of potential sources. The Isfjorden anomaly only shows in the magnetic data, while two lineaments along the BFZ and WSFTB are present in both magnetic and gravity data. The thick black lines indicate the location of the five data profiles used for forward modeling. *No gravity data available in this area.

5.2 2022 SvalGrav survey: data quality, processing and comparison to legacy data

Station spacing

The seven SvalGrav profiles have different station spacing as during acquisition deviations were made from the planned one kilometer spacing, see Figure 5.6. Profile 1 and 2 had the densest spacing and Profile 6 and 7 the coarsest. The average station spacing of the SvalGrav survey was 1.3 kilometers. This is of a much higher sampling density than the distribution of the previously acquired gravity stations that in the inland regions covered by the new survey often exceeded 5 kilometers between stations (Dallmann, 2015).

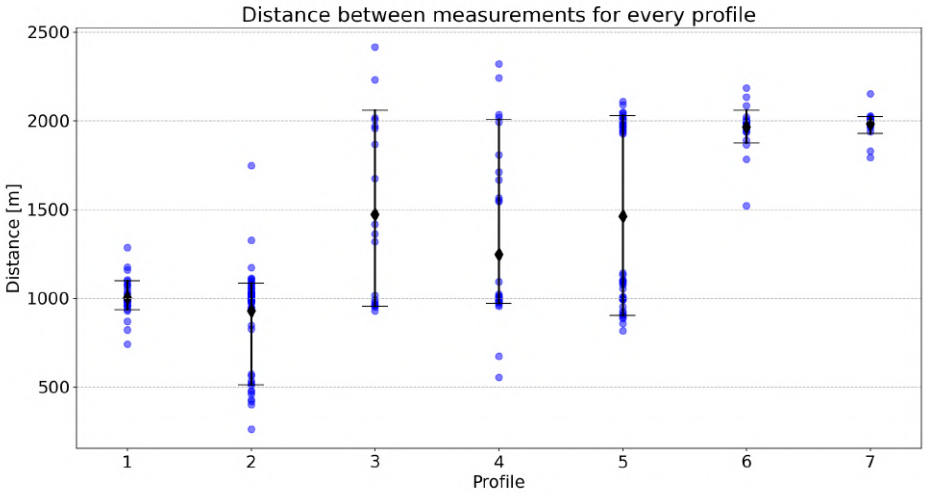

Figure 5.6: The distance between the gravity stations points for every SvalGrav profile. The mean distance is indicated with the black diamond and P10/P90 whiskers are added to visualize the range.

New vs legacy data

A quality comparison of the new SvalGrav data to the regional data documented by Olesen et al. (2010) and the effect of terrain correction was done by computing the correlation coefficient (R) (Schober et al., 2018) and mean average error (MAE) (Willmott & Matsuura, 2005). A good match between the data sets is indicated by R values close to 1 and low MAE values. Figure 5.7 shows that for all data combined a good fit existed. SvalGrav data without the terrain correction applied (5.7a) had a better fit to the regional grid than the terrain corrected data set (5.7b), both in terms of accuracy (MAE) and data trends (R).

The R and MAE of the seven individual SvalGrav profiles is shown in Table 5.1. SvalGrav data without terrain correction from Profile 1 and Profile 5 showed the best match to the regional data. Data trends along the individual profiles allowed insight into the source of the discrepancies. Figure 5.8 shows the Bouguer anomaly trends of Profile 2 with and without terrain correction in comparison to the regional data. Most of the error is due to more extreme fluctuations in highs and lows. A similar comparison for the other six profiles can be found in Appendix B.

We investigated whether this difference in station spacing per profile influenced the resulting match between the new and the old data. The MAE and R values were plotted against the mean station spacing of every profile, but no correlation was found. This suggested that discrepancies between the profiles in how well the new data match the legacy regional data are not due to the difference in station spacing.

Table 5.1: The computed correlation coefficient (R) and the Mean Average Error (MAE) for comparing the legacy regional data from Olesen et al. (2010) to the newly acquired SvalGrav data. TC indicates the value with the terrain correction are used.

Profile	R	R TC	MAE	MAE TC
1	0.982	0.975	1.725	3.719
2	0.875	0.903	2.669	2.239
3	0.800	0.702	3.674	1.973
4	0.928	0.967	1.772	2.075
5	0.997	0.997	1.884	4.981
6	0.684	0.694	1.715	1.922
7	0.995	0.987	1.978	1.697

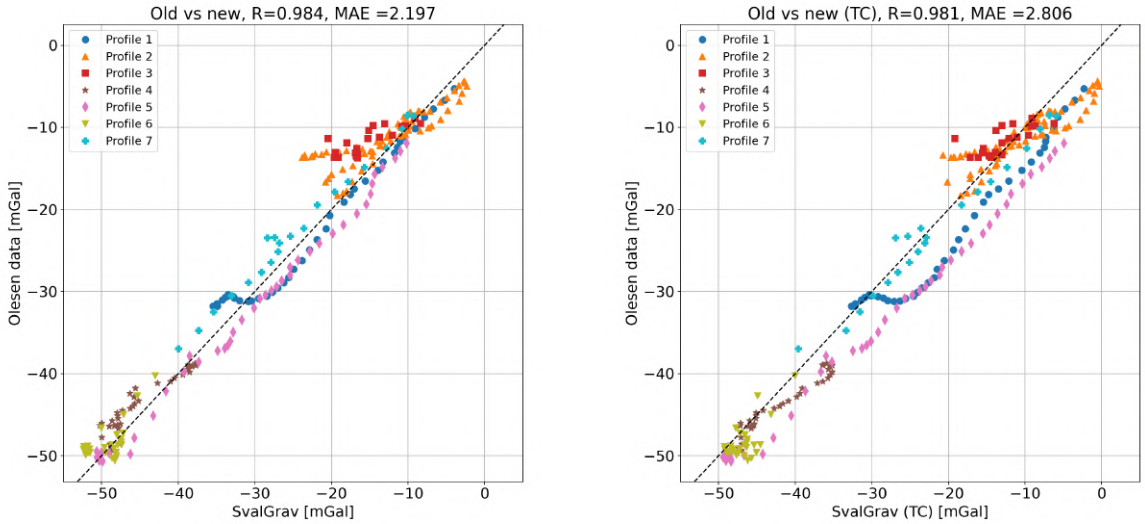

(a) Bouguer anomalies without terrain correction.

(b) Bouguer anomalies with terrain correction.

Figure 5.7: Comparison of the new SvalGrav data to the legacy regional data from Olesen et al. (2010) without (a) and with (b) terrain correction. The SvalGrav data set without the terrain correction has a smaller mean average error (MAE) and a higher correlation coefficient (R), indicating a better match to the regional data.

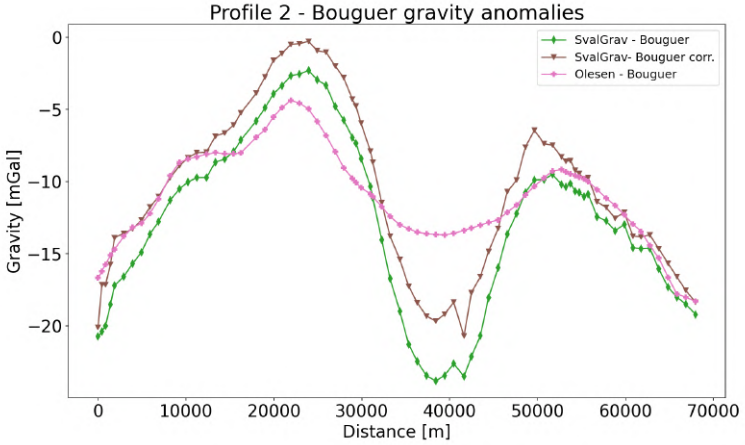

Figure 5.8: Data trends of new SvalGrav data with (brown) and without (green) terrain correction along Profile 2 compared with the regional data from Olesen et al. (2010). The data sets have a similar trend, but the new data have more pronounced variations. It should be noted that the Olesen et al. (2010) data were extracted along the profile from the grid, but not from actual station readings.

Plotting the difference in Bouguer anomalies on a map allowed us to put the data fit into regional context, see Figure 5.9. This was done for the SvalGrav data both without (5.9a) and with (5.9b) terrain correction. Smaller SvalGrav values (red) are mostly located along the west coast and in Sabine Land. Larger SvalGrav values (blue) are located around the center of Nordenskiöld Land. Adding the terrain corrections seems to overcompensate in quite some regions. The large misfit along Profile 3 is due to glacier crossing which has not been corrected for in this study. The misfit in Profile 2 is located in a narrow valley, suggesting the terrain effect on this section might be higher than computed. The high in data located to the west could have also elevated the magnitude of the regional interpolated data.

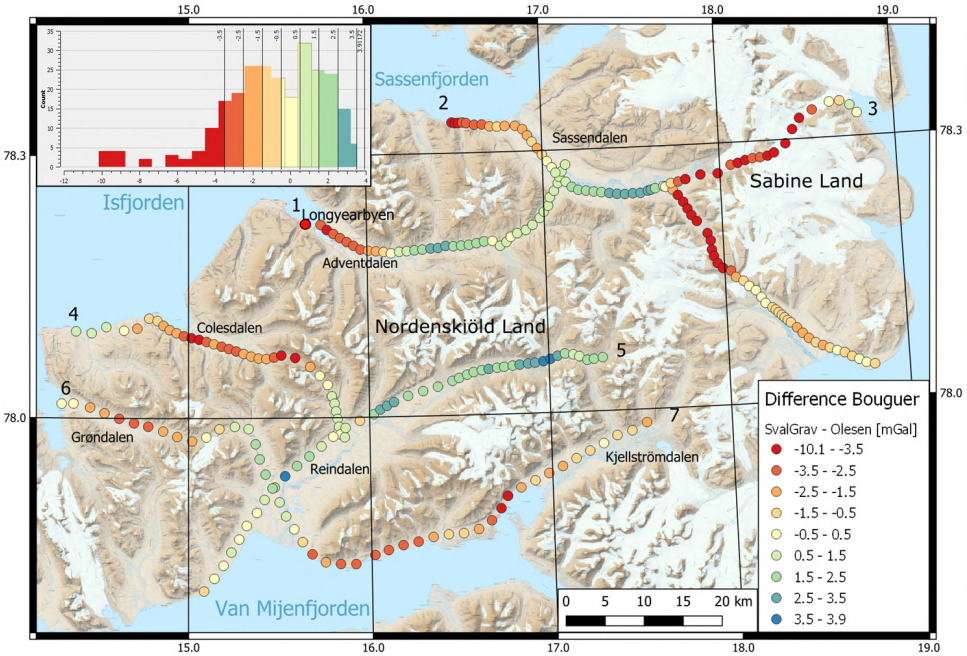

(a) Difference in Bouguer anomalies without terrain correction.

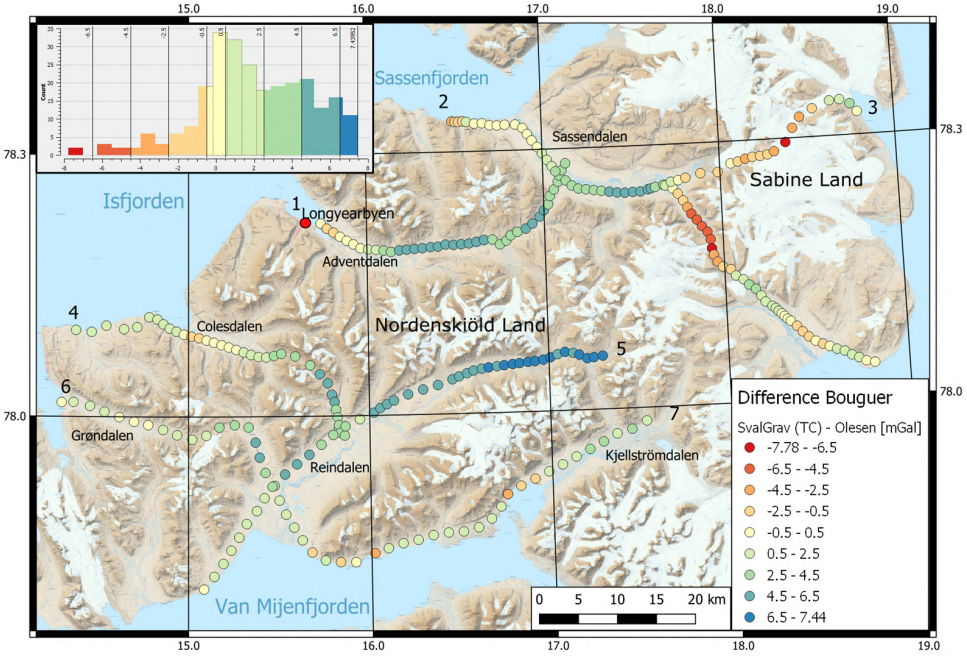

(b) Difference in Bouguer anomalies with terrain correction.

Figure 5.9: Difference in Bouguer anomalies between the SvalGrav survey and the regional legacy data Olesen et al. (2010) without (a) and with (b) terrain correction. Note the change in color scale between the figures. Numbers indicate SvalGrav profiles and inserted histograms show the distribution of the values.

5.3 Forward gravity and magnetic models

This section describes the results of the seismic interpretation and forward modeling along five profiles, starting with the northernmost model and moving south. Figure 5.10 shows an overview of the various lithostratigraphic units on Svalbard with their seismic tie as well as the density and susceptibility parameters used in forward modeling. The location of the model lines and the data profiles can be seen in Figure 5.11. Multiple scenarios were tested for all profiles, the best fit models will be shown in this section with some alternative scenarios presented in Appendix D.

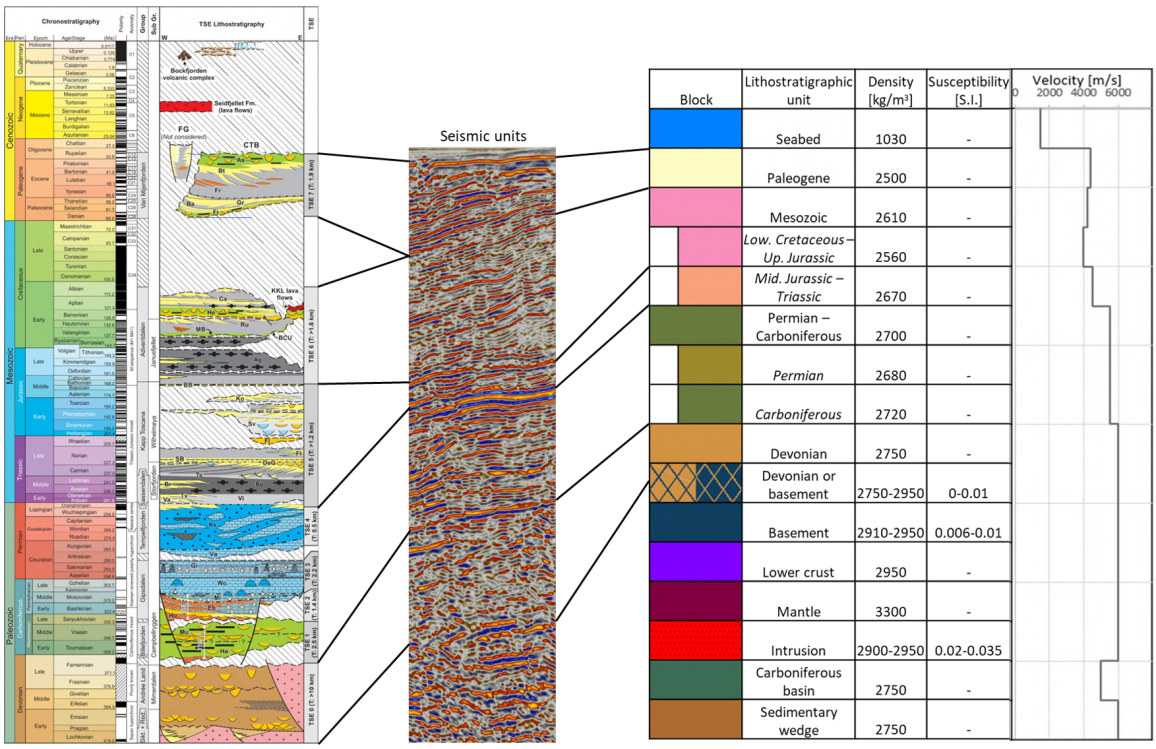

Block	Lithostratigraphic unit	Density [kg/m³]	Susceptibility [S.I.]
	Seabed	1030	-
	Paleogene	2500	-
	Mesozoic	2610	-
	Low. Cretaceous – Up. Jurassic	2560	-
	Mid. Jurassic – Triassic	2670	-
	Permian – Carboniferous	2700	-
	Permian	2680	-
	Carboniferous	2720	-
	Devonian	2750	-
	Devonian or basement	2750-2950	0-0.01
	Basement	2910-2950	0.006-0.01
	Lower crust	2950	-
	Mantle	3300	-
	Intrusion	2900-2950	0.02-0.035
	Carboniferous basin	2750	-
	Sedimentary wedge	2750	-

Figure 5.10: The seismic tie of the different lithostratigraphic units with their coinciding blocks used in forward modeling. The assigned color, density, susceptibility, and seismic velocity values are shown. Seismic tie is established on line SVA-VM-85-01. The lithostratigraphic column is adapted from Olaussen et al. (2023).

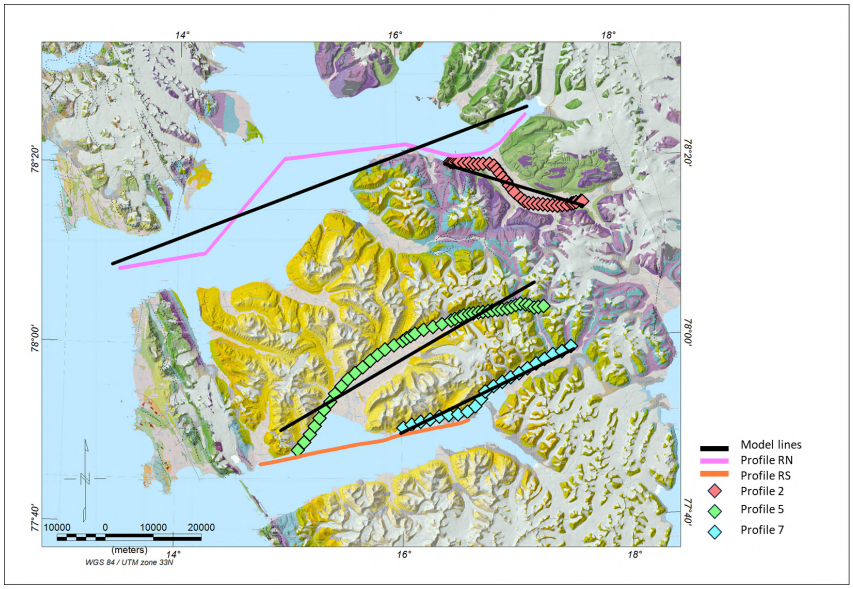

Figure 5.11: The data profiles and model lines of the five analyzed profiles. For Profile RS, the model line coincides with the data profile. Data is plotted on the geological map of Dallmann (2015).

5.3.1 Profile RN - Isfjorden

Profile RN stretches from the western end of Isfjorden towards Tempelfjorden with a NE-SW trend and a rough length of 90 kilometers. From east to west, it crossed the WSFTB, CSB and the BFZ. The seismic interpretation of the composite seismic line (E-W): ST8815-114, ST8815-222, ST8815-125 and NH8706-405 is shown in Figure 5.12.

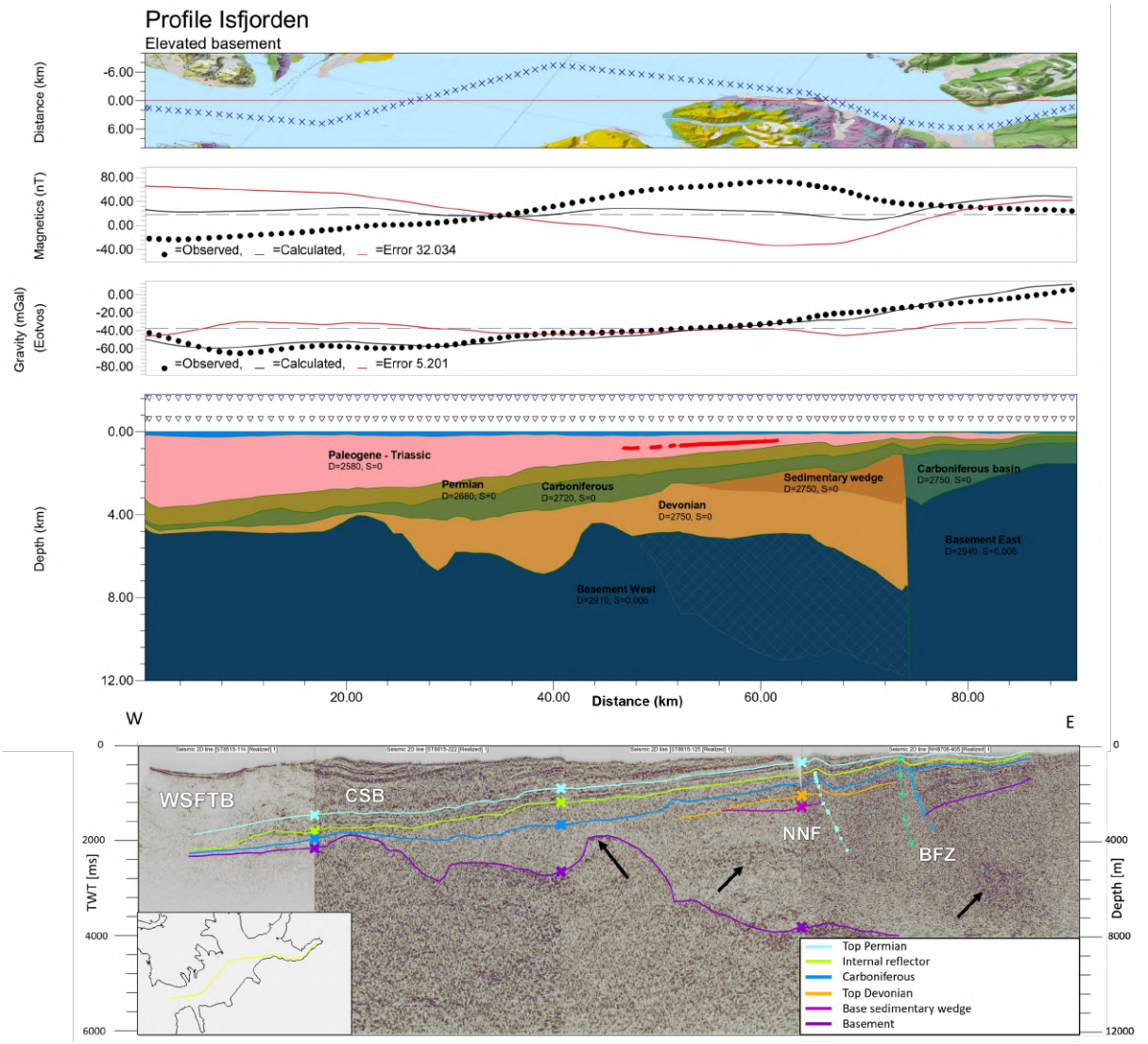

Figure 5.12: Forward model of Profile RN with an elevated basement and interpreted seismic section of lines (E-W) ST8815-114, ST8815-222, ST8815-125 and NH8706-405. The location of the data profile (crosses) and the model location (red line) are plotted on the geological map. The fit between the observations and calculations of the magnetic and gravity data is shown. The forward model shows the subsurface structure, where the blue and black triangles show the elevation of the magnetic and gravity data, respectively. The red points are sills identified in Senger & Galland (2022). A depth indication was added to the seismic interpretation using a seismic velocity of 4000 km/s. The inset shows the location of the seismic line, and the legend includes the identified horizons. Abbreviations: BFZ = Billefjorden Fault Zone, CSB = Central Spitsbergen Basin, NNF = No Name Fault and WSFTB = West Spitsbergen Fold and Thrust Belt.

Seismic interpretation

The westernmost part of the profile is located within the WSFTB, where the steeper orientation of the reflectors in combination with low seismic data quality makes the tracing of beds challenging. East of it, the synform Cenozoic sediments of the CSB are present on top of the Mesozoic succession.

The basement topography is based on the previous interpretation of Bælum & Braathen (2012). Three groups of strong discontinuous reflectors, indicated with the black arrows on Figure 5.12, were identified between 2000-3000 ms. The outline of these three groups were used as input for potential intrusions in one of the forward model scenarios, as seen in Figure 5.13.

On the easternmost seismic line, three faults were identified. The BFZ has two east-dipping faults which offset the basement against Devonian sediments and accommodate fault-propagation folds within the overlying strata. On the western side, another steep east dipping fault is shown in light blue and similarly folds the overlying strata. This fault was not previously mapped and is named No Name Fault (NNF) in our research. To the west of this fault a thin sedimentary wedge is identified of which the reflectors are truncated the Devonian reflector.

Based on the seismic interpretation, there were three feasible scenarios for the subsurface structure of Profile RN. Their validity was tested by constructing forward models. One model was created with the basement topography according to Bælum & Braathen (2012), one model with an alternative elevated basement (Figure 5.12) and a final model which included the intrusions (Figure 5.13). These latter two models had the best fit, the worst fitting model with the basement topography according to literature can be found in Appendix D.

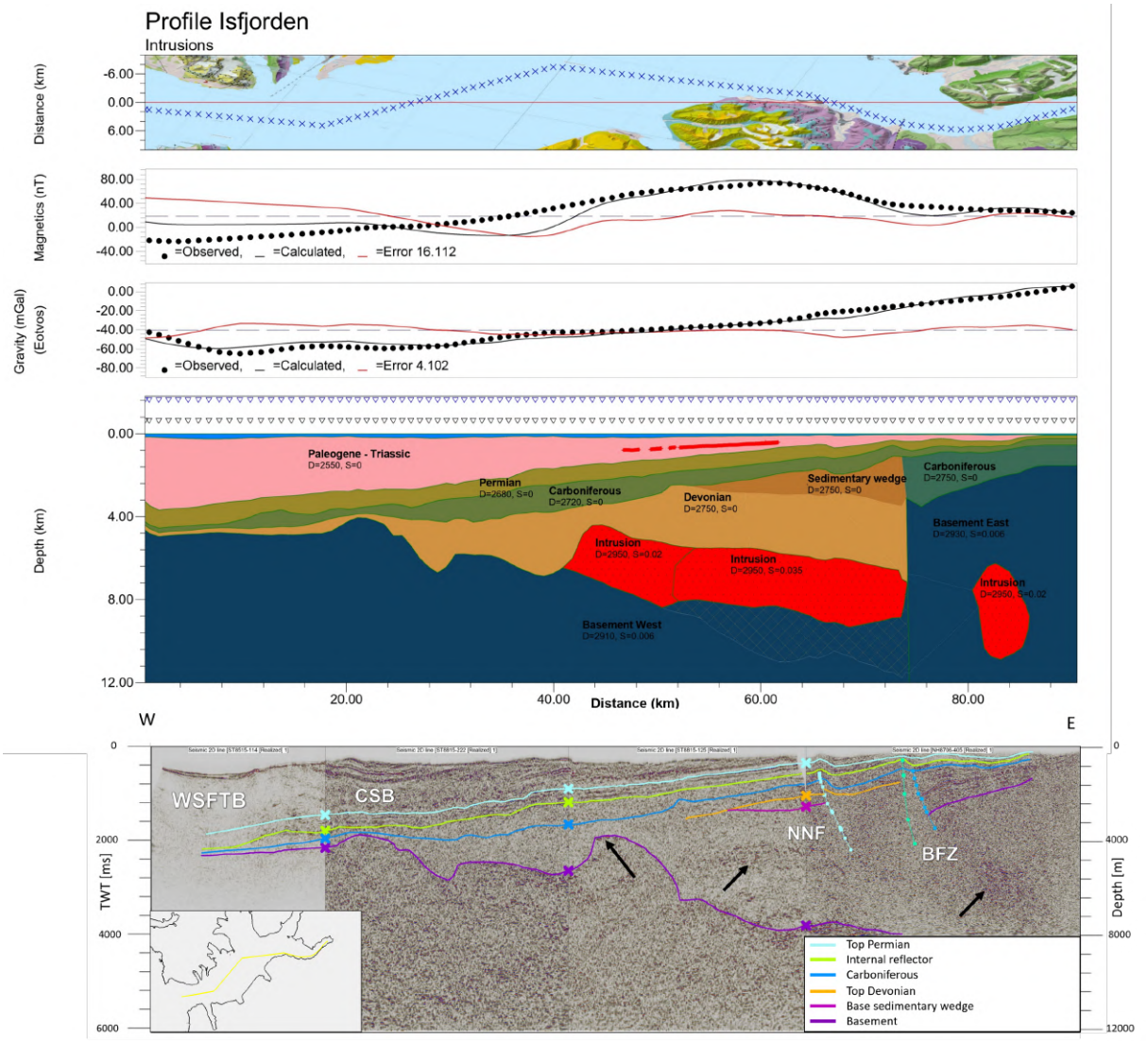

Figure 5.13: Forward model of Profile RN with included intrusions and interpreted seismic section of lines (E-W) ST8815-114, ST8815-222, ST8815-125 and NH8706-405. The location of the data profile (crosses) and the model location (red line) are plotted on the geological map. The fit between the observations and calculations of the magnetic and gravity data is shown. The forward model shows the subsurface structure, where the blue and black triangles show the elevation of the magnetic and gravity data, respectively. The red points are sills identified in Senger & Galland (2022). A depth indication was added to the seismic interpretation using a seismic velocity of 4000 km/s. The inset shows the location of the seismic line, and the legend includes the identified horizons. For abbreviations, see Figure 5.12.

Forward model

The gravity data (Figure 5.12) show a low on the west of the profile with increasing values towards the east. The magnetic data showed a high around 60 kilometers east of the start of the model, with a steeper gradient on the eastern side. The model according to the Bælum & Braathen (2012) interpretation with a thick Devonian basin (Appendix D) had a bad fit to both magnetic and gravity data, especially in this basin region. Susceptibility values of the sedimentary package of about 0.018 SI would have been necessary to match the magnetic trend. The relatively low density of the Devonian rocks also causes a low in the computed gravitational values which is absent in the data.

The model with an elevated basement (Figure 5.12) showed a better fit in terms of gravity data. However, the basement topography was not sufficient to match the observed gravity values. A density heterogeneity was introduced in the basement, increasing the density east of the BFZ with 30 kg/m^3. While the fit to the magnetic data had improved, even with the elevated basement it was not possible to explain the observed magnetic anomalies without introducing large and local susceptibility contrasts in the basement.

Profile RN partly overlies the Isfjorden anomaly previously identified in the regional trends section. It has a long wavelength signal and various igneous sills were identified in the area (Senger & Galland, 2022). Combining this knowledge with the observations of the strong discontinuous seismic reflectors, it suggested the potential presence of large magmatic bodies in the subsurface. These were added to the final model based on their location in the seismic data and suitable susceptibilities were assigned to match the magnetic data, see Figure 5.13. Due to the higher density of igneous rock, the trend of gravity data could also be fitted. The computed dips on the side of the magnetic anomaly are stronger than those of the observed values, this could be due to the coarse interpolation of the regional grid. By adding the intrusions, the density contrast between the eastern and western basement was reduced to 20 kg/m^3. The sedimentary wedge and Carboniferous basin as identified in the seismic section did not seem to have a noteworthy influence on the resulting potential field anomalies.

5.3.2 Profile 2 - Sassendalen

Profile 2 is located east of Profile RN in Sassendalen. It consists of the western part of the SvalGrav profile from station 1 - 35. It has a curved, roughly WNW-ESE orientation and a length of about 30 kilometers. It crosses the surface expression of the BFZ on the westernmost edge where there is no seismic coverage. The seismic interpretation (Figure 5.14) was established on a composite line (E-W) of NH8802-14 and NH8802-12.

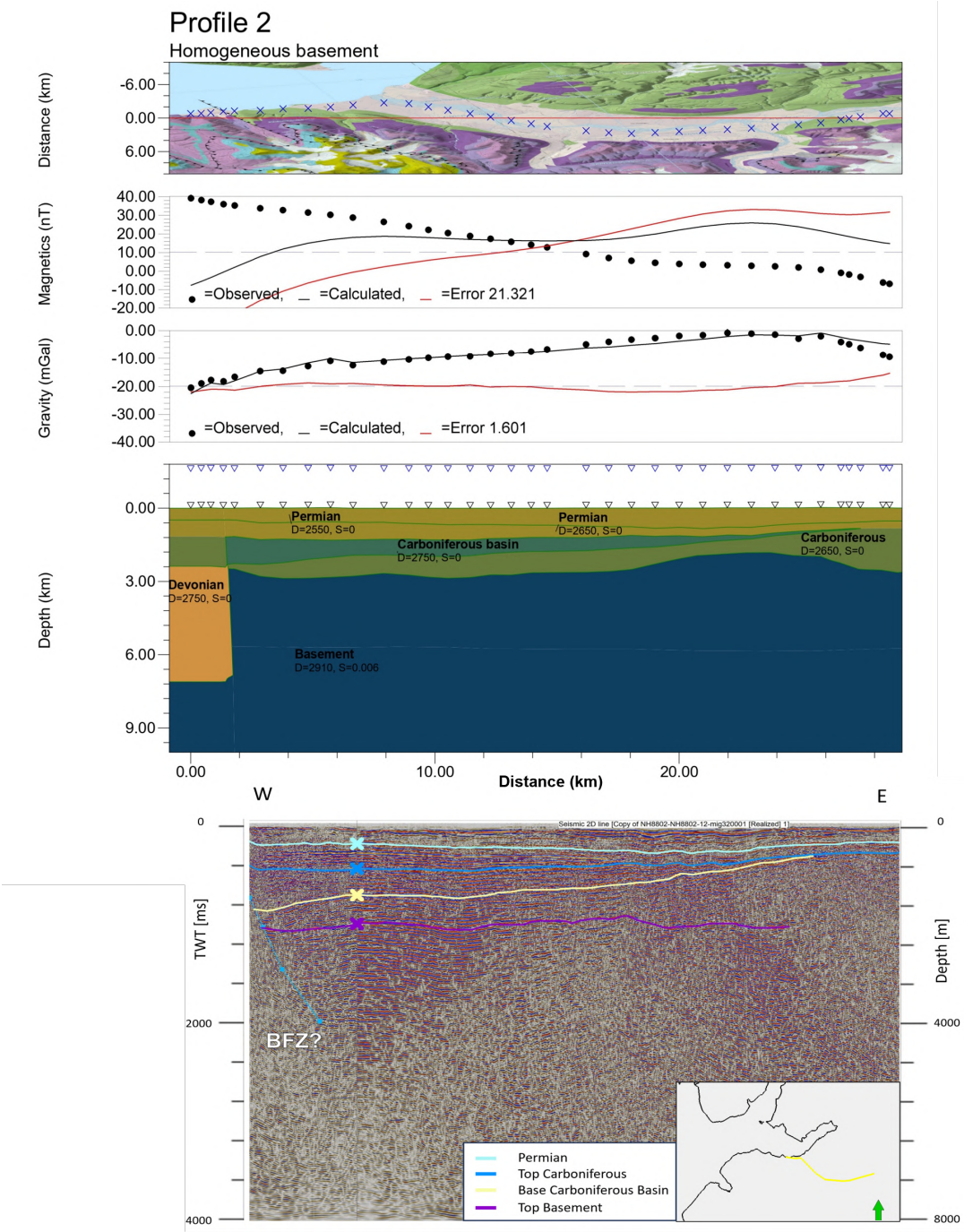

Figure 5.14: Forward model of Profile 2 with a homogeneous basement and interpreted seismic section of lines (E-W) NH8802-14 and NH8802-12. The seismic data do not cover the western edge of the model. The location of the data profile (crosses) and the model location (red line) are plotted on the geological map. The fit between the observations and calculations of the magnetic and gravity data is shown. The forward model shows the subsurface structure, where the blue and black triangles show the elevation of the magnetic and gravity data, respectively. A depth indication was added to the seismic interpretation using a seismic velocity of 4000 km/s. The inset shows the location of the seismic line and the legend includes the identified horizons. A sedimentary wedge thinning eastwards is visible and the Billefjorden Fault Zone (BFZ) which offsets sediments deeper down.

Seismic interpretation

The seismic lines of Profile 2 had limited resolution at depth as can be seen in Figure 5.14. Especially eastwards, the quality decreases making mapping of top basement challenging. The basement is overlain by a Carboniferous sedimentary package, in which a sedimentary wedge is pinching out eastwards. Permian sediments are located on top with some internal reflectors. The westernmost part of the composite line shows the potential location of the BFZ offsetting the basement against the Devonian basin at depth.

Forward model

The Bouguer anomalies along this profile were the highest of the entire SvalGrav survey. They increase eastwards, peaking around 25 kilometers with a steeper decline further east. The magnetic data gradually decreases from west to east. The forward model of Figure 5.14 has a good fit to the gravity data based on the topography of a homogeneous basement. Unlike Profile RN, no density heterogeneities needed to be introduced.

On the contrary, the computed magnetic data had a bad fit to the observed values and solely the basement topography was not sufficient to explain the trend in anomalies. A scenario was tested where a basement susceptibility heterogeneity was introduced in the model to match the data. This required the basement east of the BFZ to have a susceptibility of 0.001 SI, while the basement west of the BFZ had a susceptibility of 0.01 SI, see Appendix D. This did not coincide with basement susceptibility values used in other models nor with the geological constraints. Based on its location on the flank of the Isfjorden anomaly, the magnetic high was linked to the same source as the high seen on Profile RN. Extrapolating previous scenarios, this would be subsurface magmatic bodies. However, we did not identify strong discontinuous seismic reflectors mapping the outline of intrusive bodies and therefore they were not included in the forward model.

5.3.3 Profile 5 - Reindalen

Profile 5 is located in Reindalen in Nordenskiöldland with a NE-SW orientation and is about 60 kilometers long. Constraints for seismic interpretation were used from the Vassdalen and Reindalspasset boreholes. The profile is located in the CSB and crosses the BFZ in the east (Figure 5.15). The seismic interpretation is established on a composite line of (E-W) NH9108-07 and NH8802-32.

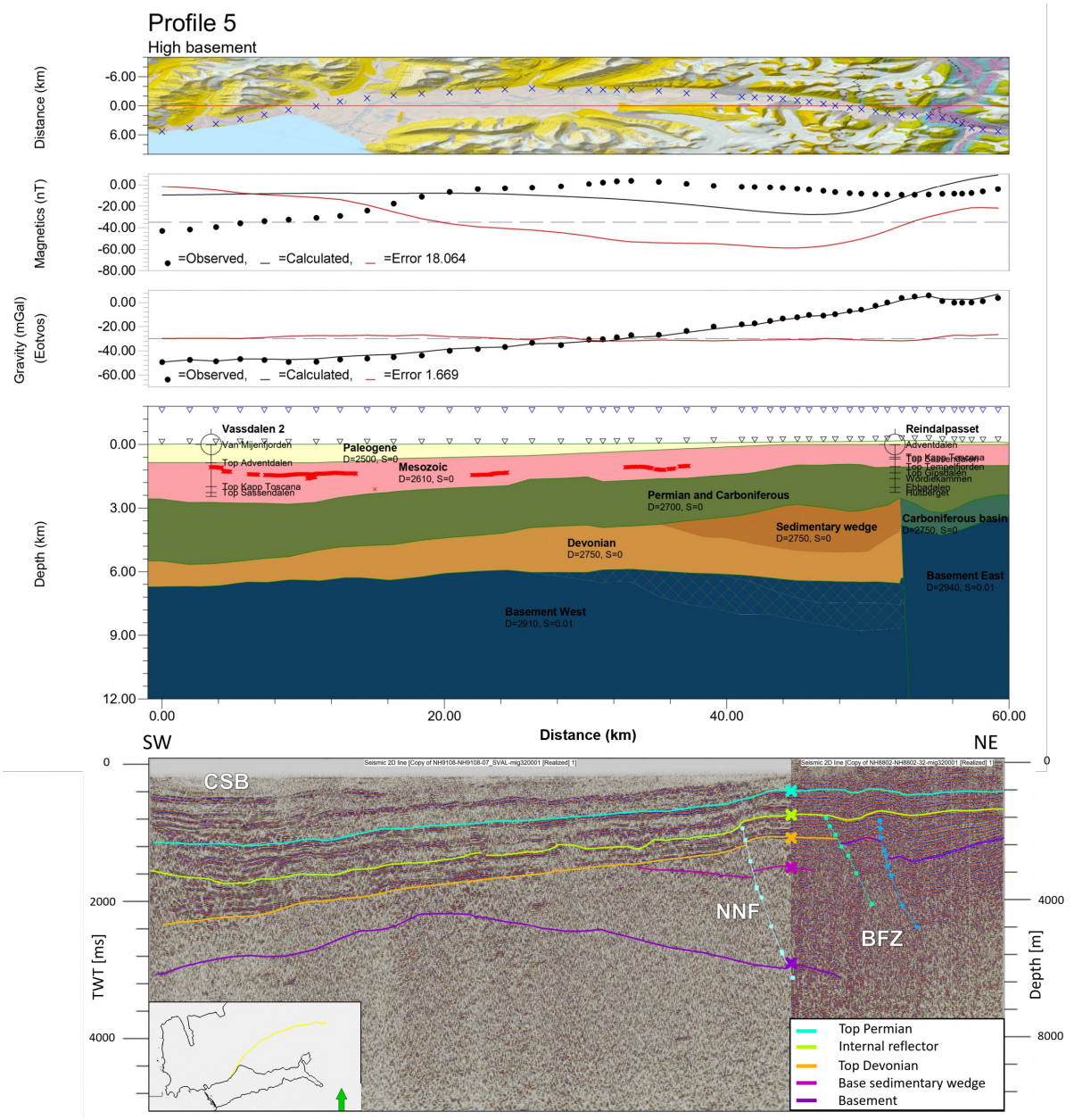

Figure 5.15: Forward model of Profile 5 with an elevated basement and interpreted seismic section of lines (E-W) NH9108-07 and NH8802-32. The location of the data points (crosses) and the model location (red line) are plotted on the geological map. The fit between the observations and calculations of the magnetic and gravity data is shown. The forward model shows the subsurface structure, where the blue and black triangles show the elevation of the magnetic and gravity data, respectively. The location of sills is shown with the red dots based on Senger & Galland (2022) and the stratigraphic constraints from the Vassdalen and Reindalspasset boreholes are included. A depth indication was added to the seismic interpretation using a seismic velocity of 4000 km/s. The inset shows the location of the seismic line and the legend includes the identified horizons. A sedimentary wedge is identified which is cut by the No Name Fault (NNF). The Billefjorden Fault Zone (BFZ) offsets the basement against the Devonian basin in the northeast. The Central Spitsbergen Basin (CSB) is in the southwest.

Seismic interpretation

Figure 5.15 shows that the Cenozoic sediments wedge out eastwards. The Mesozoic, Permian, and Carboniferous successions are tilted southwestwards and are overlying the top of the Devonian. The BFZ is present on the eastern section as two large east dipping faults. They offset the basement against the Devonian basin. Similar to Profile RN, again the large east dipping fault (NNF) west of the BFZ was identified. It seems to cut through the sedimentary wedge which is truncated by the top of the Devonian. There was no clear reflector marking the top of the basement in the west, the horizon indicates the estimated location.

Forward model

The forward model created based on the basement configuration of the seismic interpretation had a poor match with the potential field data, see Appendix D. By elevating the basement and introducing a basement density heterogeneity, as seen in Figure 5.15, it was possible to match the eastern increase in gravity. A density contrast of 2940 versus 2910 kg/m^3 was used, respectively east and west of the BFZ.

The magnetic data did not match with the basement topography and required large intra-basement susceptibility contrasts for the computed values to match the data. Alternatively, it might have resulted from a magmatic body as was found on the previous two models. Looking at the extent of the long-wavelength Isfjorden anomaly in Figure 5.1, it overlaps the center of Profile 5. Additionally, the location of the magnetic high coincided with previously identified sills from Senger & Galland (2022). As no supporting seismic reflectors constraining the intrusion location were identified, it was not included in the model but is the favored solution for explaining the discrepancy between the computed and observed magnetic values.

5.3.4 Profile RS - Van Mijenfjorden

Profile RS is located in Van Mijenfjorden with a WSW-ENE orientation and about 45 kilometers long. It runs perpendicular to the CSB and overlaps the WSFTB on the westernmost edge (Figure 5.16). The seismic interpretation is partly constrained by the Ishøgda borehole and established on line SVA-VM-85-01.

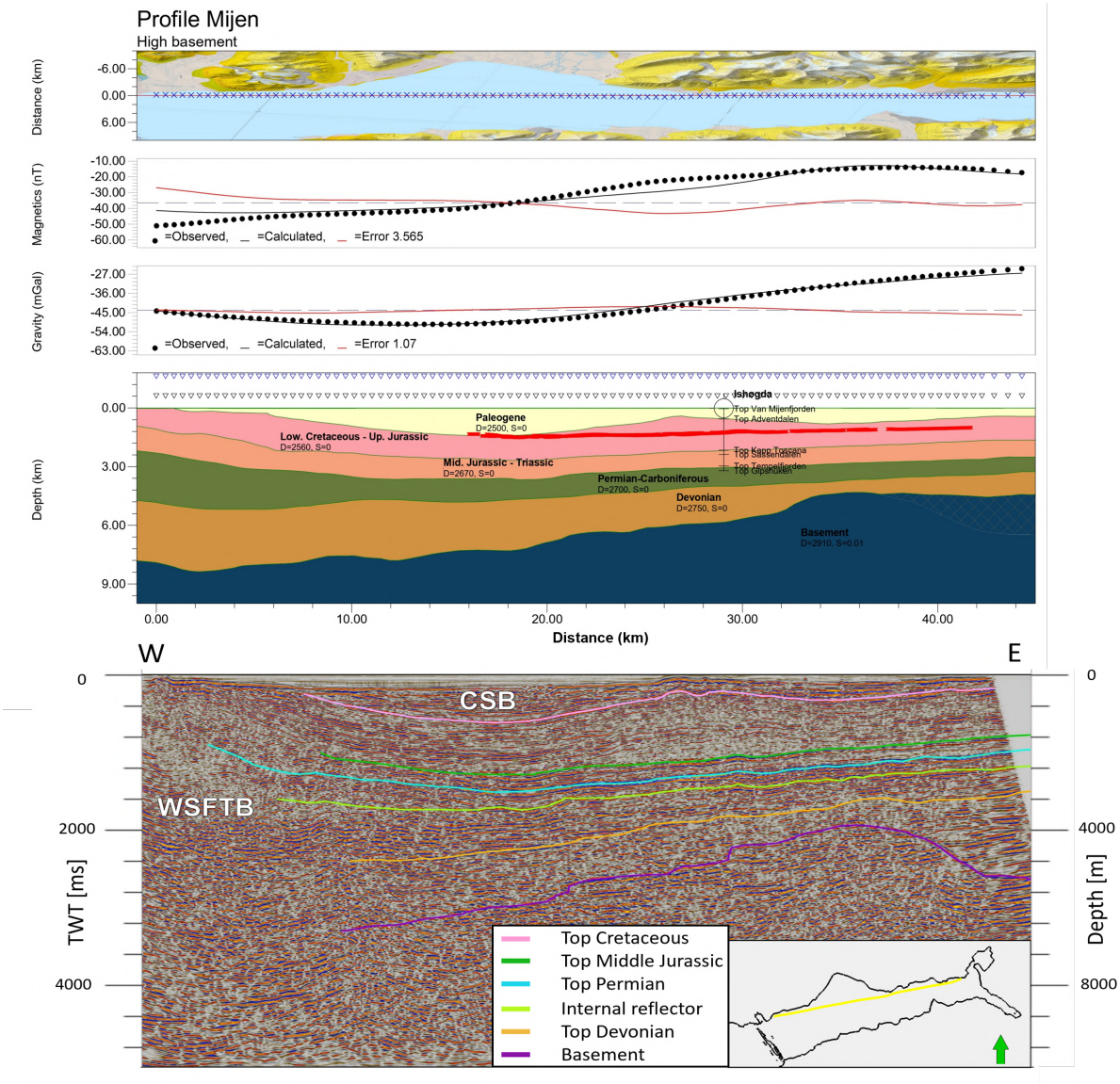

Figure 5.16: Forward model of Profile RS with an elevated basement in the east and interpreted seismic line SVA-VM-85-01. The location of the data points (crosses) and the model location (red line) are plotted on the geological map. The fit between the observations and calculations of the magnetic and gravity data is shown, together with the corresponding error. The forward model shows the subsurface structure, where the blue and black triangles show the elevation of the magnetic and gravity data, respectively. The red line in the model indicates the presence of sills as identified in Senger & Galland (2022). A depth indication was added to the seismic interpretation using a seismic velocity of 4000 km/s. The inset shows the location of the seismic line and the legend includes the identified horizons. The Central Spitsbergen Basin (CSB) is located in the middle of the profile with the West Spitsbergen Fold and Thrust Belt (WSFTB) in the west.

Seismic interpretation

The seismic section of Figure 5.16 shows the synclinal CSB with Cenozoic and Mesozoic sediments. The seismic reflectors are mostly continuous but the effect of the WSFTB is visible on the western edge by the increasingly steeper tilted reflectors. The basement topography shows an antiform on the eastern side. However, the reflectors at the edge are not conclusive.

Forward model

The forward model with a geometry according to the basement horizon showed a misfit with the data on the eastern side, having both lower gravitational and magnetic anomalies, see Appendix D. A model with an elevated basement showed the best fit to the data as seen in Figure 5.16. Both the gravity and magnetic data trends match with the topography of a homogeneous basement with a density of 2910 kg/m^3 and a susceptibility of 0.01 SI. The small misfit in magnetic data around 25 kilometers coincides with the location of a previously identified sill, offering a plausible explanation for the local increase in magnetic signal deviating from the computed values of the basement topography.

5.3.5 Profile 7 - Van Mijenfjorden / Kjellströmdalen

Profile 7 is an eastward continuation of Profile RS, located in Van Mijenfjorden and Kjellströmdalen. It has a NE-SW orientation with a length of about 45 kilometers. The Ishøgda borehole is located on the outer western edge of the model. The profile crosses the BFZ in the east, where it offsets the basement against the Devonian basin at a depth of 4 kilometers (Figure 5.17). The seismic interpretation was established on a composite line of (E-W): SVA-VM-85-01, leg 3 and leg 2 of the UNIS AG-351/851 Svea campaign and NH8903-21.

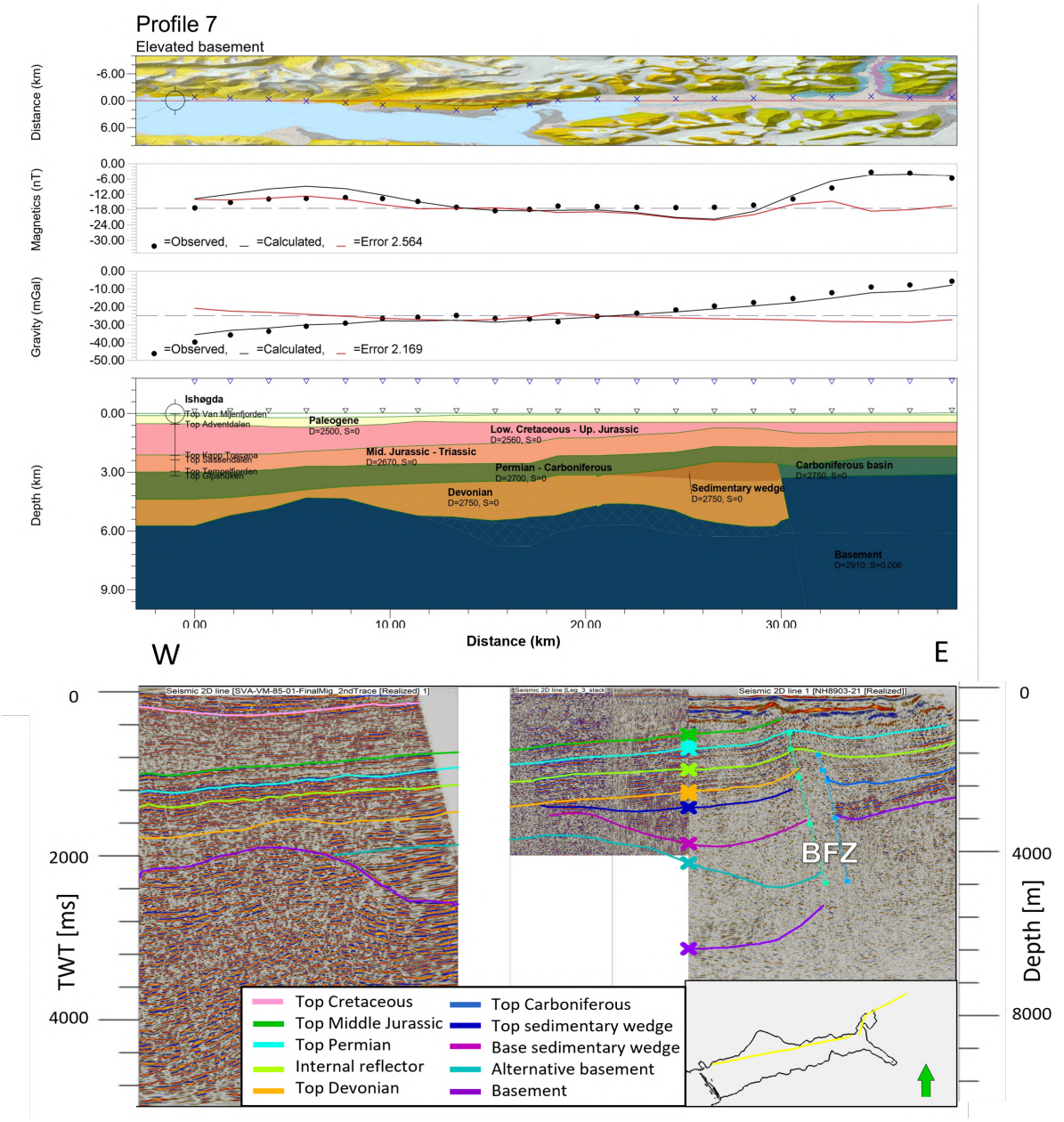

Figure 5.17: Forward model of Profile 7 with an elevated basement and interpreted seismic line (E-W) SVA-VM-85-01, AG351-3,-2 and NH8903-21. The location of the data points (crosses) and the model location (red line) are plotted on the geological map. The fit between the observations and calculations of the magnetic and gravity data is shown. The forward model shows the subsurface structure, where the blue and black triangles show the elevation of the magnetic and gravity data, respectively. A similar sedimentary wedge was identified as on Profile RN and Profile 5 and the Billefjorden Fault Zone (BFZ) offsets the basement against the Devonian. Two basement scenarios were interpreted.

Seismic interpretation

The composite seismic line of Profile 7, see Figure 5.17, exists in the west out of the same data as Profile RS. The Mesozoic succession is truncated by a major detachment on the eastern edge of the profile. Strong reflectors evident of the Carboniferous basin are located on the east of the BFZ, which offsets the basement against the Devonian. As the seismic reflectors are inconclusive, two proposed basement configurations are shown. The sedimentary wedge which was previously observed on Profile RN and Profile 5 is also present in this section. It again is truncated by the top of the Devonian. However, the east dipping fault (NNF) found on those profiles was not identified within this section. Some discontinuation of reflectors was observed in the projected location of the fault, but they were too inconclusive to interpret a fault on.

Forward model

The model with an elevated basement according to the turquoise horizon had the best fit to the data, see Figure 5.17. The alternative scenario with a lower basement can be found in Appendix D. The gravity showed a steady increase towards the east, which matched with the elevated basement resulting from the BFZ. The magnetic data peaks on the eastern edge, coinciding with the elevated basement. A homogeneous basement in terms of susceptibility and density matched the observed potential field data based on its topography. This is according to the expectations of the regional trends, which showed that the Isfjorden anomaly did not interact with this profile.

5.3.6 Combined observations

In general, the sedimentary layers have a limited effect on the observed trends in potential field data. The basement topography was able to explain most of the gravity anomaly trends. The general increase of gravity towards the east was explained by elevated metamorphic basement along the BFZ. On Profile RN and Profile 5, a denser basement in the east was necessary to match the data, an increase of 30 kg/m^3. Furthermore, most models showed a better fit to the data with a thinner Devonian basin and therefore a higher placement of the basement topography. This deviated between about 1 kilometer to 4 kilometers along Profile RN. The gravity DC shift for all forward models was in a similar range, showing the consistency between the models.

Basement magnetic susceptibility values between 0.006 and 0.01 SI were used between the five different profiles, but no internal heterogeneities were introduced. Only the two southern profiles, Profile RS and Profile 7, were able to explain the observed magnetic data based on the basement topography. The other three models were overlaying the Isfjorden anomaly of Figure 5.1, and the magnetic data trend did not match with the basement topography. Igneous intrusions included in Profile RN based on the location of shallow igneous sills and stronger seismic reflectors helped explain the magnetic data trend. As the seismic sections of Profile 2 and Profile 5 did not allow the identification of potential magmatic bodies, none were included in the forward modeling and no good fit to the magnetic data was obtained on these profiles. The magnetic DC shift was not consistent between the forward models as it needed to compensate for 3D effects of the regional data on the simplified 2D profiles.

6 Discussion

The results of the regional data analysis are discussed, after which the scope focuses on the study area by discussing the SvalGrav field data and the outcome of the seismic interpretations and forward models. Their geological implications as well as the limitations and future opportunities are discussed.

6.1 Regional potential field trends

6.1.1 Magnetic trends

Comparing the low-pass filtered magnetic anomalies with the original grid showed roughly the same trend in the anomalies. Figure 6.1 shows the subsurface igneous sills and the outcropping Diabasodden Suite dolerites as identified in Senger & Galland (2022) overlaying the magnetic anomaly data (Figure 6.1a) and the outlined potential magnetic sources (Figure 6.1b). Interestingly, only in the Isfjorden area (1) is there a good match between the igneous rocks and the magnetic data. Two large patches of the outcropping Diabasodden Suite are visible in eastern Sabine Land (2) and between Ny-Friesland and Nordaustlandet (3) but are barely represented in the magnetic data. This lack of correlation shows the sensitivity of the aeromagnetic data to the long wavelength signal due to the sparse data density. It suggests that the large Isfjorden anomaly is linked to a long wavelength signal with a deeper source rather than it being explained by the high frequency shallow sills identified in Senger et al. (2023).

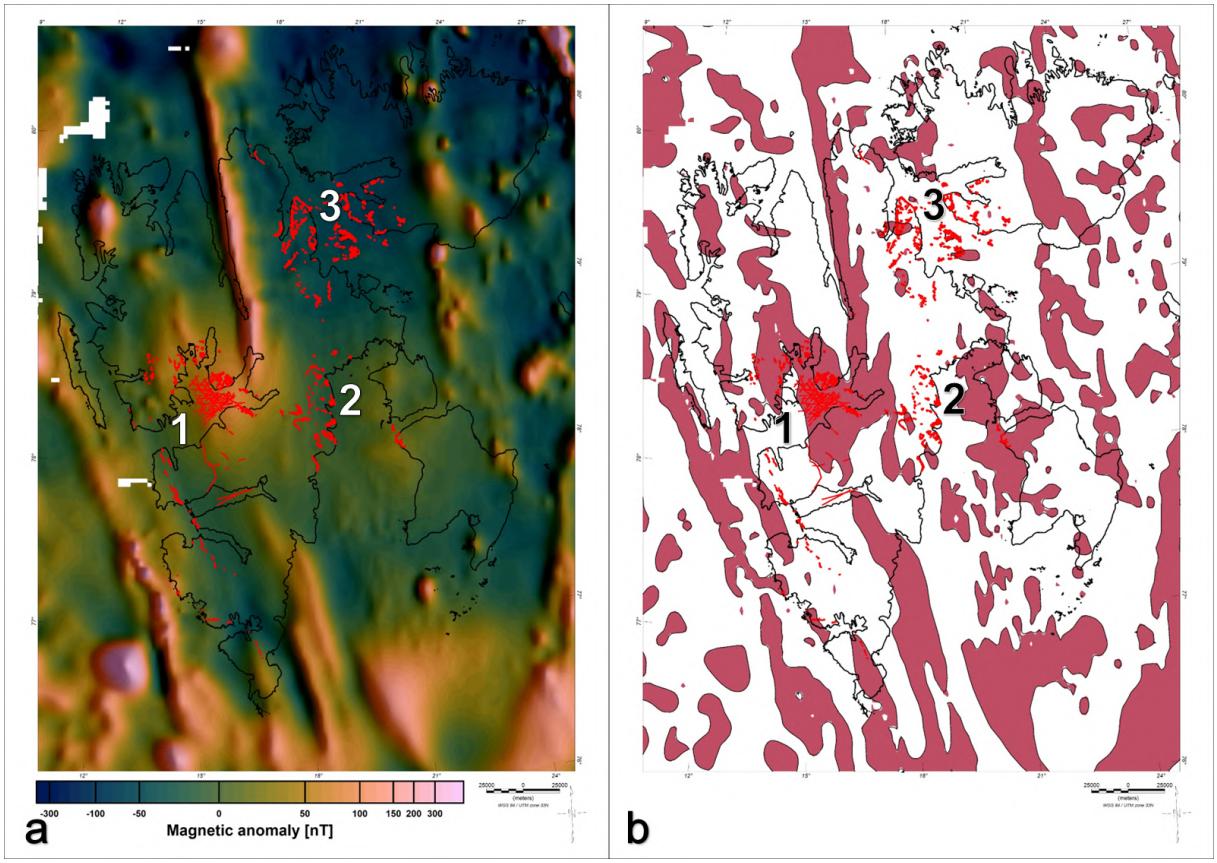

Figure 6.1: Correlation between outcropping Diabossoden Suite and intrusions mapped in seismic data from Senger & Galland (2022) with a) the magnetic anomalies and b) potential source regions.

The NNW-SSE trending magnetic source in the north shows a good correlation with the BFZ. As the BFZ has elevated the magnetic Atomfjella Complex and offset it against Devonian sediments, this can be seen as a likely source for the magnetic anomaly and matches previous interpretations by Dallmann (2015). The data from the tilt depth which described the anomaly to be relatively shallow matches with that observation.

Further south, the Isfjorden anomaly intertwines with the otherwise roughly linear trend of the BFZ anomaly. The deeper tilt depth of this source matches with the long wavelength signal and suggests this anomaly has a different origin than the shallow BFZ anomaly. As previously described, the southward

extent of the anomaly can be divided into a relatively deep western leg and a shallower eastern leg. Based on the depth and the knowledge of the regional geology, the favored scenario is the eastern anomaly being a continuation of the BFZ while the western anomaly is part of the Isfjorden anomaly.

While the presence of the Isfjorden anomaly has been previously addressed in literature (Dallmann, 2015), no explanation for its existence was provided. There are various scenarios which would account for the local subsurface susceptibility increase. The shape of the anomaly deviates from the roughly N-S trending basement terranes present on Svalbard as previously described. This makes the scenario that the anomaly is caused by a basement susceptibility heterogeneity unlikely and favors a more local feature. Such a local increase in susceptibility could for example be caused by a magmatic body in the subsurface or the presence of a hydrothermal system.

6.1.2 Gravity trends

Similar to the magnetic data, a positive gravity anomaly with a NNW-SSE orientation coincides with the BFZ and can therefore be explained by an elevated basement along the fault zone. The southward weakening of the anomaly can be explained by the general southward tilt of Svalbard. The basement becomes overlain by a thicker sedimentary package dampening the signal. The large negative anomaly west of it coincides with the CSB and can be explained by a locally thicker crust, pushing denser layers further down and therefore reducing the mass. This matches previous observations in Dallmann (2015).

6.1.3 Combined magnetic-gravity trends

The dark purple regions of Figure 5.5 showing potential gravity and magnetic sources match with the HFC and the BFZ. The HFC forms the continental-ocean boundary, resulting in additional mass from accumulated sediments and a higher magnetic signal due to the mafic rocks. The increase of both density and susceptibility values at the BFZ hints towards an influence of the basement and matches with the knowledge that the BFZ elevates the basement. This further supports the conclusions drawn based on the individual gravity and magnetic trends.

The lack of potential gravity source for the Isfjorden magnetic anomaly indicates that there is only a change in subsurface susceptibility. In the scenario where a change in basement composition is responsible for this susceptibility increase, one might expect to see a density and therefore gravity contrast as well. While there is no linear relationship between the density and susceptibility of basement rock, the study of Krasil'ščikov et al. (1995) did find in general higher density values for basement samples with a higher susceptibility on Svalbard. Therefore, the absence of a coinciding gravity high makes the hypothesis that a basement heterogeneity is responsible for the local susceptibility less likely. This further supports the interpretation in the magnetic section, where the scenario was discounted on basis of the anomaly shape.

It should be noted that care must be taken when making onshore-offshore data correlations on the potential field data. Thicker offshore sedimentary packages can dampen some of the magnetic signal while it has a less prone effect on the gravity data. Additionally, one should always be wary for potential processing artifacts when looking at interpolated potential field data with a sparse data density.

6.1.4 Storfjorden seismicity

As we observe both seismic activity and potential field anomalies in the Storfjorden area, see Figure 6.2, it was investigated whether the anomalies were linkable to the same fault system responsible for the earthquakes. Grogan et al. (2000) discusses Paleozoic faults which functioned as pathways for igneous rock leading to magnetic anomalies east of Svalbard. These faults were difficult to image in the seismic data due to their vertical orientation.

Likewise, it was not possible to identify a candidate fault zone in Storfjorden on seismic reflection data due to the sparse data availability. Therefore, the link between the anomalies and fault activity was investigated by plotting the earthquake locations on the map of the potential sources, see Figure 6.2. Pirli et al. (2013) link the seismicity to a rupture along an oblique normal fault with a dextral component which is trending NE-SW and dipping towards the SE. They correlate it to a Paleogene NE-SW trending shear zone in the Sørkapp-Hornsund region as described in Bergh & Grogan (2003). In our data, there was no clear correlation observed between the seismicity and the potential field anomalies. Further investigation into alternative scenarios is therefore necessary to explain the presence of the anomalies in Storfjorden.

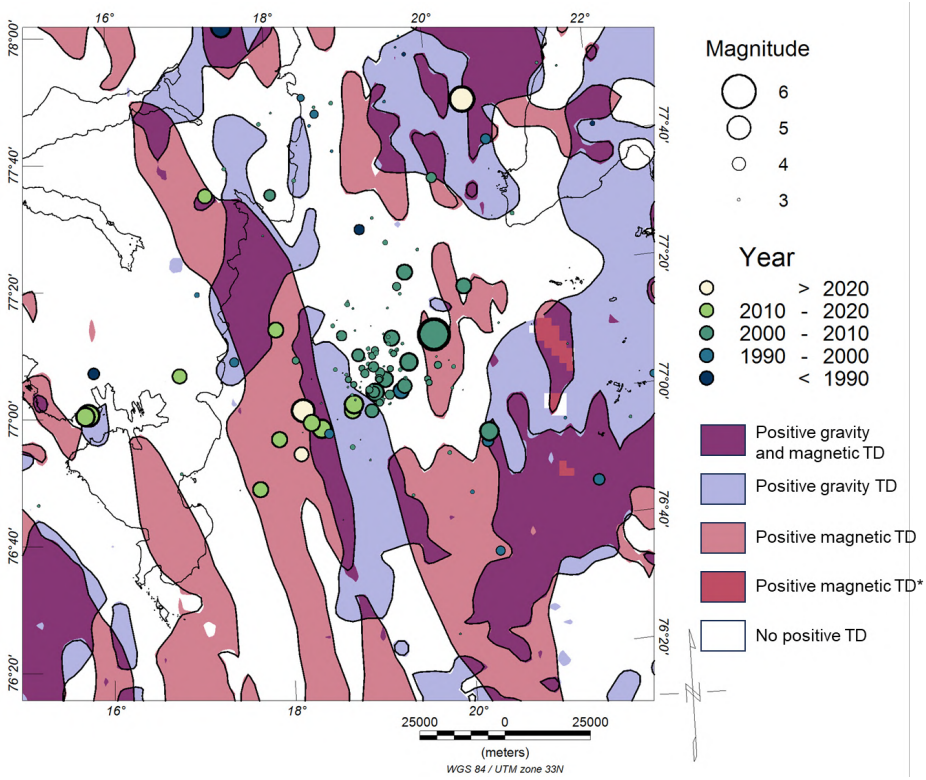

Figure 6.2: Location of earthquakes from 1980-2023 with the outlined sources of the anomalies. Legend of the outlined sources according to Figure 5.5. Earthquakes with a minimum magnitude of 2.7 and 4 were included for respectively the 1980-2012 period and 2013-2023 period. The earthquake locations do not match the trend of the magnetic anomalies and rather suggest the presence of a NE-SW trending fault system.

6.2 Field survey

The comparison of the SvalGrav data to the regional grid of Olesen et al. (2010) was useful for analyzing the general trends of the acquired gravity data. It showed a satisfactory fit. Further analysis of the SvalGrav data in comparison to previously acquired data at the actual station rather than the interpolated grid would be insightful but was beyond the current scope of the study. Based on the results, it was concluded that some further finetuning of the terrain correction might enhance the data quality but was again beyond the temporal and computational scope of this study.

Previous gravity surveys in Svalbard were executed using helicopters, marine vessels for offshore acquisition or small boats for landings to collect gravity data along the shoreline. The usage of snowmobiles in the SvalGrav survey allowed for quicker travelling between stations that were located largely in the interior. Traditionally, these were only accessible by helicopter with associated economic and environmental costs. However, it does require doing fieldwork in the Arctic spring, exposing both the surveyors and equipment to sub-freezing temperatures. Field gravity surveys in other Arctic regions, such as Prudhoe Bay, Alaska, used a Tucker Sno-Cat as mode of transport (Ferguson et al., 2007). A bandwagon provides additional shelter for the acquisition team. However, it also has more limited mobility due to slow operation speed during transit and previous surveys faced issues with broken equipment due to the bumpiness.

Our results showed that the average station spacing per profile did not impact the fit with the regional data. However, it would have been interesting to study how the detectability of density variation is dependent on the station spacing through forward modeling. This was beyond the scope of our research. It has been described before that the station separation should be smaller than the target depth to resolve the subsurface structure (Long & Kaufmann, 2013). It is furthermore beneficial for resolving targets to orientate your survey perpendicular to them. Future surveys could consider acquiring some additional data with very small station spacing along the lines, as this allows further insight into shallow features and noise sources (Long & Kaufmann, 2013).

The advantage of a gravity land survey is that one obtains the data in a static manner, allowing more precise location positioning and higher resolution data. Gravity acquired on moving platforms face more issues such as maintaining a stable elevation and dealing with turbulence (Fairhead & Odegard, 2002).

Additionally, from a financial perspective, the costs of operation are a lot smaller with a ground-based team compared to helicopter or airplane operations.

6.3 Constraining forward models by multi-physical data integration

Our research limits the degrees of freedom of forward modeling by constraining models with multi-physical data integration. Previous largely offshore seismic refraction surveys done in the region (e.g. Breivik et al. (2005); Ritzmann et al. (2002)) used gravity data for iteratively improving their density profile. The preliminary density model was obtained by converting the seismic velocity model based on tomography data to a density model by using general velocity-density relationships such as Christensen & Mooney (1995). This method of obtaining information about the density structure introduces uncertainties in regards of the velocity-density relationship. Additionally, Svalbard is often located at the outer edge of these models, where limited ray coverage reduces the resolution (Ritzmann et al., 2002, 2004; Ljones et al., 2004). These limitations should be taken into consideration when analyzing the resulting velocity and density values.

Our study therefore took a different approach by prioritizing the available subsurface data in terms of seismic lines and boreholes as initial modeling constraints. As the aeromagnetic field data were not located along these seismic lines, a consequence of this approach was that we were dependent on sampling the interpolated regional grids. We recognize that this limits the precision and short wavelength trends of the data, but we favor the solid geometry foundation provided by locating the models along seismic lines in this study.

6.4 Geological implications from forward models

By placing the main findings of the forward modeling into the broader context of regional geology, it was possible to integrate these observations to further enhance our understanding of the regional geological evolution. The different features will be discussed ordered by their impact on the resulting forward models.

6.4.1 Basement configuration

Only the two southern models were able to fit the magnetic data based on a homogeneous basement. The Isfjorden anomaly, thought to originate from a local magmatic body, dominates the magnetic signal and masks smaller contrasts resulting from the basement topography or heterogeneity. It would have been possible to introduce susceptibility heterogeneities in the basement to remove the remaining misfit. However, we aimed to keep the basement configuration laterally continuous between the models. Subsequently, as the southern models did not support substantial changes in basement susceptibility, large misfits in the magnetic data remained on the other 3 profiles. In previous research, Skilbrei (1992) argued for the need of intra-basement susceptibility contrasts east of the BFZ to explain the magnetic data trend. They studied a profile crossing the fault zone in Billefjorden, with limited impact of the Isfjorden anomaly. As the models studied in this research were either impacted by the anomaly or only covered a small portion of the BFZ, it was not possible to distinguish this signal on our profiles.

After the input of the overlaying lithostratigraphic units and subsurface geometry, most of the forward models were able to obtain a good fit to the gravity data based on a homogeneous basement. Profile 2, 7 and RS did not require changes in density to match the gravity data. Profile 5 and RN required slightly elevated density values east of the BFZ to match the gravity data. The increase in density east of the BFZ matches with the lithology of the Atomfjella Complex, a more metamorphosed and denser terrane. Matching the data did require introducing an elevated basement with a thinner Devonian basin to explain the gravity trends. An alternative scenario would be a locally denser basement body underlying the less dense Devonian basin which compensates for the reduced mass and therefore masks the gravity signal. Previous offshore studies in the southeast of Svalbard concluded that density variations in the basement were necessary to explain the gravity anomalies (Breivik et al., 2002, 2003). Similar density contrasts were found for the Storfjorden region (Breivik et al., 2005).

The gravity trend can therefore be explained by either elevating the basement or increasing the density. This study faced some uncertainty regarding the most suitable basement density. The currently selected values had the best match to the data but were on the high range of the values previously described (Krasil'ščikov et al., 1995; Breivik et al., 2005). Further fine tuning of the basement density values would be interesting in future studies, but we do not expect them to yield significantly different modeling results.

There is no consensus on the exact configuration of the basement of Svalbard and its difference in tectonometamorphic origins has been questioned (Gasser, 2014). This study finds that most of the observed potential field trends can be explained without adding basement heterogeneities by elevating the basement and introducing local magmatic bodies. While this does not debunk the presence of potential basement heterogeneities, we do observe that they have a minimal effect on the observed potential field data or might be masked by other processes.

6.4.2 Igneous intrusions

Regional studies showed that the Isfjorden magnetic anomaly did not have a gravitational counterpart, had a deep source and its shape did not match with the general N-S trend of the basement terranes. This argued for the inclusion of magmatic bodies. The forward models overlaying this anomaly were not able to match the magnetic trend based on the basement topography and larger magmatic bodies included in Profile RN improved the fit. This was necessary as it was not possible to match the positive magnetic anomaly based solely on the magnetic signature of the identified subsurface igneous sills. This matches the results from Minakov et al. (2012) southeast of Svalbard. They used a similar method of forward modeling and were not able to match the magnetic data based solely on the inclusion of sills, even when applying extremely high susceptibility values of 0.15 SI (Hunt et al., 1995). Based on observations of seismic reflectors being truncated by vertical discontinuities linked to magnetic anomalies, they interpreted mafic feeder dykes in their model to explain the magnetic signal. They argue for lateral propagation of magma away from a hotspot in the Amerasia Basin along previous zone of weakness of the Paleozoic rift as the source for this magma.

Such a correlation between magnetic anomalies and a Paleozoic rift system was also described in Grogan et al. (2000) southeast of Svalbard. They concluded that the controlling faults of the system functioned as a pathway for the upwelling of magma along this zone of weakness. Subsequently, high frequency magnetic anomalies in the northwestern Barents Sea were also linked to intra-sedimentary magmatic intrusions (Marello et al., 2013).

Therefore, the inclusion of another magmatic body in the subsurface coincides with previous observations in the region. Based on the shape and identified stronger seismic reflectors, we favor the scenario of a deeper and larger magmatic body in the subsurface to explain the Isfjorden anomaly. However, due to the long wavelength of the magnetic signal and the inherent ambiguity of depth and shape determination of potential field anomalies (Skeels, 1947), we cannot exclude the presence of a similar feeder dyke. Based on the Cretaceous age of the outcropping Diabasodden Suite, we favor linking the magmatic body to the HALIP as an explanation for its presence. However, there is no consensus on the emplacement mechanism of the HALIP (Senger & Galland, 2022). Limited age data and a complex tectonic setting make this ambiguous.

Integrating observations from other geophysical studies puts the presence of a magmatic body into further geophysical context. A mid crustal conductor (MCC) at a depth of approximately five kilometers was derived from a magnetotelluric (MT) profile collected in Adventdalen (Beka et al., 2016). They linked it to a potential Devonian basin infill, at the location where we suggest the presence of a larger magmatic body. While in general igneous intrusions are more resistive than the host rocks, if they are emplaced in organic-rich shales the intrusions have highly conductive aureoles due to pyritization and graphitization (Spacapan et al., 2020). Similarly, previous studies have linked conductive bodies derived from MT data offshore Norway to igneous systems with abundant mineralization (Corseri et al., 2017). This supports that a larger magmatic body could be responsible for the observed MCC if a similar mineralization system is present. Additionally, Senger et al. (2023) found a higher interpolated subsurface temperature below Isfjorden, and a faster Lower Crustal Body (LCB) was described (Krysiński et al., 2013) between the BFZ and HFC. These are observations which would potentially support the presence of a larger magmatic body. However, only shallow temperature data (1-2 km) was available and more heat flow modeling is necessary to understand the lateral heterogeneity of the thermal regime. Therefore, further analysis of the spatial correlation and its subsequent implications on a geometric model would be necessary to investigate the link between the different geophysical elements.

To properly analyze the different scenarios, we investigated whether the Devonian basin could be responsible for the observed magnetic signal. Hydrothermal alteration of rocks can cause increased magnetization in sedimentary formations (Airo, 2002). On average sedimentary rocks have a susceptibility between 0-0.00036 SI with the range of sandstone being between 0-0.021 SI (Telford et al., 1990). A Devonian basin susceptibility of 0.018 SI was necessary to obtain a good fit, based on the subsurface structure as interpreted according to the Bælum & Braathen (2012) scenario found in Appendix D. While this falls in the range of sandstone rocks, it is unrealistic for an entire basin to have such high

susceptibilities. Additionally, the southward extent of the Devonian basin continues beyond the Isfjorden anomaly. This makes it unlikely that the Devonian basin is responsible for the observed magnetic anomalies and again supports the scenario of a larger magmatic body in the subsurface.

6.4.3 Fault zones

Billefjorden Fault Zone

The regional trends as well as the forward models showed a good fit between the BFZ geometry and a high in gravity and magnetic data. The magnitude of the gravity anomaly reduces southward, linked to the deeper placement of the top of metamorphic basement bounded by the BFZ in the south.

Breivik et al. (2005) argue that the western Ny Friesland terrane along the BFZ continues southwards and is responsible for the offshore gravity anomaly in Storfjorden. While the gravity anomaly is a lot lower, they contribute a lowered gravity signal to the presence of a small basin. A similar continuation was interpreted in Skilbrei (1992) based on the aeromagnetic data.

However, there remain some open questions about this correlation. Onshore Svalbard, the signal from the Ny Friesland terrane diminishes around Van Mijenfjorden, about 60 kilometer north. The signal only becomes prominently visible again in Storfjorden. It could be that the change in signal is due to the onshore/offshore correlation. However, one might expect more sedimentation in the offshore region and therefore a stronger muting of the potential field signal. An alternative solution would therefore be that the stronger anomalies are again due to local magmatic bodies intruding along a Paleozoic fault zone, as described before in Minakov et al. (2012).

Lomfjorden Fault Zone

The scope of the current research focused on the potential field signature of the BFZ. Profile 3 and the eastern extent of Profile 2 of the SvalGrav surveys also cross the LFZ, another major N-S oriented tectonic lineament. Previous research suggested that the LFZ was responsible for a significant kink in the gravity data (Rylander & Sterley, 2022). However, upon further investigation in the current research, we found that this discontinuation was due to incorrect plotting of the data points sequence and no kink was present in the data. The LFZ does not have an equally expressive signature in the potential field data as the BFZ and would require further investigation for identifying its potential field signature.

6.4.4 Sedimentary basins

Central Spitsbergen Basin

The recent phase of compressing resulting in the formation of the WSFTB and the CSB has a strong link with the large negative gravity anomaly observed in the area. The thicker sediments in the foreland basin led to a deeper placement of the denser rock, therefore lowering the gravity signal. A combination of the thicker sedimentary package together with the elevation of basement along the BFZ explain the gravity anomalies on our profiles.

Devonian

Our models had the best fit to the observed data when the basement topography was slightly elevated when compared to previous interpretations. This would mean that the Devonian basin would have been thinner than previously interpreted, therefore having less accommodation space and a smaller volume of deposited sediments. However, there are other scenarios which would explain the potential field observations. As mentioned before, it could be that the basin is as thick as previously interpreted but a higher density basement underlying it compensates for this mass deficiency. Another scenario is that the actual density contrasts between the basement and Devonian rocks are lower than modeled, needing less change in elevation. Due to the strong influence of the Isfjorden anomaly on the magnetic data, these were less suitable for analyzing these scenarios.

Therefore, our research suggests the Devonian basin is thinner than originally interpreted but the depth of the Devonian basin could not be well constrained based on the available data and some uncertainty remains. This provides limited increased insights into the suitability of the subsurface of Longyearbyen for geothermal applications. Especially the potential of the ultra-deep (five km) enhanced geothermal systems remains insecure and more investigation would be necessary.

We also identified a laterally continuous sedimentary basin truncated by the Top Devonian reflector in the seismic interpretations. Its N-S continuation can be seen in Figure 6.3, combined with its stratigraphic

position this suggests it belongs to a smaller Devonian foreland basin. It can potentially be linked to the Mimerdalen Subgroup outcropping around Pyramiden, which has formed during the Svalbardian phase and was filled with sediments coming from the erosion of the eastward located uplifted Ny-Friesland fault block (Piepjohn & Dallmann, 2014). This is a changed provenance when compared to the older Andrée Group deposits sourcing westwards (Anfinson et al., 2022). However, further investigation of this foreland basin origin and geological implications are necessary.

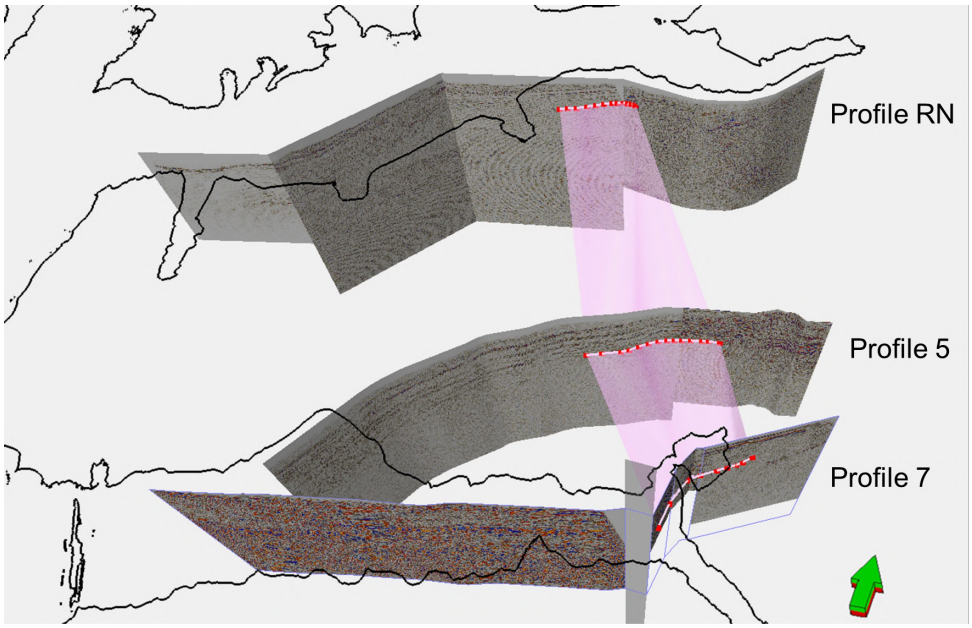

Figure 6.3: 3D view and correlation of the sedimentary wedge as identified on the seismic lines of Profiles RN, 5 and 7. It is thought to be a Devonian Foreland basin linked to the Mimerdalen Subgroup outcropping further north.

6.4.5 No Name Fault

The east dipping fault identified on the western side of the BFZ, named the No Name Fault in this study (NNF), has not been well described before. In Bergh & Grogan (2003) they include a similar feature in a cross sections based on the interpretations in (Bergh et al., 1997). They explain it as a result of basement involved thrust uplifting of Eocene age and linked to transpression in western Spitsbergen (Haremo & Andresen, 1992). Based on this interpretation, the age of the fault is approximately 40 Ma, not matching with the suspected age of intrusions of the Cretaceous HALIP.

Following the northward trend of the fault, an alternative explanation would be to link it to the Triungen Fault Zone outcropping in the Devonian Andrée land (Dallmann, 2015). This fault zone has been attributed to the Svalbardian contractional phase of deformation later reactivated during the mid-Carboniferous extension. Interestingly, outcropping Seidfjellet basalts were identified on the proximity of the fault zone (Dallmann, 2015). These basalts are of Cenozoic age but the dating of them has been inconclusive (Senger et al., 2014). The Seidfjellet formation is linked to a hotspot on the Yermak Plateau. Lateral magma transport would have been necessary to emplace the basalts. The role of the Triungen Fault Zone is unclear in the emplacement of the volcanics and further investigation into the signature and lateral continuation would be necessary to evaluate whether this fault zone could have functioned as a pathway for magmatic bodies.

This is relevant as the trend of the NNF seems to coincide with the eastern extent of the Isfjorden magnetic anomaly, see Figure 6.4, suggesting it could have functioned as a potential pathway for the magmatic body. If the Triungen Fault Zone played a role in the emplacement of the Seidfjellet basalts, it suggests it might have been a persistent zone of weakness through time. We identified the NNF on the Profile RN and 5, located in Isfjorden and Reindalen respectively. At the expected location of its southward continuation on profile 7, the seismic data is of low resolution and semi-parallel orientated with the strike of the fault. This does not allow us to conclude whether the fault is absent or not imaged. The scenario where the fault is absent supports the NNF being a potential pathway for the magmatic body, as the magnetic anomaly reduces in a similar location. However, more extensive research mapping of the surrounding seismic data would be necessary to further support this claim.

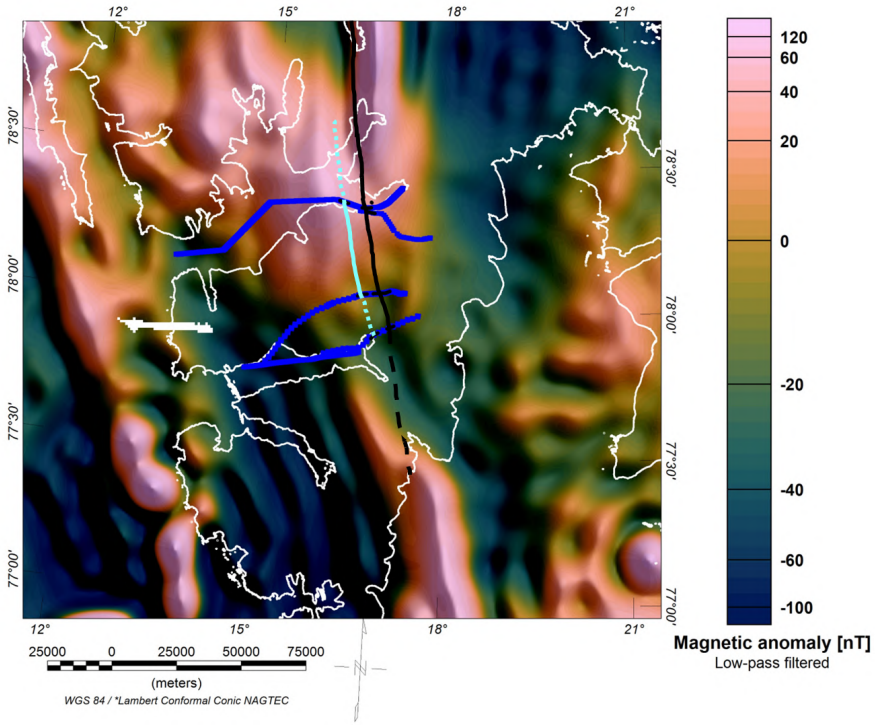

Figure 6.4: Low-pass filtered magnetic data with the data profiles of the forward modeling (dark blue), the mapped NNF (light blue) and the BFZ. The location is based on the interpretations of the seismic lines. The northward and southward extent of the NNF is not well defined but the location seems to match with the outer edge of the Isfjorden anomaly.

6.5 Limitations and uncertainty of the forward models

As with all forward models, due to the non-uniqueness of the solutions, it was essential to use appropriate boundary conditions for ensuring the models fit the observed data within the constraints of the geological framework. The current research faced several limitations, both in regards of the data integration and the modeling.

Data limitations

Our results showed that a lot of the potential field anomalies are thought to be due to basement configuration. It is however at this basement depth that the quantity and quality of the available data is limited. The seismic lines have a lower signal to noise ratio at depth, in addition to multiples or edge effects distorting the actual reflectors making interpretation more ambiguous. Borehole logs mostly cover the Cenozoic, Mesozoic and Upper Paleozoic lithostratigraphic units, with no physical parameters retrieved for the Devonian basin or basement. Additionally, limited data is available from hand samples which would allow further constraints on the input parameters. While this has introduced some uncertainties in our model, we believe we have obtained sufficient constraints from tomographic studies and average densities from literature. Another uncertainty in the model was located deeper down at the Moho transition. We included a uniform Moho at 30 kilometers in the models, as there was insufficient high-resolution data to base depth fluctuations on. However, Svalbard is located in a complex tectonic setting affected by the opening of both the North Atlantic and Arctic oceans, and it could be that this had some local effect on the Moho depth and therefore the potential field data.

As only long wavelength magnetic data was available as input for forward modeling, the resolution of the resolvable magnetic subsurface sources was limited. High resolution SvalMag data would have allowed imaging of shorter wavelength anomalies, which helps with distinguishing the source depth. Profile RN and RS also used regional data for the gravity input. On the other profiles, SvalGrav data without terrain correction was used. As both Profile 2 and 7 showed irregularities in the computed terrain correction and as the selected models were in areas with consistent and moderate topography, the impact on the data trends is limited. A recomputed terrain correction on a more accurate and ice-free topography DEM would further improve the data quality but was beyond the temporal and computational scope of this study.

Modeling limitations

Next to the data input, the modeling method had some limitations as well. First, projection of the data profile onto the 2D dimensional model line complicates direct comparison between the seismic cross sections and the created forward models. The more sinuous the profile, the larger the difference in distance and therefore the larger the distortion. As it is not possible to use a velocity-with-depth profile as input in the software, seismic velocities were assigned to individual model blocks. While this allowed a uniform velocity configuration between the models, the simplification adds uncertainty into the model. The high density of the compacted sediments on Svalbard adds another complicating factor for the forward gravity modeling. The upper sedimentary layers are within the range of 2500-2700 kg/m^3, while siliciclastic rocks have a typical density of around 2350-2400 kg/m3 (Telford et al., 1990). The compacted sediments therefore have a smaller density contrast with the basement rock, making it more difficult to distinguish signal from changes in subsurface composition.

After creating the individual forward models, we determined the absolute DC shift (see Section 4.3.5) to compare the magnitude of the computed anomalies across the models. Values in a similar range were found for the gravity data, however the magnetic DC shift showed large discrepancies between the models. It was positive in the north and became increasingly negative to the south. This was found to be due to the orientation of the anomalies with respect to the model orientation. The eastern increase of gravity anomalies is roughly parallel to the model orientations, a data trend orientation which the 2D perspective of the model can capture. However, the magnetic anomaly data peaks in the north of the study area and has a southern decrease, orthogonal to the model orientations. The 2D models are not able to capture this effect of the 3D feature in the data. As every peak coincides with a trough, adjusting the DC shift is necessary to compensate for this effect and allow the comparison between the computed and field data. This limited our ability to cross check models based on the magnetic data and highlights the limitations of using 2D profiles to explain 3D features. However, the match in gravity data does show a first-order consistency between the models.

6.6 Future research opportunities

Advanced modeling techniques

The scope of our study was limited to 2D forward modeling of gravity and magnetic data. Expanding the modeling dimensions and techniques would further enhance obtained insight from the available geophysical data. For a start, creating 2.5D models allows the incorporation of the 3D effect of regional anomalies. Further complexity can be added by performing 2.75D (allowing intersection of elements with non-perpendicular angles) inversion based on seismic, magnetic and gravity data, which has previously been used to identify subsurface saucer-shaped sills (Rocchi et al., 2007).

Using 3D inversion algorithms for both gravity (Li & Oldenburg, 1998) and magnetic data (Li & Oldenburg, 1996) allows the imaging of subsurface density and susceptibility contrasts in a more spatial domain. Joint interpretation of the resulting subsurface features, such as done in Moghaddam et al. (2016) for studying geothermal potential, would further enhance our understanding of the subsurface.

Expanding on the previous method comparing individual results of inversions, joint inversion of geophysical data limits the amount of non-unique solutions by putting multiple parameters into one inversion scheme and optimizing towards a solution fitting all data (Vozoff & Jupp, 1975). While this requires input regarding the coupling of the different parameters, choosing a cross-gradient approach which analyzes structural similarity between models would limit the dependency on input of parameter relationships. Previous studies have used this for making three dimensional joint inversions based on MT, gravity, and seismic refraction data (Moorkamp et al., 2011). Continuous developments in the field recently led to the proposal of a joint multinary inversion method of gravity and magnetic data (Lin & Zhdanov, 2018).

These more advanced modeling approaches do require increased computational power. We therefore recommend to first analyze whether the available geophysical data is of high enough resolution to be able to resolve anomalies on an appropriate scale. A joint inversion between the two potential field data but also exploring incorporating other data such as seismic tomography and MT studies would then be recommended to provide further insight into the anomalous bodies in the subsurface of Svalbard.

7 Conclusion

In conclusion, we have been able to enhance the understanding of the subsurface geometry, density, and magnetic susceptibility structure of Svalbard through analysis of regional potential field trends, multi-physical data integration and forward modeling of five key profiles. This gave us insight into basement configuration, igneous intrusions and fault zone configuration.

Our elected method of making seismic interpretations, which formed the primary constraints of the forward modeling geometry of five key profiles, in combination with multi-physical data integration from borehole logs, hand samples and velocity models was unique for the region and allowed us to limit the degrees of freedom coinciding with forward modeling. High resolution gravity data collected in the SvalGrav survey allowed more detailed modeling of the onshore profiles.

Both the regional analysis and the forward modeling showed that the gravity and magnetic anomalies were largely dependent on the basement configuration and the overlying sedimentary packages have a limited effect. The BFZ had a clear signature in both the magnetic and gravity data, as it offsets metamorphic basement against the Devonian basin. While some density heterogeneity was necessary to match the gravity data, the interpretation of magnetic anomalies was more ambiguous. The basement signature was overshadowed on most profiles by a local magnetic high in Isfjorden which did not match the basement topography.

Based on the anomaly shape and depth estimation, in combination with observations of strong discontinuous seismic reflectors, igneous sills and outcropping igneous rock in the region of the anomaly, we favor the scenario where this anomaly is caused by a larger magmatic body in the subsurface. This is in agreement with previous results from offshore studies and we suggest the emplacement of the body to be linked to the HALIP. Further studies of a detailed spatial correlation and incorporating MT and heatflow data might provide further insight. The NNF matches with the eastern edge of the Isfjorden anomaly, hinting at its potential for having functioned as a magma pathway. However, more constraints would be necessary on the age and regional extent of the fault to expand on the feasibility of this hypothesis.

Due to some of the data limitations of our research, some open questions remain, especially regarding the depth of the Devonian basin. This restricts us in drawing conclusions for the feasibility of deep geothermal exploration around Longyearbyen. Future studies applying advanced modeling methods, such as joint 3D inversion of potential field data and potentially integration various other geophysical data sources, might be able to further advance the local energy system.

This work has illustrated the importance of data integration in areas with poor data coverage. By applying the appropriate geological framework, we were able to obtain geological implications from geophysical datasets, especially regarding large fault zones and tectono-magmatic elements. These are important for the comprehension of the tectonic evolution of the region. The work has also highlighted the complexity of constraining the subsurface of Svalbard, especially at depth. Many opportunities remain for further research enhancing our understanding of how the geological evolution of Svalbard might be deciphered by studying the potential field anomalies.

References

Ahlborn, M., & Stemmerik, L. (2015). Depositional evolution of the Upper Carboniferous – Lower Permian Wordiekammen carbonate platform, Nordfjorden High, central Spitsbergen, Arctic Norway. *Norwegian Journal of Geology*, *95*, 91-126. doi: https://doi.org/10.17850/njg95-1-03

Airo, M.-L. (2002). Aeromagnetic and aeroradiometric response to hydrothermal alteration. *Surveys in Geophysics*, *23*, 273–302.

Andersen, O. B., & Knudsen, P. (2009). DNSC08 mean sea surface and mean dynamic topography models. *Journal of Geophysical Research*, *114*, C11001. doi: https://doi.org/10.1029/2008JC005179

Anfinson, O. A., Odlum, M. L., Piepjohn, K., Poulaki, E. M., Shephard, G. E., Stockli, D. F., ... Pavlovskaia, E. A. (2022). Provenance Analysis of the Andrée Land Basin and Implications for the Paleogeography of Svalbard in the Devonian. *Tectonics*, *41*(11), e2021TC007103. doi: https://doi.org/10.1029/2021TC007103

Bælum, K., Johansen, T. A., Johnsen, H., Rød, K., Ole Ruud, B., & Braathen, A. (2012). Subsurface structures of the Longyearbyen CO 2 Lab study area in Central Spitsbergen (Arctic Norway), as mapped by reflection seismic data. *Norwegian Journal of Geology/Norsk Geologisk Forening*, *92*(4), 377-389.

Beka, T. I., Smirnov, M., Birkelund, Y., Senger, K., & Bergh, S. G. (2016). Analysis and 3D inversion of magnetotelluric crooked profile data from central Svalbard for geothermal application. *Tectonophysics*, *686*, 98-115. doi: https://doi.org/10.1016/j.tecto.2016.07.024

Bergh, S. G., Braathen, A., & Andresen, A. (1997). Interaction of basement-involved and thin-skinned tectonism in the Tertiary fold-thrust belt of central Spitsbergen, Svalbard. *AAPG Bulletin*, *81*(4), 637–661. doi: https://doi.org/10.1306/522B43F7-1727-11D7-8645000102C1865D

Bergh, S. G., & Grogan, P. (2003). Tertiary structure of the Sørkapp-Hornsund Region, South Spitsbergen, and implications for the offshore southern extension of the fold-thrust belt. *Norwegian Journal of Geology/Norsk Geologisk Forening*, *83*(1).

Bergh, S. G., Maher, H., & Braathen, A. (2011). Late Devonian transpressional tectonics in Spitsbergen, Svalbard, and implications for basement uplift of the Sørkapp–Hornsund High. *Journal of the Geological Society*, *168*, 441-456. doi: https://doi.org/10.1144/0016-76492010-046

Berglar, K., Franke, D., Lutz, R., Schreckenberger, B., & Damm, V. (2016). Initial Opening of the Eurasian Basin, Arctic Ocean. *Frontiers in Earth Science*, *4*(91). doi: https://doi.org/10.3389/feart.2016.00091

Blakely, R. J. (1995). *Potential theory in gravity and magnetic applications*. Cambridge University Press.

Blakely, R. J., Connard, G. G., & Curto, J. B. (2016). Tilt derivative made easy. *Geosoft Technical Publications*, *4*, 1–4.

Blomeier, D., Dustira, A. M., Forke, H., & Scheibner, C. (2013). Facies analysis and depositional environments of a storm-dominated, temperate to cold, mixed siliceous-carbonate ramp: the Permian Kapp Starostin Formation in NE Svalbard. *Norwegian Journal of Geology/Norsk Geologisk Forening*, *93*(2), 75-93.

Blomeier, D., Scheibner, C., & Forke, H. (2009). Facies arrangement and cyclostratigraphic architecture of a shallow-marine, warm-water carbonate platform: the Late Carboniferous Ny Friesland Platform in eastern Spitsbergen (Pyefjellet Beds, Wordiekammen Formation, Gipsdalen Group). *Facies*, *55*, 291-324. doi: https://doi.org/10.1007/s10347-008-0163-3

Bouligand, C., Glen, J. M. G., & Blakely, R. J. (2009). Mapping Curie temperature depth in the western United States with a fractal model for crustal magnetization. *Journal of Geophysical Research: Solid Earth*, *114*, B11104. doi: https://doi.org/10.1029/2009JB006494

Braathen, A., Bælum, K., Maher Jr, H., & Buckley, S. J. (2012). Growth of extensional faults and folds during deposition of an evaporite-dominated half-graben basin; the Carboniferous Billefjorden Trough, Svalbard. *Norwegian Journal of geology*, *91*(3), 137-160.

Braathen, A., Osmundsen, P. T., Maher, H., & Ganerød, M. (2018). The Keisarhjelmen detachment records Silurian–Devonian extensional collapse in northern Svalbard. *Terra Nova*, *30*, 34-39. doi: https://doi.org/10.1111/ter.12305

Breivik, A., & Faleide, J. I. (2004). *Geophysical Atlas of the Barents Sea, integrated seismic, gravity and magnetic interpretation* (Tech. Rep.). Oslo: Confidential VBPR and TGS-NOPEC Report.

Breivik, A. J., Mjelde, R., Grogan, P., Shimamura, H., Murai, Y., & Nishimura, Y. (2003). Crustal structure and transform margin development south of Svalbard based on ocean bottom seismometer data. *Tectonophysics*, *369*(1), 37-70. doi: https://doi.org/10.1016/S0040-1951(03)00131-8

Breivik, A. J., Mjelde, R., Grogan, P., Shimamura, H., Murai, Y., & Nishimura, Y. (2005). Caledonide development offshore–onshore Svalbard based on ocean bottom seismometer, conventional seismic, and potential field data. *Tectonophysics*, *401*(1), 79-117. doi: https://doi.org/10.1016/j.tecto.2005.03.009

Breivik, A. J., Mjelde, R., Grogan, P., Shimamura, H., Murai, Y., Nishimura, Y., & Kuwano, A. (2002). A possible Caledonide arm through the Barents Sea imaged by OBS data. *Tectonophysics*, *355*(1), 67-97. doi: https://doi.org/10.1016/S0040-1951(02)00135-X

Briggs, I. C. (1974). Machine contouring using minimum curvature. *GEOPHYSICS*, *39*, 39-48. doi: https://doi.org/10.1190/1.1440410

Bro, E. G. (1990a). Processing results from parametric drill hole Vassdalenskaya-2, Svalbard Archipelago, north side of Van-Meyen Fjord (Report 6593, Leningrad). *All-Russian Research Institute for Geology and Mineral Resources of the World Ocean, St. Petersburg, PANGAEA*. doi: https://doi.org/10.1594/PANGAEA.690356

Bro, E. G. (1990b). Processing results from parametric drill hole Vassdalenskaya-3, Svalbard Archipelago, north side of Van-Meyen Fjord (Report 6593, Leningrad) [data set]. *All-Russian Research Institute for Geology and Mineral Resources of the World Ocean, St. Petersburg, PANGAEA*. doi: https://doi.org/10.1594/PANGAEA.690357

Bælum, K., & Braathen, A. (2012). Along-strike changes in fault array and rift basin geometry of the Carboniferous Billefjorden Trough, Svalbard, Norway. *Tectonophysics*, *546-547*, 38-55. doi: https://doi.org/10.1016/j.tecto.2012.04.009

Bédard, J. H., Troll, V. R., Deegan, F. M., Tegner, C., Saumur, B. M., Evenchick, C. A., ... Dewing, K. (2021). High Arctic Large Igneous Province Alkaline Rocks in Canada: Evidence for Multiple Mantle Components. *Journal of Petrology*, *62*(9), egab042. doi: https://doi.org/10.1093/petrology/egab042

Christensen, N. I., & Mooney, W. D. (1995). Seismic velocity structure and composition of the continental crust: A global view. *Journal of Geophysical Research: Solid Earth*, *100*, 9761–9788.

Clark, S. A., Glorstad-Clark, E., Faleide, J. I., Schmid, D., Hartz, E. H., & Fjeldskaar, W. (2014). Southwest Barents Sea rift basin evolution: Comparing results from backstripping and time-forward modelling. *Basin Research*, *26*, 550-566. doi: https://doi.org/10.1111/bre.12039

Corseri, R., Senger, K., Selway, K., Abdelmalak, M. M., Planke, S., & Jerram, D. A. (2017). Magnetotelluric evidence for massive sulphide mineralization in intruded sediments of the outer Vøring Basin, mid-Norway. *Tectonophysics*, *706-707*, 196-205. doi: https://doi.org/https://doi.org/10.1016/j.tecto.2017.04.011

Crameri, F. (2018). Scientific Colour Maps. *Zenodo*, *10*. Retrieved from `http://www.fabiocrameri.ch/colourmaps`

Dallmann, W. K. (1992). Multiphase tectonic evolution of the Sørkapp-Hornsund mobile zone (Devonian, Carboniferous, Tertiary), Svalbard. *Norsk Geologisk Tidsskrift*, *72*(1), 49–66.

Dallmann, W. K. (2015). *Geoscience Atlas of Svalbard*. Norsk polarinstitutt. Retrieved from `https://digitalcommons.usf.edu/kip_articles/2176`

Dentith, M., & Mudge, S. T. (2014). *Geophysics for the mineral exploration geoscientist*. Cambridge University Press. doi: https://doi.org/10.1017/CBO9781139024358.

Dumais, M.-A. (2021). *Regional tectonic and environmental assessments of the Norwegian Polar regions using potential field methods* (Doctoral dissertation, NTNU). Retrieved from https://hdl.handle.net/11250/2977180

Dumais, M.-A., & Brönner, M. (2020). Revisiting Austfonna, Svalbard, with potential field methods–a new characterization of the bed topography and its physical properties. *The Cryosphere*, *14*, 183-197. doi: https://doi.org/10.5194/tc-14-183-2020

Dumais, M.-A., Gernigon, L., Olesen, O., Johansen, S. E., & Brönner, M. (2021). New interpretation of the spreading evolution of the Knipovich Ridge derived from aeromagnetic data. *Geophysical Journal International*, *224*, 1422-1428. doi: https://doi.org/10.1093/gji/ggaa527

Dumais, M.-A., Gernigon, L., Olesen, O., Lim, A., Johansen, S. E., & Brönner, M. (2022). Crustal and thermal heterogeneities across the Fram Strait and the Svalbard margin. *Tectonics*, *41*, e2022TC007302. doi: https://doi.org/10.1029/2022TC007302

Dumais, M.-A., Olesen, O., Gernigon, L., Brönner, M., Lim, A., & Johansen, S. (2020). Knipovich Ridge Aeromagnetic Survey 2016: processing and interpretation. *NGU-rapport 2020.030*.

Døssing, A., Jackson, H., Matzka, J., Einarsson, I., Rasmussen, T., Olesen, A., & Brozena, J. (2013). On the origin of the Amerasia Basin and the High Arctic Large Igneous Province - Results of new aeromagnetic data. *Earth and Planetary Science Letters*, *363*, 219-230. doi: https://doi.org/10.1016/j.epsl.2012.12.013

Egging, R., & Tomasgard, A. (2018). Norway's role in the European energy transition. *Energy Strategy Reviews*, *20*, 99-101. doi: https://doi.org/10.1016/j.esr.2018.02.004

Fairhead, J. D., & Odegard, M. E. (2002). Advances in gravity survey resolution. *The Leading Edge*, *21*(1), 36-37. doi: https://doi.org/10.1190/1.1445845

Faleide, J. I., Bjørlykke, K., & Gabrielsen, R. H. (2015). Geology of the Norwegian continental shelf. *Petroleum geoscience*, 603–637.

Ferguson, J. F., Chen, T., Brady, J., Aiken, C. L., & Seibert, J. (2007). The 4D microgravity method for waterflood surveillance: Part II — Gravity measurements for the Prudhoe Bay reservoir, Alaska. *GEOPHYSICS*, *72*, I33-I43. doi: https://doi.org/10.1190/1.2435473

Friend, P., Heintz, N., & Moody-Stuart, M. (1966). New unit terms for the Devonian of Spitsbergen and a new stratigraphical scheme for the Wood Bay Formation. *Norsk Polarinstitutt Årbok*, *1965*, 59–64.

Fürst, J. J., Navarro, F., Gillet-Chaulet, F., Huss, M., Moholdt, G., Fettweis, X., ... Braun, M. H. (2018). The ice-free topography of Svalbard. *Geophysical Research Letters*, *45*, 11,760-11,769. doi: https://doi.org/10.1029/2018GL079734

Gasser, D. (2014). The Caledonides of Greenland, Svalbard and other Arctic areas: status of research and open questions. *Geological Society, London, Special Publications*, *390*(1), 93-129. doi: https://doi.org/10.1144/SP390.17

Gasser, D., & Andresen, A. (2013). Caledonian terrane amalgamation of Svalbard: Detrital zircon provenance of Mesoproterozoic to Carboniferous strata from Oscar II Land, western Spitsbergen. *Geological Magazine*, *150*, 1103-1126. doi: https://doi.org/10.1017/S0016756813000174

Gee, D. G., & Teben'kov, A. M. (2004). Svalbard: a fragment of the Laurentian margin. *Geological Society, London, Memoirs*, *30*, 191-206. doi: https://doi.org/10.1144/GSL.MEM.2004.030.01.16

Geosoft. (2006). *GM-SYS profile modeling. gravity and magnetic modeling software.* Geosoft Incorporated.

Geosoft. (2010). *Geophysics levelling system - processing and enhancing geophysical data extension for Oasis montaj v7.1 - Tutorial and user guide.* Geosoft Incorporated. (70pp.)

Gjelberg, J., & Steel, R. (1981). An outline of Lower-Middle Carboniferous sedimentation on Svalbard: Effects of tectonic, climatic and sea level changes in rift basin sequences. In *Geology of the North Atlantic Borderlands* (Vol. 7, p. 543-561). CSPG Special Publications.

Glicken, M. (1962). Eötvös corrections for a moving gravity meter. *GEOPHYSICS*, *27*(4), 531–533.

Grad, M., & Majorowicz, J. (2020). Geophysical properties of the crust and upper mantle of the ocean-continent transition in Svalbard area. *Polish Polar Research*, *41*(1), 1–22. doi: https://doi.org/10.24425/ppr.2020.132567

Green, P. F., & Duddy, I. R. (2010). Synchronous exhumation events around the Arctic including examples from Barents sea and Alaska North Slope. *Geological Society, London, Petroleum Geology Conference Series*, *7*, 633-644. doi: https://doi.org/10.1144/0070633

Grogan, P., Nyberg, K., Fotland, B., Myklebust, R., Dahlgren, S., & Riis, F. (2000). Cretaceous magmatism south and east of Svalbard: evidence from seismic reflection and magnetic data. *Polarforschung*, *68*, 25–34.

Haremo, P., & Andresen, A. (1992). Tertiary décollement thrusting and inversion structures along Billefjorden and Lomfjorden Fault Zones, east central Spitsbergen. In *Structural and tectonic modelling and its application to petroleum geology* (pp. 481–494). Norwegian Petroleum Society, Special Publication.

Harland, W. B. (1997). *The Geology of Svalbard* (No. 17). Geological Society, London. doi: https://doi.org/10.1144/GSL.MEM.1997.017.01.26

Harland, W. B., Scott, R. A., Auckland, K. A., & Snape, I. (1992). The Ny Friesland Orogen, Spitsbergen. *Geological Magazine*, *129*, 679-707. doi: https://doi.org/10.1017/S0016756800008438

Helland-Hansen, W., & Grundvåg, S. (2021). The Svalbard Eocene-Oligocene (?) Central Basin succession: Sedimentation patterns and controls. *Basin Research*, *33*, 729-753. doi: https://doi.org/10.1111/bre.12492

Hjelle, A. (1966). The composition of some granitic rocks from Svalbard. *Norsk Polarinstitutt Årbok*, *1965*, 7–30.

Horisont Energi. (n.d.). *Polaris*. `https://horisontenergi.no/projects/polaris/`. (Accessed 31/10/2023)

Hunt, C. P., Moskowitz, B. M., Banerjee, S. K., & Ahrens, T. (1995). Rock physics and phase relations: a handbook of physical constants. *AGU reference shelf*, *3*, 189–204.

Huss, M. (2013). Density assumptions for converting geodetic glacier volume change to mass change. *The Cryosphere*, *7*(3), 877–887.

Hübscher, C., & Gohl, K. (2014). *Reflection/refraction seismology*. Encyclopedia of Marine Geosciences, Springer. doi: https://doi.org/10.1007/978-94-007-6644-0_128-1

Ineson, J. R., Hovikoski, J., Sheldon, E., Piasecki, S., Alsen, P., Fyhn, M. B. W., ... Bojesen-Koefoed, J. A. (2021). Regional impact of Early Cretaceous tectono-magmatic uplift in the Arctic: Implications of new data from eastern North Greenland. *Terra Nova*, *33*, 284-292. doi: https://doi.org/10.1111/ter.12514

Jacobsen, B. H. (1987). A case for upward continuation as a standard separation filter for potential-field maps. *GEOPHYSICS*, *52*, 1138-1148. doi: https://doi.org/10.1190/1.1442378

Jafarian, E., Kleipool, L., Scheibner, C., Blomeier, D., & Reijmer, J. (2017). Variations in petrophysical properties of upper Palaeozoic mixed carbonate and non-carbonate deposits, Spitsbergen, Svalbard archipelago. *Journal of Petroleum Geology*, *40*, 59-83. doi: https://doi.org/10.1111/jpg.12664

Jakobsson, K. H. (2018). A history of exploration offshore Norway: the Barents Sea. *Geological Society, London, Special Publications*, *465*(1), 219-241. doi: https://doi.org/10.1144/SP465.18

Johansen, T., Ruud, B., Bakke, N., Riste, P., Johannessen, E., & Henningsen, T. (2011). Seismic profiling on Arctic glaciers. *First Break*, *29*. doi: https://doi.org/10.3997/1365-2397.20112st1

Johansen, T. A., Digranes, P., van Schaack, M., & Lønne, I. (2003). Seismic mapping and modeling of near-surface sediments in polar areas. *GEOPHYSICS*, *68*, 566-573. doi: https://doi.org/10.1190/1.1567226

Johansen, T. A., Ruud, B. O., & Hope, G. (2019). Seismic on floating ice on shallow water: Observations and modeling of guided wave modes. *GEOPHYSICS*, *84*(2), P1-P13. doi: https://doi.org/10.1190/geo2018-0211.1

Johansson, A., Gee, D. G., Larionov, A. N., Ohta, Y., & Tebenkov, A. M. (2005). Grenvillian and Caledonian evolution of eastern Svalbard–a tale of two orogenies. *Terra Nova*, *17*, 317-325. doi: https://doi.org/10.1111/j.1365-3121.2005.00616.x

Jokat, W., Geissler, W., & Voss, M. (2008). Basement structure of the north-western Yermak Plateau. *Geophysical Research Letters*, *35*, L05309. doi: https://doi.org/10.1029/2007GL032892

Jokat, W., Lehmann, P., Damaske, D., & Nelson, J. B. (2016). Magnetic signature of North-East Greenland, the Morris Jesup Rise, the Yermak Plateau, the central Fram strait: constraints for the rift/drift history between Greenland and Svalbard since the Eocene. *Tectonophysics*, *691*, 98-109. doi: https://doi.org/10.1016/j.tecto.2015.12.002

Klausen, T. G., Nyberg, B., & Helland-Hansen, W. (2019). The largest delta plain in Earth's history. *Geology*, *47*, 470-474. doi: https://doi.org/10.1130/G45507.1

Krasil'ščikov, A., Kubanskij, A., & Ohta, Y. (1995). Surface magnetic anomaly study on the eastern part of the Forlandsundet Graben. *Polar Research*, *14*, 55-68. doi: https://doi.org/10.1111/j.1751-8369.1995.tb00710.x

Krysiński, L., Grad, M., Mjelde, R., Czuba, W., & Guterch, A. (2013). Seismic and density structure of the lithosphere- asthenosphere system along transect Knipovich Ridge- Spitsbergen-Barents Sea–geological and petrophysical implications. *Polish Polar Research*(2), 111–138. doi: https://doi.org/10.2478/popore-2013-0011

Kurinin, R. (1965). Density and magnetic susceptibility of Spitsbergen rocks. *Geological material of Spitsbergen (in Russian)*, 276–285.

Lacoste, L. J. B. (1967). Measurement of gravity at sea and in the air. *Reviews of Geophysics*, *5*, 477-526. doi: https://doi.org/10.1029/RG005i004p00477

Lacoste-Romberg. (2004). Instruction Manual Models G & D Gravity Meters [Computer software manual]. (127 pp.)

Lasabuda, A. P., Johansen, N. S., Laberg, J. S., Faleide, J. I., Senger, K., Rydningen, T. A., ... Hanssen, A. (2021). Cenozoic uplift and erosion of the Norwegian Barents Shelf–A review. *Earth-Science Reviews*, *217*, 103609. doi: https://doi.org/10.1016/j.earscirev.2021.103609

Lepvrier, C. (2000). Drift of Greenland and correlation of Tertiary tectonic events in the West Spitsbergen and Eurekan fold thrust belt. *Polarforschung*, *68*, 93-100.

Li, X., & Götze, H. (2001). Ellipsoid, geoid, gravity, geodesy, and geophysics. *GEOPHYSICS*, *66*, 1660-1668. doi: https://doi.org/10.1190/1.1487109

Li, Y., & Oldenburg, D. W. (1996). 3-D inversion of magnetic data. *GEOPHYSICS*, *61*, 394-408. doi: https://doi.org/10.1190/1.1443968

Li, Y., & Oldenburg, D. W. (1998). 3-D inversion of gravity data. *GEOPHYSICS*, *63*, 109-119. doi: https://doi.org/10.1190/1.1444302

Lin, W., & Zhdanov, M. S. (2018). Joint multinary inversion of gravity and magnetic data using Gramian constraints. *Geophysical Journal International*, *215*(3), 1540-1557. doi: https://doi.org/10.1093/gji/ggy351

Ljones, F., Kuwano, A., Mjelde, R., Breivik, A., Shimamura, H., Murai, Y., & Nishimura, Y. (2004). Crustal transect from the North Atlantic Knipovich Ridge to the Svalbard Margin west of Hornsund. *Tectonophysics*, *378*(1), 17-41. doi: https://doi.org/10.1016/j.tecto.2003.10.003

Long, L. T., & Kaufmann, R. D. (2013). *Acquisition and analysis of terrestrial gravity data*. Cambridge University Press. doi: https://doi.org/10.1017/CBO9781139162289

Lund, J. W., Bjelm, L., Bloomquist, G., & Mortensen, A. K. (2008). Characteristics, development and utilization of geothermal resources – a Nordic perspective. *Episodes*, *31*, 140-147. doi: https://doi.org/10.18814/epiiugs/2008/v31i1/019

Lyberis, N., & Manby, G. (1999). Continental collision and lateral escape deformation in the lower and upper crust: an example from Caledonide Svalbard. *Tectonics*, *18*, 40-63. doi: https://doi.org/10.1029/1998TC900013

Maher, H. D. (2001). Manifestations of the Cretaceous High Arctic large igneous province in Svalbard. *The Journal of Geology*, *109*, 91-104. doi: https://doi.org/10.1086/317960

Marello, L., Ebbing, J., & Gernigon, L. (2013). Basement inhomogeneities and crustal setting in the Barents sea from a combined 3D gravity and magnetic model. *Geophysical Journal International*, *193*, 557-584. doi: https://doi.org/10.1093/gji/ggt018

Mather, B., & Delhaye, R. (2019). PyCurious: A Python module for computing the Curie depth from the magnetic anomaly. *Journal of Open Source Software*, *4*(39), 1544. doi: https://doi.org/10.21105/joss.01544

McCann, A. J. (2000). Deformation of the Old Red sandstone of NW Spitsbergen; links to the Ellesmerian and Caledonian orogenies. *Geological Society, London, Special Publications*, *180*, 567-584. doi: https://doi.org/10.1144/GSL.SP.2000.180.01.30

Miller, H. G., & Singh, V. (1994). Potential field tilt—a new concept for location of potential field sources. *Journal of Applied Geophysics*, *32*, 213-217. doi: https://doi.org/10.1016/0926-9851(94)90022-1

Minakov, A., Mjelde, R., Faleide, J. I., Flueh, E. R., Dannowski, A., & Keers, H. (2012). Mafic intrusions east of Svalbard imaged by active-source seismic tomography. *Tectonophysics*, *518-521*, 106-118. doi: https://doi.org/10.1016/j.tecto.2011.11.015

Moghaddam, M. M., Mirzaei, S., Nouraliee, J., & Porkhial, S. (2016). Integrated magnetic and gravity surveys for geothermal exploration in Central Iran. *Arabian Journal of Geosciences*, *9*(506). doi: https://doi.org/10.1007/s12517-016-2539-y

Moorkamp, M., Heincke, B., Jegen, M., Roberts, A. W., & Hobbs, R. W. (2011). A framework for 3-D joint inversion of MT, gravity and seismic refraction data. *Geophysical Journal International*, *184*(1), 477-493. doi: https://doi.org/10.1111/j.1365-246X.2010.04856.x

Morelli, C., Gantar, C., McConnell, R., Szabo, B., & Uotila, U. (1972). *The international gravity standardization net 1971 (IGSN 71)* (Tech. Rep.). Osservatorio Geofisico Sperimentale Trieste (Italy). Retrieved from `https://apps.dtic.mil/sti/citations/ADA006203`

Moritz, H. (1980). Geodetic reference system 1980. *Bulletin géodésique*, *54*(3), 395–405.

Müller, R., Klausen, T., Faleide, J., Olaussen, S., Eide, C., & Suslova, A. (2019). Linking regional unconformities in the Barents Sea to compression-induced forebulge uplift at the Triassic-Jurassic transition. *Tectonophysics*, *765*, 35-51. doi: https://doi.org/10.1016/j.tecto.2019.04.006

Nordenskiöld, A. E. (1867). *Sketch of the Geology of Spitsbergen.* Stockholm: Norstedt. (Original in Swedish: Utkast till Spetsbergens geologi. Published by the Royal Swedish Science Academy in 1866.)

Nuth, C., Kohler, J., König, M., von Deschwanden, A., Hagen, J. O., Kääb, A., ... Pettersson, R. (2013). Decadal changes from a multi-temporal glacier inventory of Svalbard. *The Cryosphere*, *7*, 1603–1621. doi: https://doi.org/10.5194/tc-7-1603-2013

Olaussen, S., Grundvåg, S.-A., Senger, K., Anell, I., Betlem, P., Birchall, T., ... Stemmerik, L. (2023). Svalbard Composite Tectono-Sedimentary Element, Barents Sea. *Geological Society, London, Memoirs*, *57*(1), M57-2021-36. doi: https://doi.org/10.1144/M57-2021-36

Olesen, O., Brönner, M., Ebbing, J., Gellein, J., Gernigon, L., Koziel, J., ... Usov, S. (2010). New aeromagnetic and gravity compilations from Norway and adjacent areas: methods and applications. *Geological Society, London, Petroleum Geology Conference Series*, *7*, 559-586. doi: https://doi.org/10.1144/0070559

Piepjohn, K. (2000). The Svalbardian-Ellesmerian deformation of the old red sandstone and the pre-Devonian basement in NW Spitsbergen (Svalbard). *Geological Society, London, Special Publications*, *180*, 585-601. doi: https://doi.org/10.1144/GSL.SP.2000.180.01.31

Piepjohn, K., & Dallmann, W. K. (2014). Stratigraphy of the uppermost Old Red Sandstone of Svalbard (Mimerdalen Subgroup). *Polar Research*, *33*. doi: https://doi.org/10.3402/polar.v33.19998

Pirli, M., Schweitzer, J., & Paulsen, B. (2013). The Storfjorden, Svalbard, 2008–2012 aftershock sequence: Seismotectonics in a polar environment. *Tectonophysics*, *601*, 192-205. doi: https://doi.org/10.1016/j.tecto.2013.05.010

Ringrose, P. S. (2018). The CCS hub in Norway: some insights from 22 years of saline aquifer storage. *Energy Procedia*, *146*, 166-172. doi: https://doi.org/https://doi.org/10.1016/j.egypro.2018.07.021

Ritzmann, O., Jokat, W., Czuba, W., Guterch, A., Mjelde, R., & Nishimura, Y. (2004). A deep seismic transect from Hovgård ridge to northwestern Svalbard across the continental-ocean transition: A sheared margin study. *Geophysical Journal International*, *157*, 683-702. doi: https://doi.org/10.1111/j.1365-246X.2004.02204.x

Ritzmann, O., Jokat, W., Mjelde, R., & Shimamura, H. (2002). Crustal structure between the Knipovich Ridge and the Van Mijenfjorden (Svalbard). *Marine Geophysical Researches*, *23*, 379-401. doi: https://doi.org/10.1023/B:MARI.0000018168.89762.a4

Rocchi, S., Mazzotti, A., Marroni, M., Pandolfi, L., Costantini, P., Giuseppe, B., ... Lô, P. G. (2007). Detection of Miocene saucer-shaped sills (offshore Senegal) via integrated interpretation of seismic, magnetic and gravity data. *Terra Nova*, *19*, 232-239. doi: https://doi.org/10.1111/j.1365-3121.2007.00740.x

Rylander, S., & Sterley, A. (2022). *Integration of geology with geophysics: case studies from Svalbard* (Master's thesis, KTH Royal Institute of Technology). Retrieved from `https://www.diva-portal.org/smash/get/diva2:1708058/FULLTEXT01.pdf`

Salem, A., Williams, S., Fairhead, D., Smith, R., & Ravat, D. (2008). Interpretation of magnetic data using tilt-angle derivatives. *GEOPHYSICS*, *73*, L1-L10. doi: https://doi.org/10.1190/1.2799992

Schintgen, T. (2015). Exploration for deep geothermal reservoirs in Luxembourg and the surroundings - perspectives of geothermal energy use. *Geothermal Energy*, *3*(9). doi: https://doi.org/10.1186/s40517-015-0028-2

Schlumberger. (2022). *PETREL software.* Computer software. Author. (Version 2022.1)

Schober, P., Boer, C., & Schwarte, L. A. (2018). Correlation coefficients: appropriate use and interpretation. *Anesthesia & Analgesia*, *126*, 1763-1768. doi: https://doi.org/10.1213/ANE.0000000000002864

Seidler, L., Steel, R., Stemmerik, L., & Surlyk, F. (2004). North Atlantic marine rifting in the Early Triassic: new evidence from East Greenland. *Journal of the Geological Society*, *161*, 583-592. doi: https://doi.org/10.1144/0016-764903-063

Senger, K., Brugmans, P., Grundvåg, S.-A., Jochmann, M. M., Nøttvedt, A., Olaussen, S., ... Smyrak-Sikora, A. (2019). Petroleum, coal and research drilling onshore Svalbard: a historical perspective. *Norwegian Journal of Geology*, *99*(3), 377-407. doi: https://doi.org/10.17850/njg99-3-1

Senger, K., & Galland, O. (2022). Stratigraphic and Spatial extent of HALIP Magmatism in central Spitsbergen. *Geochemistry, Geophysics, Geosystems*, *23*, e2021GC010300. doi: https://doi.org/10.1029/2021GC010300

Senger, K., Nuus, M., Balling, N., Betlem, P., Birchall, T., Christiansen, H. H., ... Thomas, P. J. (2023). The subsurface thermal state of Svalbard and implications for geothermal potential. *Geothermics*, *111*, 102702. doi: https://doi.org/10.1016/j.geothermics.2023.102702

Senger, K., Tveranger, J., Braathen, A., Olaussen, S., Ogata, K., & Larsen, L. (2015). CO 2 storage resource estimates in unconventional reservoirs: insights from a pilot-sized storage site in Svalbard, Arctic Norway. *Environmental Earth Sciences*, *73*, 3987-4009. doi: https://doi.org/10.1007/s12665-014-3684-9

Senger, K., Tveranger, J., Ogata, K., Braathen, A., & Planke, S. (2014). Late Mesozoic magmatism in Svalbard: A review. *Earth-Science Reviews*, *139*, 123-144. doi: https://doi.org/10.1016/j.earscirev.2014.09.002

Simpson, R. W., Jachens, R. C., & Blakely, R. J. (1983). *AIRYROOT; a FORTRAN program for calculating the gravitational attraction of an Airy isostatic root out to 166.7 km* (Tech. Rep.). US Geological Survey. doi: https://doi.org/10.3133/ofr83883

Skeels, D. C. (1947). Ambiguity in gravity interpretation. *GEOPHYSICS*, *12*(1), 43-56. doi: https://doi.org/10.1190/1.1437295

Skilbrei, J. R. (1991). Interpretation of depth to the magnetic basement in the northern Barents Sea (south of Svalbard). *Tectonophysics*, *200*, 127-141. doi: https://doi.org/10.1016/0040-1951(91)90010-P

Skilbrei, J. R. (1992). Preliminary interpretation of aeromagnetic data from Spitsbergen, Svalbard Archipelago (76–79 N): Implications for structure of the basement. *Marine Geology*, *106*, 53-68. doi: https://doi.org/10.1016/0025-3227(92)90054-L

Smelror, M., & Larssen, G. B. (2016). Are there Upper Cretaceous sedimentary rocks preserved on Sørkapp land, Svalbard? *Norwegian Journal of Geology*, *96*(2), 147-158. doi: https://doi.org/10.17850/njg96-2-05

Smyrak-Sikora, A., Johannessen, E. P., Olaussen, S., Sandal, G., & Braathen, A. (2019). Sedimentary architecture during Carboniferous rift initiation–the arid Billefjorden Trough, Svalbard. *Journal of the Geological Society*, *176*, 225-252. doi: https://doi.org/10.1144/jgs2018-100

Smyrak-Sikora, A., Nicolaisen, J. B., Braathen, A., Johannessen, E. P., Olaussen, S., & Stemmerik, L. (2021). Impact of growth faults on mixed siliciclastic-carbonate-evaporite deposits during rift climax and reorganisation—Billefjorden Trough, Svalbard, Norway. *Basin Research*, *33*, 2643-2674. doi: https://doi.org/10.1111/bre.12578

Spacapan, J. B., D´Odorico, A., Palma, O., Galland, O., Senger, K., Ruiz, R., ... Leanza, H. A. (2020). Low resistivity zones at contacts of igneous intrusions emplaced in organic-rich formations and their implications on fluid flow and petroleum systems: A case study in the northern Neuquén Basin, Argentina. *Basin Research*, *32*(1), 3-24. doi: https://doi.org/https://doi.org/10.1111/bre.12363

Steel, R. J., Dalland, A., Kalgraff, K., & Larsen, V. (1981). The Central Tertiary Basin of Spitsbergen: Sedimentary Development of a Sheared-Margin Basin. In *Geology of the North Atlantic Borderland* (Vol. 7, p. 647–664). Canadian Society of Petroleum Geologists.

Steel, R. J., & Worsley, D. (1984). Svalbard's post-Caledonian strata — an atlas of sedimentational patterns and palaeogeographic evolution. Graham and Trotman, London. doi: https://doi.org/10.1007/978-94-009-5626-1_9

Stemmerik, L. (2008). *Influence of late Paleozoic Gondwana glaciations on the depositional evolution of the northern Pangean shelf, North Greenland, Svalbard, and the Barents Sea* (Vol. 441). Geological Society of America.

Talwani, M., Worzel, J. L., & Landisman, M. (1959). Rapid gravity computations for two-dimensional bodies with application to the Mendocino submarine fracture zone. *Journal of Geophysical Research*, *64*, 49-59. doi: https://doi.org/10.1029/JZ064i001p00049

Tauxe, L. (2010). *Essentials of paleomagnetism*. University of California Press.

Tegner, C., Storey, M., Holm, P., Thorarinsson, S., Zhao, X., Lo, C.-H., & Knudsen, M. (2011). Magmatism and Eurekan deformation in the High Arctic Large Igneous Province: 40Ar–39Ar age of Kap Washington Group volcanics, North Greenland. *Earth and Planetary Science Letters*, *303*(3), 203-214. doi: https://doi.org/https://doi.org/10.1016/j.epsl.2010.12.047

Telford, W. M., Telford, W., Geldart, L., & Sheriff, R. E. (1990). *Applied geophysics*. Cambridge University Press.

Trulsvik, M., Myklebust, R., Polteau, S., & Planke, S. (2011). Geophysical atlas of the East Greenland Basin: Integrated seismic, gravity and magnetic interpretation. *Volcanic Basin Petroleum Research AS, TGS-NOPEC Geophysical Company*.

U.S. Geological Survey. (2023). *Earthquake hazards program.* Retrieved 2023-06-05, from https://earthquake.usgs.gov/

Vozoff, K., & Jupp, D. L. B. (1975). Joint Inversion of Geophysical Data. *Geophysical Journal International*, *42*(3), 977-991. doi: https://doi.org/10.1111/j.1365-246X.1975.tb06462.x

Willmott, C. J., & Matsuura, K. (2005). Advantages of the mean absolute error (MAE) over the root mean square error (RMSE) in assessing average model performance. *Climate research*, *30*(1), 79–82. doi: https://doi.org/10.3354/cr030079

Witt-Nilsson, P., Gee, D. G., & Hellman, F. J. (1998). Tectonostratigraphy of the Caledonian Atomfjella Antiform of northern Ny Friesland, Svalbard. *Norsk Geologisk Tidsskrift*, *78*(1), 67–80.

Worsley, D. (2008). The post-Caledonian development of Svalbard and the western Barents Sea. *Polar Research*, *27*(3), 298-317. doi: https://doi.org/10.1111/j.1751-8369.2008.00085.x

Appendices

A Velocity and density relationship based on borehole data

Table A.1: Corresponding p-wave velocity and density data based on 3 boreholes (Tromsøbreen, Reindalspasset, Sarstangen)

Vel. [m/s]	Dens. [g/cm^3]	Vel. [m/s]	Dens. [g/cm^3]	Vel. [m/s]	Dens. [g/cm^3]
3000	2.47	4500	2.66	6000	2.72
3100	2.46	4600	2.64	6100	2.70
3200	2.50	4700	2.67	6200	2.75
3300	2.47	4800	2.67	6300	2.76
3400	2.53	4900	2.66	6400	2.77
3500	2.54	5000	2.66	6500	2.79
3600	2.56	5100	2.66	6600	2.78
3700	2.55	5200	2.67	6700	2.78
3800	2.58	5300	2.65	6800	2.75
3900	2.61	5400	2.67	6900	2.73
4000	2.62	5500	2.67	7000	2.76
4100	2.64	5600	2.68	7100	2.81
4200	2.65	5700	2.73	7200	2.76
4300	2.62	5800	2.71	7300	2.75
4400	2.63	5900	2.70	7400	2.79

B SvalGrav vs Olesen data: per profile

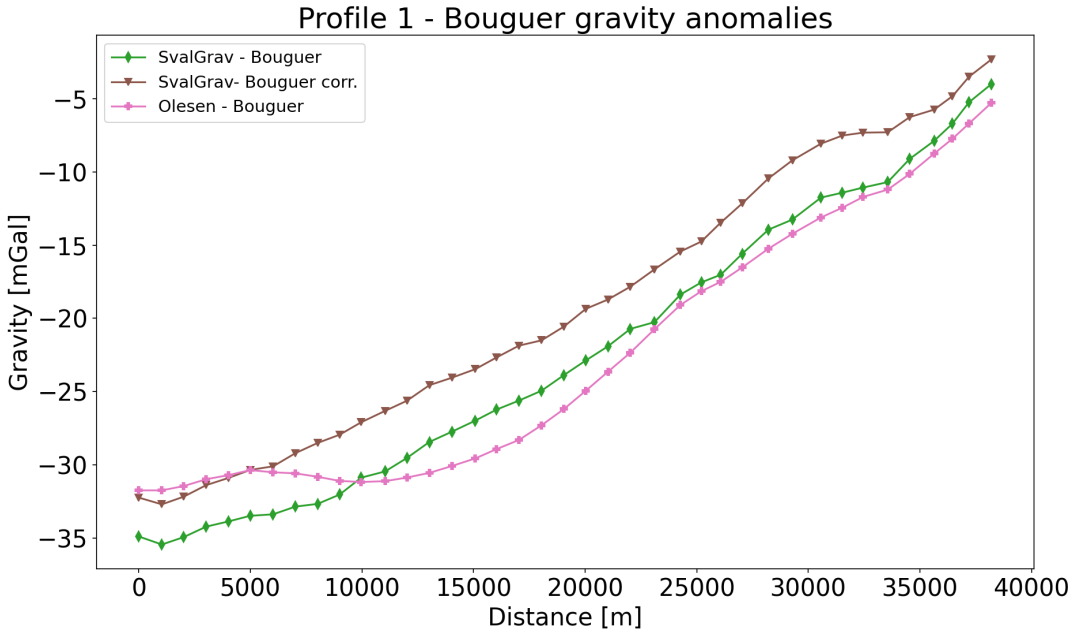

Figure B.1: Comparison of the gravity anomalies of the SvalGrav data without (Bouguer) and with (Bouguer corr.) terrain correction as well as the legacy data from Olesen et al. (2010) for Profile 1. The distance along the profile from E-W is plotted along the x-axis.

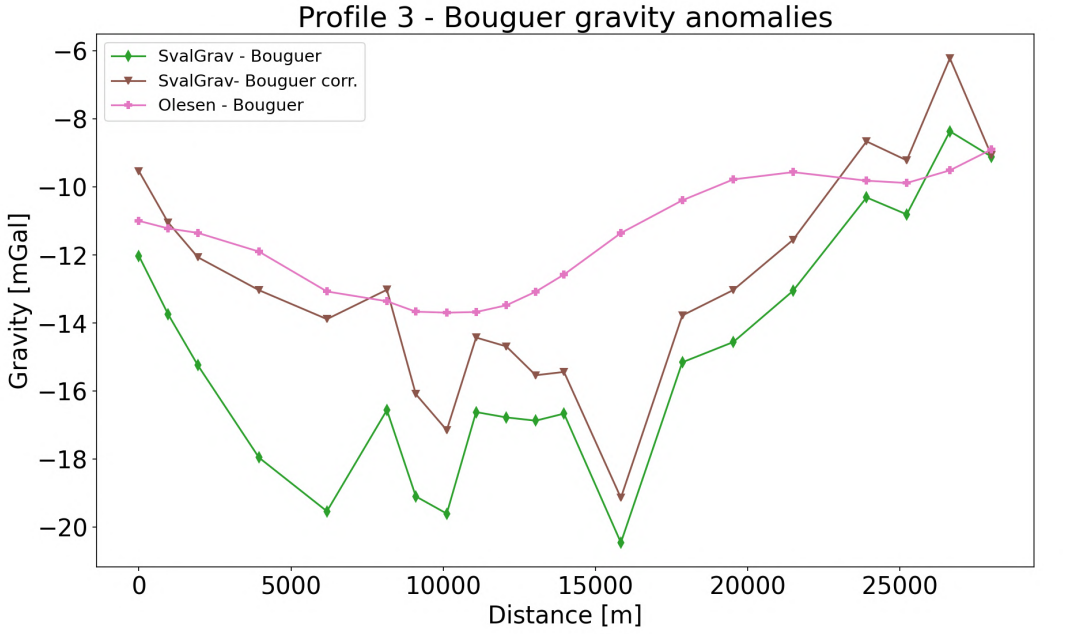

Figure B.2: Comparison of the gravity anomalies of the SvalGrav data without (Bouguer) and with (Bouguer corr.) terrain correction as well as the legacy data from Olesen et al. (2010) for Profile 3. The distance along the profile from E-W is plotted along the x-axis.

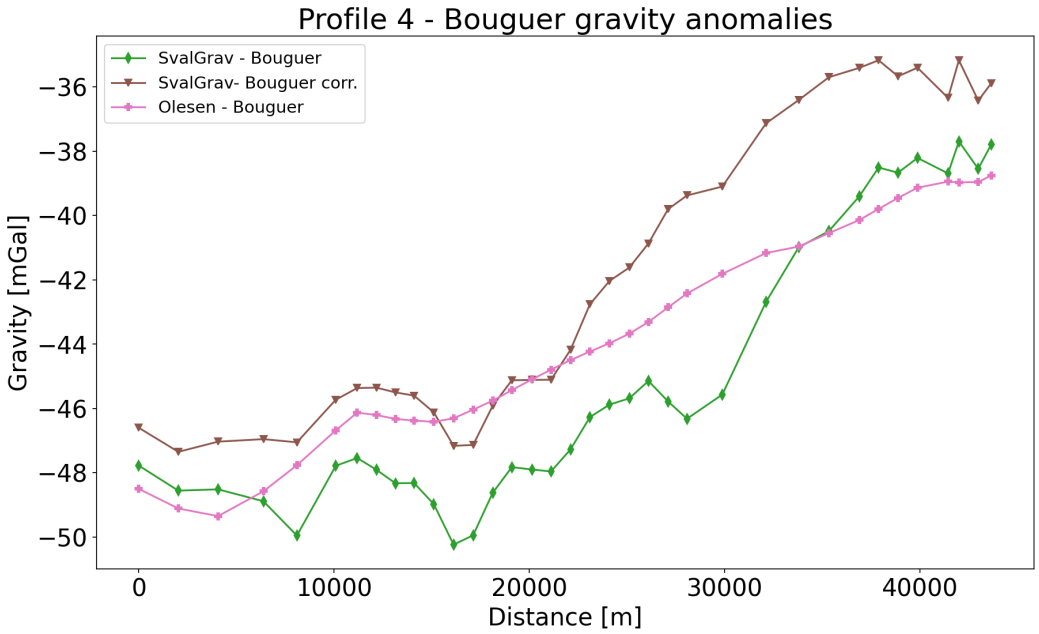

Figure B.3: Comparison of the gravity anomalies of the SvalGrav data without (Bouguer) and with (Bouguer corr.) terrain correction as well as the legacy data from Olesen et al. (2010) for Profile 4. The distance along the profile from E-W is plotted along the x-axis.

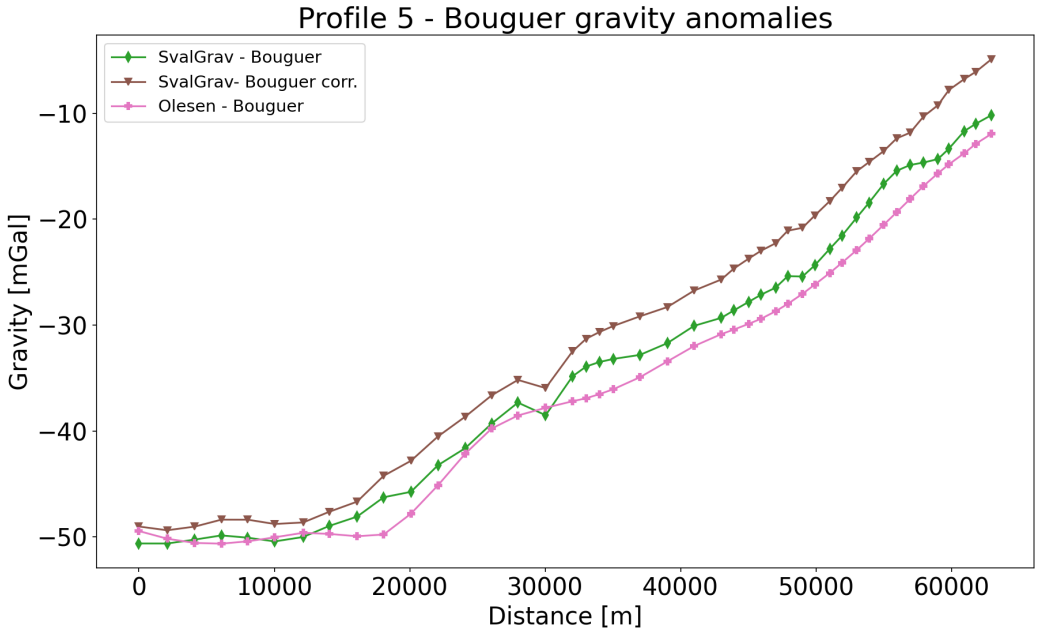

Figure B.4: Comparison of the gravity anomalies of the SvalGrav data without (Bouguer) and with (Bouguer corr.) terrain correction as well as the legacy data from Olesen et al. (2010) for Profile 5. The distance along the profile from E-W is plotted along the x-axis.

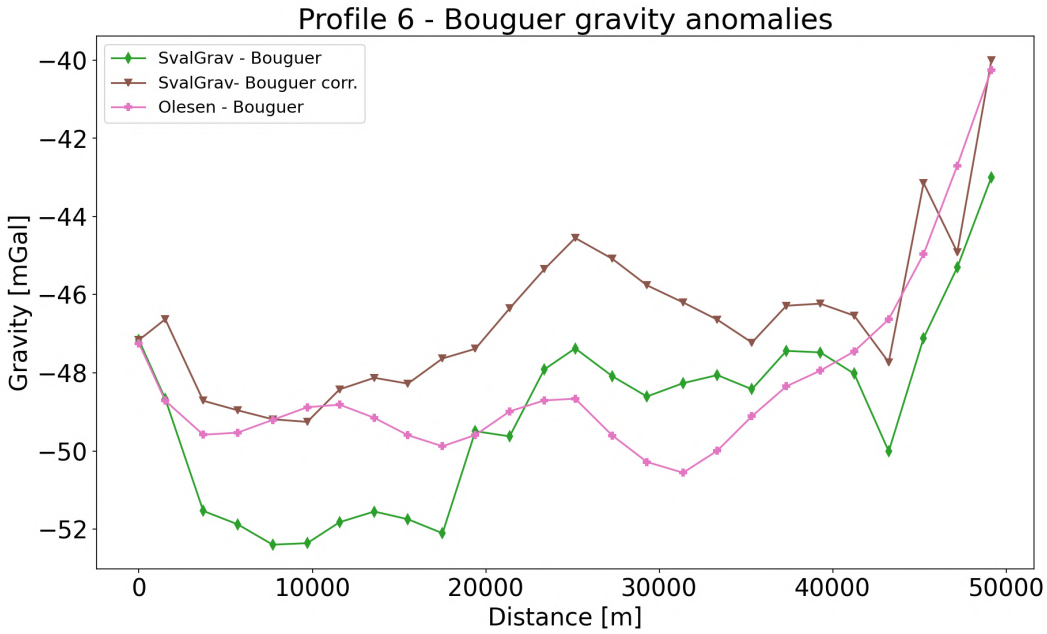

Figure B.5: Comparison of the gravity anomalies of the SvalGrav data without (Bouguer) and with (Bouguer corr.) terrain correction as well as the legacy data from Olesen et al. (2010) for Profile 6. The distance along the profile from E-W is plotted along the x-axis.

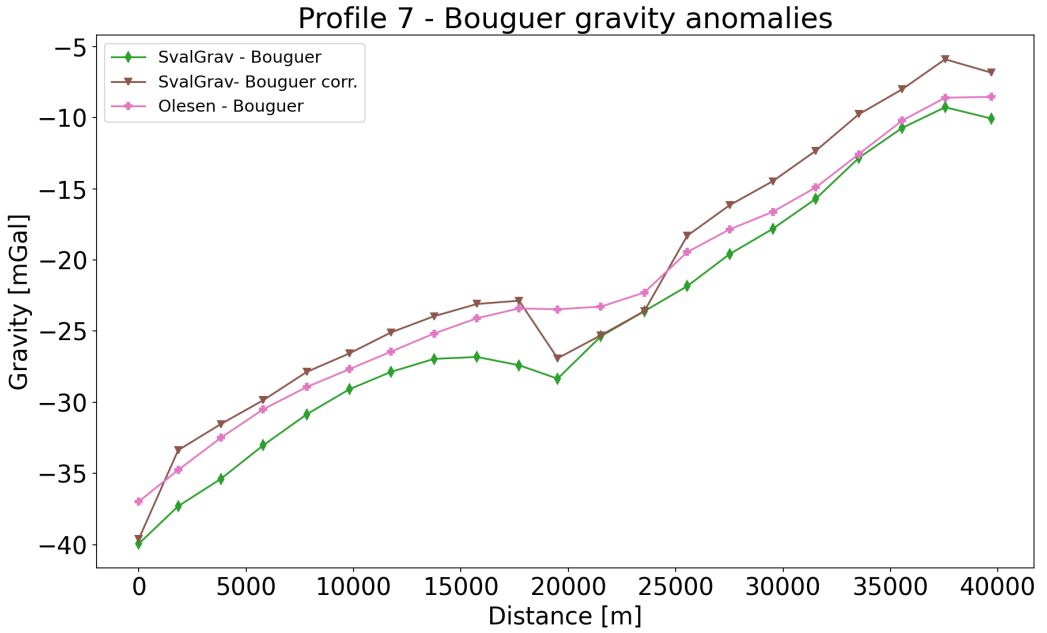

Figure B.6: Comparison of the gravity anomalies of the SvalGrav data without (Bouguer) and with (Bouguer corr.) terrain correction as well as the legacy data from Olesen et al. (2010) for Profile 7. The distance along the profile from E-W is plotted along the x-axis.

C Equal area rainbow figures

The figures in this section are identical to those in the paper but made using the traditional equal area rainbow color map.

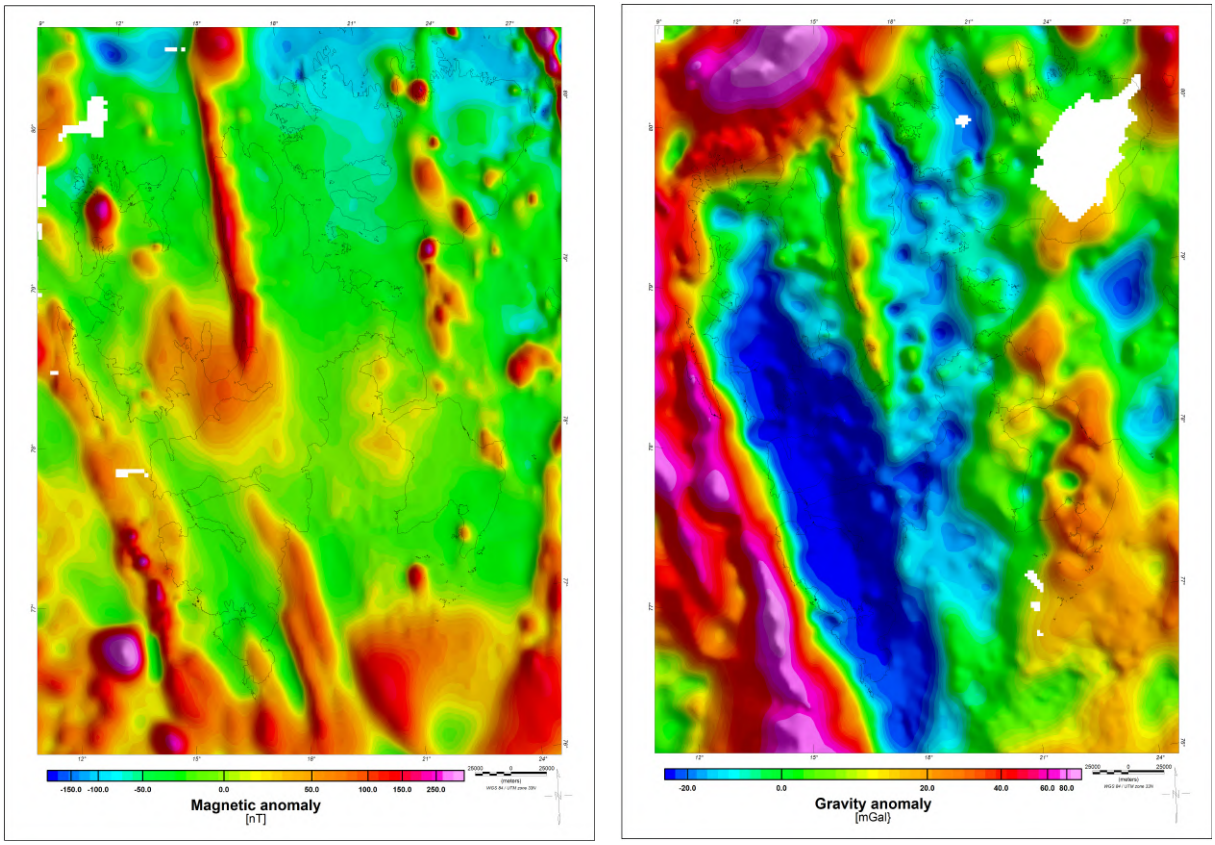

(a) Magnetic anomalies

(b) Regional map of the gravity anomalies

Figure C.1: Magnetic (a) and gravity (b) anomalies of the region plotted with the traditional equal area rainbow color map.

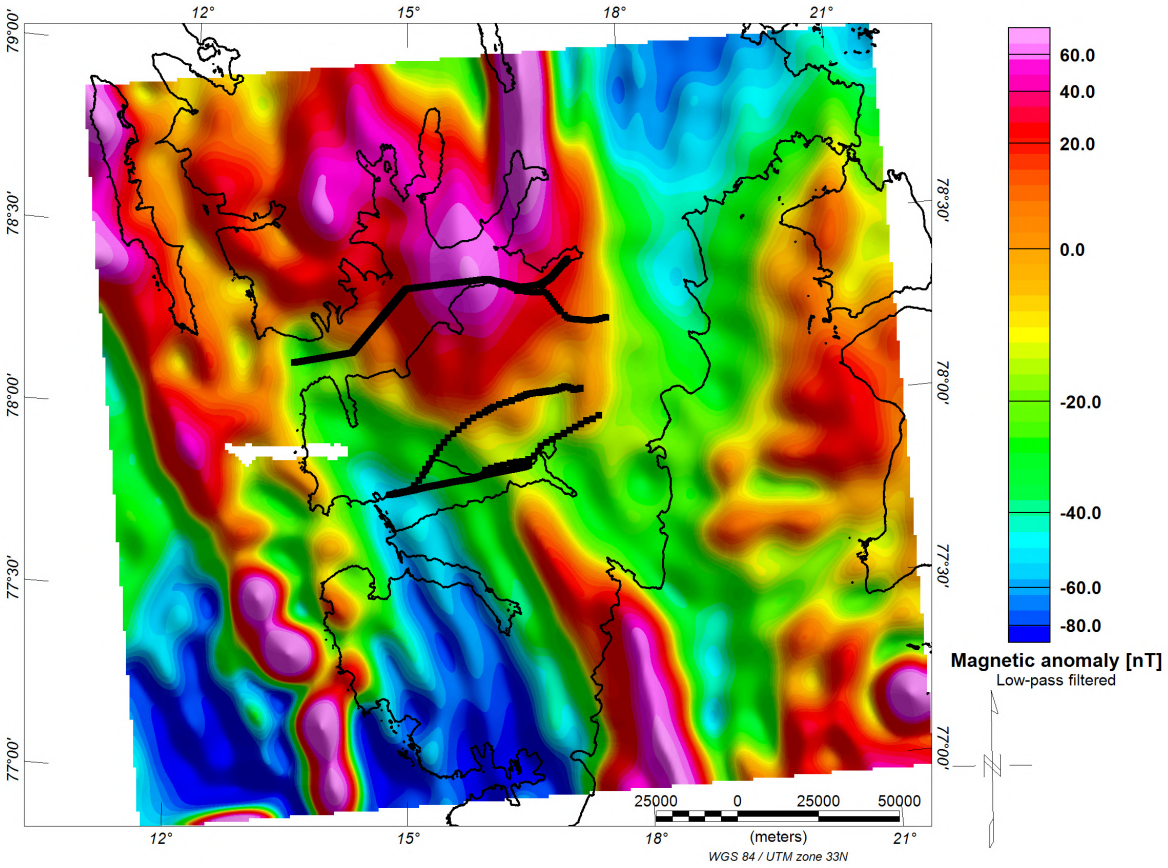

Figure C.2: The magnetic grid with a low-pass filter applied so only the long wavelength signal remains. It shows how the peak in Isfjorden extends to both Profile 2 and 5, while Profile 7 and RS are less affected.

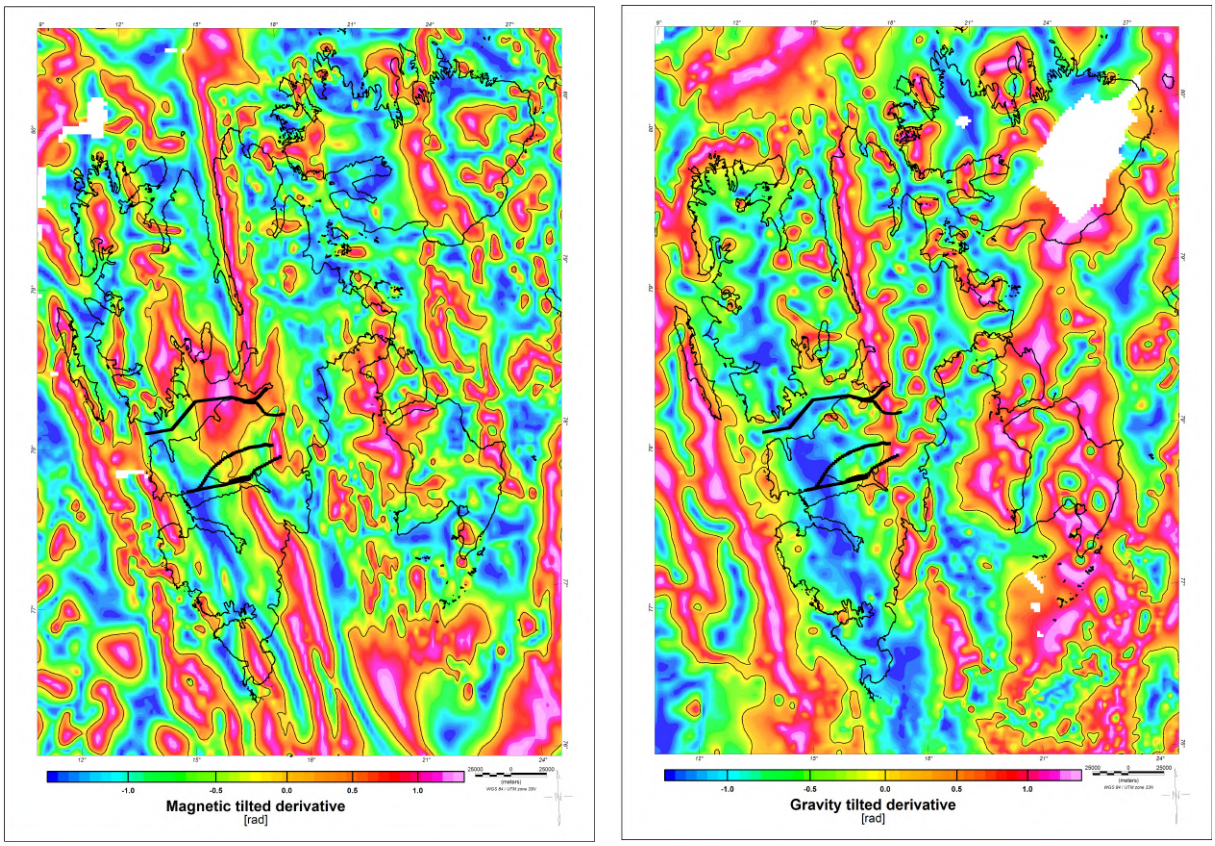

(a) Tilted derivative of the magnetic anomaly.

(b) Tilted derivative of the gravity anomaly.

Figure C.3: Tilted derivatives of the magnetic (a) and gravity (b) data plotted with the traditional equal area rainbow color map. The black line indicates the zero-contour of the tilted derivative, which is the edge of the potential source. This potential source is indicated by the area with a positive tilted derivative. The five data profiles for forward modeling are plotted with the thick black lines.

D Forward models of alternative scenarios

Profile RN

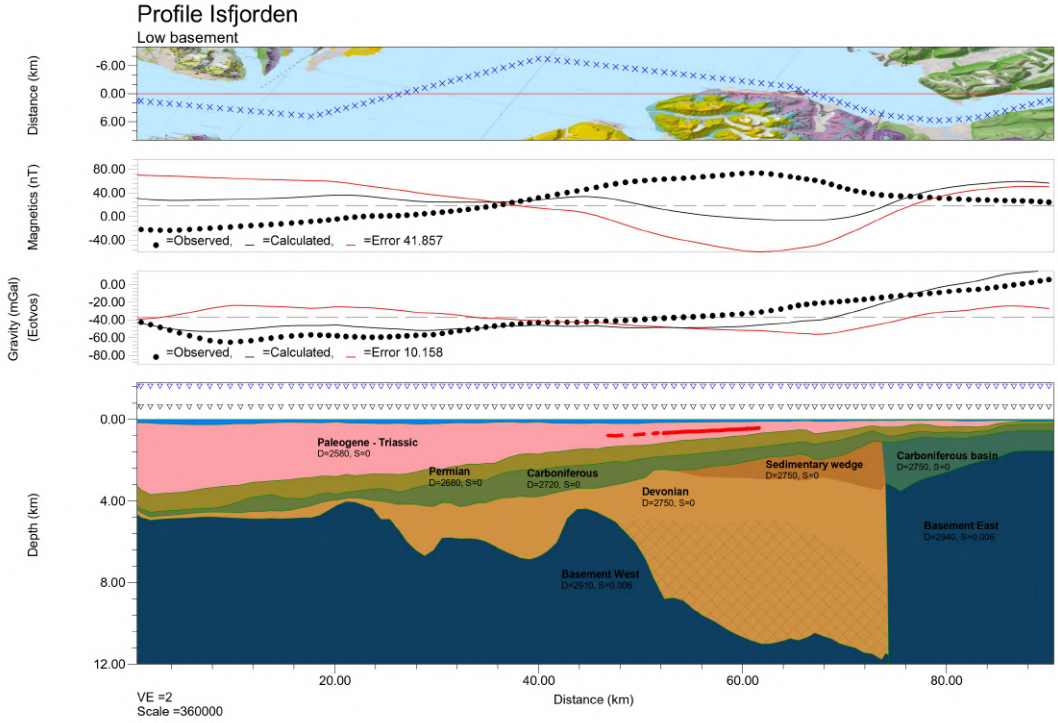

Figure D.1: Forward model of Profile RN as based on the seismic interpretation of Bælum & Braathen (2012). The model has a poor fit with both the gravity and magnetic data. The location of the data points (crosses) and the model location (red line) are plotted on the geological map. The fit between the observations and calculations of the magnetic and gravity data is shown. The forward model shows the subsurface structure, where the blue and black triangles show the elevation of the magnetic and gravity data, respectively.

Profile 2

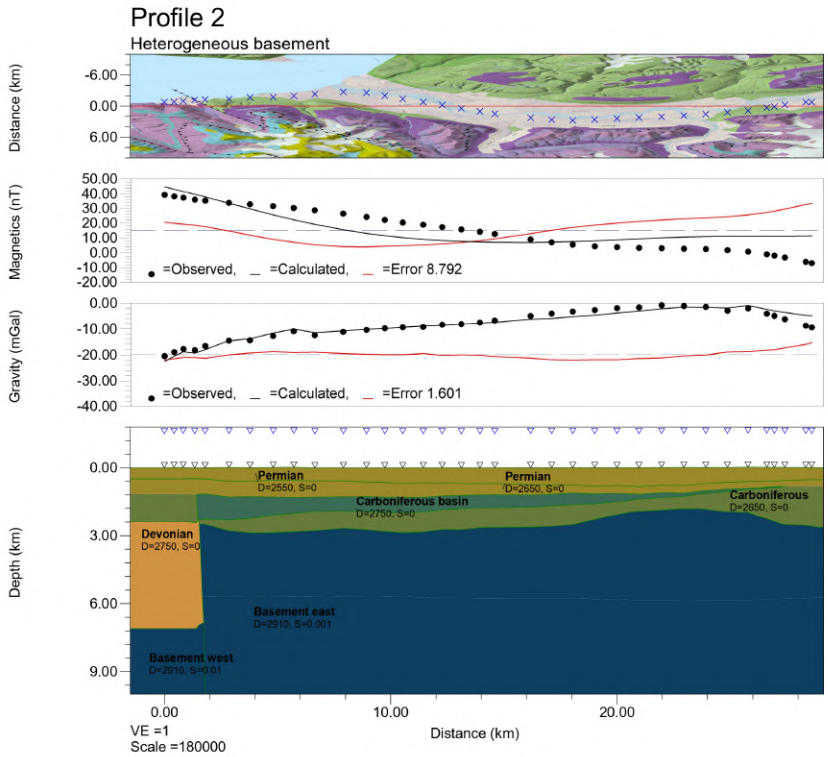

Figure D.2: Alternative forward model of Profile 2 with a heterogeneous basement with an order of magnitude difference in susceptibility of the basement. The location of the data points (crosses) and the model location (red line) are plotted on the geological map. The fit between the observations and calculations of the magnetic and gravity data is shown. The forward model shows the subsurface structure, where the blue and black triangles show the elevation of the magnetic and gravity data, respectively.

Profile 5

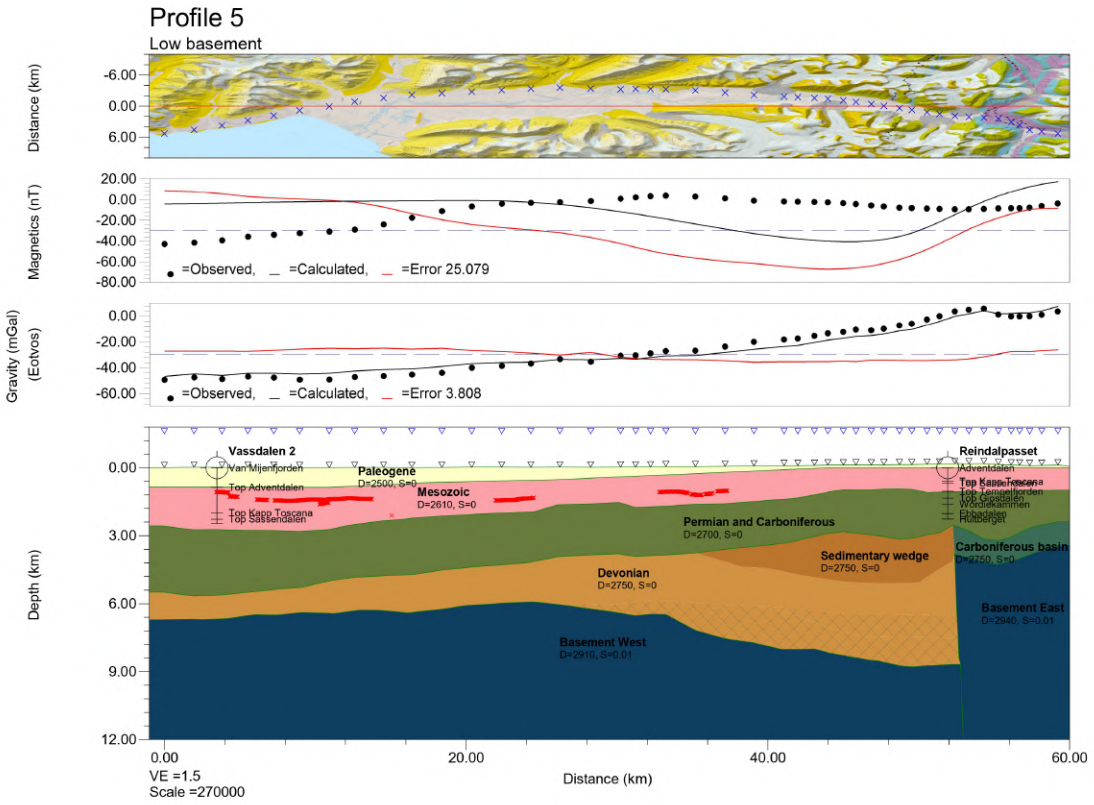

Figure D.3: Alternative forward model of Profile 5 with a low basement coinciding with previous seismic interpretations. The location of the data points (crosses) and the model location (red line) are plotted on the geological map. The fit between the observations and calculations of the magnetic and gravity data is shown. The forward model shows the subsurface structure, where the blue and black triangles show the elevation of the magnetic and gravity data, respectively.

Profile RS

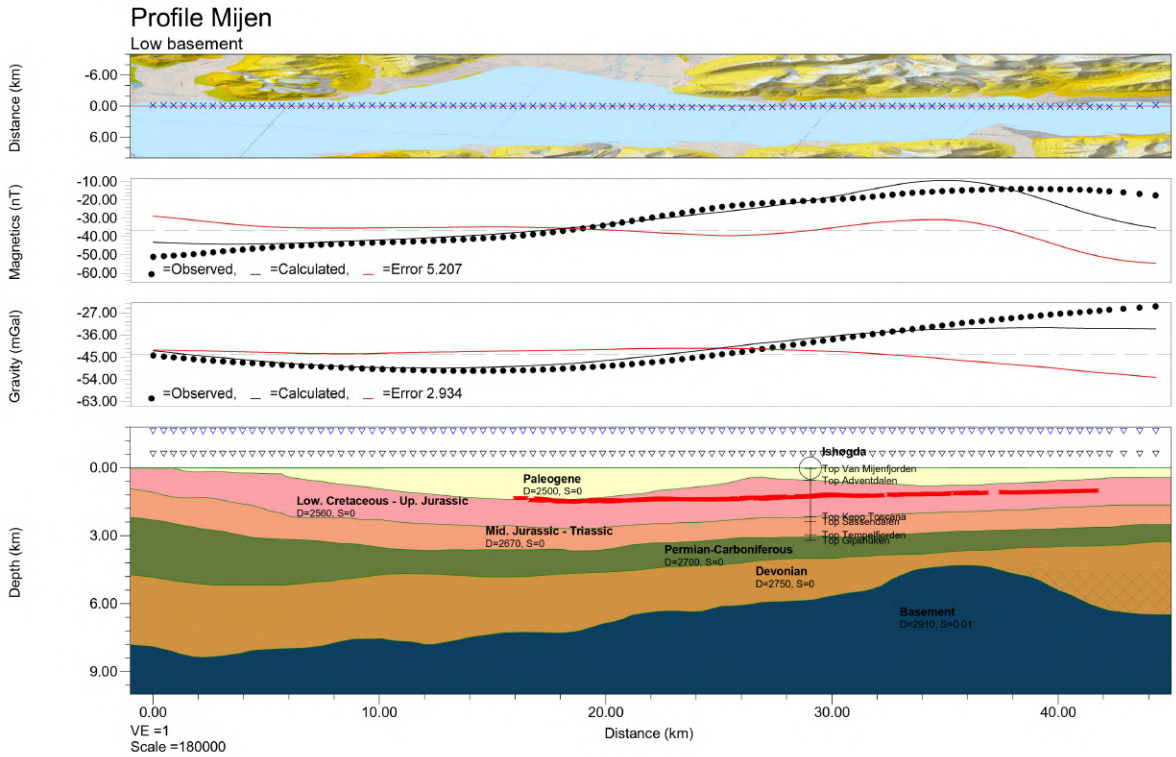

Figure D.4: Alternative forward model of Profile RS with a low basement coinciding with previous seismic interpretations. The location of the data points (crosses) and the model location (red line) are plotted on the geological map. The fit between the observations and calculations of the magnetic and gravity data is shown. The forward model shows the subsurface structure, where the blue and black triangles show the elevation of the magnetic and gravity data, respectively.

Profile 7

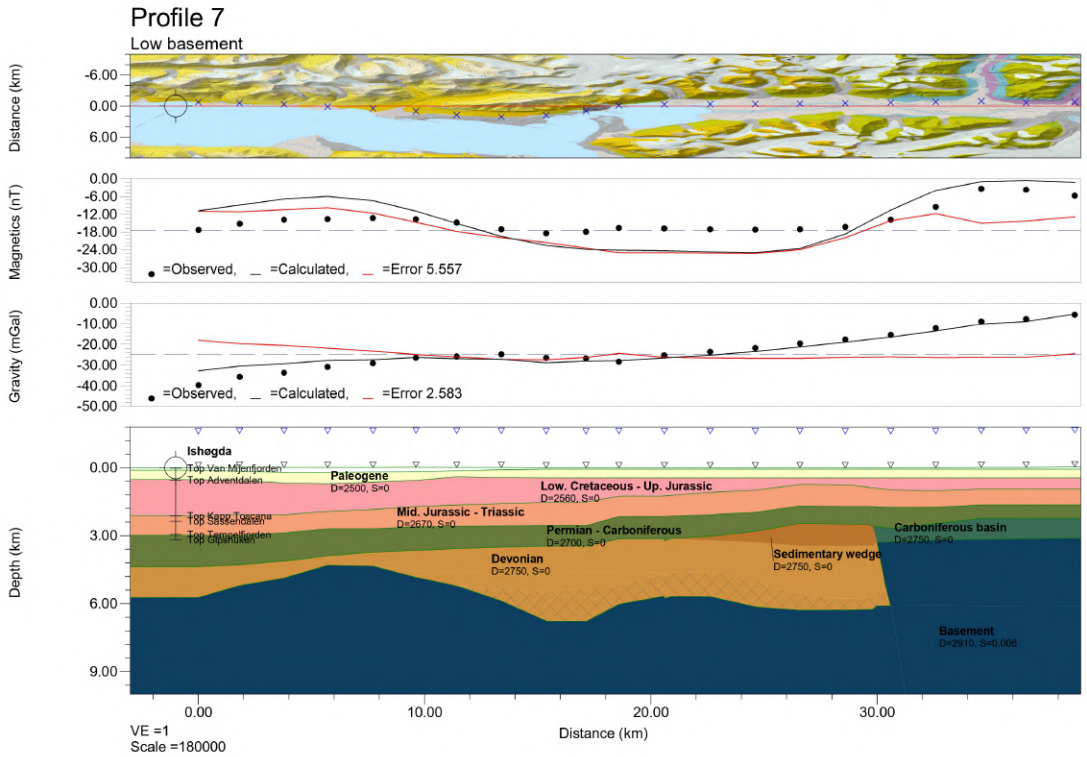

Figure D.5: Alternative forward model of Profile 7 with a low basement coinciding with previous seismic interpretations. The location of the data points (crosses) and the model location (red line) are plotted on the geological map. The fit between the observations and calculations of the magnetic and gravity data is shown. The forward model shows the subsurface structure, where the blue and black triangles show the elevation of the magnetic and gravity data, respectively.